NEWCASTLE UNIVERSITY

DOCTORAL THESIS

On the expansion of turbulent Bose-Einstein Condensates

Author:
Holly Alice Jess
MIDDLETON-SPENCER

Supervisor:
Prof. Carlo BARENGHI
Prof. Nick PARKER
Dr. Luca GALANTUCCI

*A thesis submitted in fulfillment of the requirements
for the degree of Doctor of Philosophy*

School of Mathematics, Statistics and Physics

April, 2023

ii

NEWCASTLE UNIVERSITY

Abstract

School of Mathematics, Statistics and Physics

Doctor of Philosophy

On the expansion of turbulent Bose-Einstein Condensates

by Holly Alice Jess MIDDLETON-SPENCER

Quantum Fluids provide an exquisitely tuneable playground to study numerous areas of Physics. One such area is that of turbulence. Turbulence was famously touted by Feynman as the last unsolved problem in classical physics and remains a vastly studied topic to this day. Bose-Einstein condensates - a type of quantum fluid - are dictated by quantum mechanics. This means that phase defects are quantised, allowing a simplified system to understand the nature of turbulence compared to their classical counterparts. We begin by touching upon the creation and detection of solitons within one-dimensional condensates. Here, we learn the basics of computational methods in the simulation of Bose-Einstein condensates. Using this knowledge, we then move onto more complicated three-dimensional systems, where phase defects are vortices; long strings of empty space that stretch though a condensate. We work to answer three questions in these three-dimensional systems. Firstly, we investigate how the nature of a condensate affect its time-of-flight expansion. Condensate experiments are notoriously difficult to image; experimentalists often release the condensate from its trap and take images as it rapidly expands out. These time-of-flight images are known to be affected by the phase defects within them. Here, we develop a computational technique to have a remeshing computational domain so that sizes of expanded condensates previously impossible to simulate are now reachable. We use this to study how vortices affect an expanding condensate. We then follow on by modelling the only current experimentally viable method of creating quantum turbulence in a Bose-Einstein condensate. The strong granulation and small vortex rings created give power laws not observed previously; we prove that precursory predictions of a Kolmogorov or Vinen type turbulence in these driven systems do not accurately describe our observed dynamics and further name our observed turbulence as "strong turbulence". Such a result naturally makes one question how one can experimentally create Kolmogorov or Vinen turbulence in a condensate. We thus propose a method using an imaging device which one can tune to realise a range of turbulence types. We also study how experimental results would look from such a setup before finally postulating on further work needed to understand how one can apply this method in an experiment.

Acknowledgements

It is safe to say that this PhD has coincided with the most difficult years of my life. Between the terminal diagnoses and subsequent deaths of two parents, to the global pandemic, to various health complaints, there were times where I simply felt like wanting to give up. Nevertheless, I am extremely proud of what I have achieved during this time and the work produced; physics ended up as a delightful distraction to the chaos in my life and I look forward to progressing further up the academic ladder.

First and foremost I dedicate this to my stepmother Kate Middleton, who lost her battle to cancer in March 2020 and my stepfather David Cook who lost his in December 2022. You were both in my life since I was a young child; I barely remember a life where you were not in it. Handing in this thesis is bittersweet because I know that it is the first big life achievement in which you are both not there to celebrate with me. I also dedicate this thesis to my grandmother Jess who passed of Dementia in 2020. You had a fascination of life and the universe and would have bragged endlessly about having a scientist for a granddaughter.

To my mother Fiona, who raised me single-handedly. Although we were poor when I growing up, you ensured that I never went without, was able to go to the best school around and train as a classical musician; I am only where I am today because of the sacrifices you gave. I hope you enjoying bragging that your daughter is a doctor!

I would also like to thank my partner Alastair Morgan. I simply wish to spend the rest of my life playing in orchestras and bickering with you. I am very lucky to have found someone who can tolerate my neurotic and often eccentric nature!

I would like to thank my supervisors Carlo, Nick and Luca for all the guidance throughout my studies and ensuring that my research is on a good track and that, despite the pandemic, I was able to experience all that makes academia enjoyable. Carlo's seemingly endless knowledge on every paper ever published in the area of superfluids is astounding and Luca's incredible coding abilities has ensured that I have learnt an awful lot during this PhD.

I would also like to thank Vanderlei Bagnato and the Sao Carlos Physics department for being such kind and welcoming people. My trips to Brazil will be remembered not only for the Physics, but also for the kindness you exhibited to me on my visits.

More generally, I would like to thank the (alive!) members of my family and also to Alastair's family for treating me instantly as another family member. To those friends in my department - Sam Mutter, Devika Tharakkal, Kate Brown, Thomas Flynn, "Daddy" Ash Wilkins, Stephen Mason, Sam Hawthorn-Evans, Nick Keepfer, Ryan Doran, Nicola Hewitt, James Murray,... the list goes on and I am sure I've forgotten names, however am grateful for you all and for your abilities to keep me somewhat sane.

There are also thanks to those I perform with. At times I have seriously contemplated quitting science to do music, however I do not think there are many places in the world who are looking to employ a professional viola da gamba'ist, so playing in amateur groups more than satisfies that urge. Maybe one day I will make that jump, but not today.

Contents

List of Figures

List of Tables

1 Introduction

Turbulence, characterised as the chaotic and unpredictable flow of fluids, has been a subject of fascination for scientists and engineers for centuries. There exist early mentions - mere hints - of the observation of the chaotic motion of water air in classical literature. Plutarch [1], for example, tells the story of birds falling from the sky due to the disruption of air. The first known documented attempt at the understanding of turbulence comes much later in the 16th century; Leonardo da Vinci observed and documented turbulent flow in his studies of water and air [2]. He left behind many intricate sketches of water flow, comparing the shape of water eddies to the hair of a woman. An *eddy* is a circular or swirling motion of fluid, such as air or water, that forms when fluid flows past an obstacle or when there is a disruption to the the velocity or direction of the fluid flow. Eddies can vary in size and intensity, from small vortices of the size of micrometres across to large-scale eddies that can be several kilometers in diameter.

It wasn't, however, until the 19th and 20th centuries that turbulence began to be studied systematically and scientifically. Turbulence can be seen in everyday life, from the swirling eddies in a river to the bumpy ride on an airplane during a turbulent flight; turbulence has become increasingly important for engineers seeking to design more efficient and safer aircraft, ships, and cars [3]. Today, the study of turbulence remains an active and ongoing area of research, with many unsolved mysteries yet to be answered.

Turbulence is notoriously difficult; Richard Feynman is often quoted stating that turbulence is the last unsolved problem in classical physics [4]. Aside from water and air, turbulence can be observed in a number of systems and states of matter, one of which is within a *quantum fluid*. There exist a few types of quantum fluids; such examples include Helium-3 and Helium-4 and Bose-Einstein condensates [5]. Quantum fluids are systems of particles that exhibit fluid-like behaviour at very low temperatures. At low temperatures, quantum mechanics governs the behaviour of the particles, and their wave-like nature becomes more apparent. A fascinating consequence of the dominance of quantum mechanics in this system is that vorticity and velocity fields are singular. In particular, due to quantum mechanical constraints, vorticity is confined to one dimensional objects known as quantum vortices [6].

These vortices are characterized by a quantized circulation, which means that the rotation of the fluid flowing around the vortex is always a multiple of a fundamental unit of circulation. This fundamental unit is related to the Planck constant - a foundational constant with an impactful effect on quantum mechanics, and the mass of the atom. Classical vortices can have any size, strength (circulation), shape and orientation. This is strongly dissimilar from quantum vortices whose size and strength are prescribed by quantum mechanics. The quantum nature of these vortices, of fixed width, can create vortex tangles which with interact and reconnect -

described as Vinen turbulence. A system of quantum vortices can also mimic their classical counterpart with the bundling of like-sign vortices. This mechanism creates pseudo-classical eddies which result in the appearance of classical Kolmogorov turbulence.

In this thesis, the focus of the research will be Bose Einstein Condensates. A Bose-Einstein condensate (BEC) is a unique state of matter that occurs when a collection of bosons (particles with an integer spin) are cooled to extremely low temperatures and collapse into the same quantum state. In a BEC, the bosons no longer act as individual atoms and begin to behave as a single entity, with a vast number of the particles occupying the same quantum state. This results in some remarkable properties, such as coherence and superfluidity, that are not observed in other more "ordinary" states of matter. This phenomenon was first predicted by Albert Einstein and Satyendra Nath Bose in 1920s, however it was not until 1995 that it was observed in a laboratory.

The vast majority of experimental turbulent work in quantum fluids come from Helium, where two types of vortex turbulence can be observed. Nevertheless, a small number of cold atom experiments have resulted in the reporting of visible turbulence within experiments. In these experiments, a condensate is driven at large length scales by magnetic potentials causing a turbulent cascade. The condensate is then released and the condensate imaged. Some computational modelling has been published, however a full numerical explanation to experimental results is yet to be realised. The turbulent experiments brought up questions, such as for instance the nature of the momentum distribution, the role of waves and vortices on this and the nature of the turbulence created in the turbulence experiments. Two main experimental groups have lead the development and observation of turbulence within a three-dimensional BEC;

The first experimental evidence of turbulence within a BEC was in 2009, by the group of Vanderlei Bagnato at USP, Brazil [7]. Here, a harmonically trapped cigar condensate is driven out of equilibrium by a a large, off-axis oscillatory magnetic field. In their first reported experiment, they observe randomised vortex structure, which they relate to turbulence, in their condensate. Later, they quantified the cascade of the turbulence through the 1D momentum distribution obtained experimentally [8], with comparisons to theoretical predictions on the cascade by different types of turbulence. Recently, the concept of universality in a driven system has been discussed in terms of turbulence in the USP group obtained from these same momentum distributions [9].

The group of Zoran Hadzibabic at Cambridge University, UK, developed a technique of using light sheets to create a homogeneous BEC within a box [10]. Using this, they followed the USP technique of driving the system to produce their own predictions of the type of turbulence within. They reported similar momentum distribution scaling laws, however came to different conclusions onto the nature of the turbulence they have created [11]. Whereas USP report a type of vortex turbulence, Cambridge report to have detected wave turbulence. Recently, the group has also focused on the concept of universality in various aspects of their quenched box-trapped system, with a paper specifically on the universality of an Equation of State for wave turbulence [12].

This thesis aims to answer the following:

Firstly, when an experimentalist releases a condensate from its trap, one expects

the condensate to rapidly expand out. As the condensate expands, its density falls and thus imaging becomes easier. An experimentalist passes light through the condensate. The expansion is affected by both the temperature of the system and the shape. An anisotropically shaped (such as a cigar, or a pancake) condensate will, when released, change its shape during expansion; the more strongly trapped directions will expand quicker, so that after a given time, the condensate shape will be the inverse of the originally trapped condensate. In a turbulent condensate, this does not happen; the expansion of a turbulent condensate is self-similar and thus it retains its original shape. This self-similar expansion is referred to as a signature of turbulence itself and it has been proposed analytically that the existence of vortices within a condensate inhibits the inversion of the aspect ratio of the condensate. Nevertheless, to date there have been no full study on this mechanism.

Secondly, imaging of out-of-equilibrium condensates is difficult; if a vortex is not perpendicular to the experimental imaging pane then it is almost indistinguishable to the background density. To quantify turbulence within a system, one typically measures the velocity field of the system to gain the energy spectrum, or the total length of the quantum vortices. This is obtainable experimentally in Helium systems, but not in BECs; the only true measure of turbulence in an experimental condensate has to come from the expanded density, which allows one to quantify the momentum distribution, but not, for instance, the energy spectrum or the vortex configuration. Consequently, one is not able to fully quantify the nature of turbulence in a Bose-Einstein condensate by experimental data.

On the other hand, the beauty of computational studies of turbulent Bose-Einstein condensate means that we can carefully pick, and study it in a pseudo-infinite, homogeneous system (unlike in experiments), removing any extra parameters that can add more complications to a study. One can tune the starting conditions of their study in order to pick the type of turbulence they wish to study. From there, a physicist can have access to and conduct any study she so desires; from the 3D wavefunction one is able to fully ascertain the velocity fields and vortices formed. One is also able to gain other measures such as individual energies.

1.1 Outline of Thesis

In this thesis, we aim to answer some of the questions put forward by experimentalists on the topic of quantum turbulence in a Bose-Einstein Condensate. We begin by studying a one-dimensional system and present a method of detecting solitons within a one-dimensional condensate. We also show a mathematical curiosity whereby solitons can be created in a box potential by the manipulation of said potential.

We follow on by the discussion of three-dimensional computational methods. We also discuss a way of modelling the expansion of a condensate. The ordinary method of modelling a condensate relies on using a fixed computational domain. If one wishes to model an expansion of a condensate, then one quickly realises that the grid needed is excessively, and potentially impossibly, large. As a consequence, we develop a method in which the computational domain changes as the condensate is released. As such, we are able to expand the system to the same order of size as a typical experiment. We go further and use this computational routine to

see how vortices affect the expansion of a condensate before comparing results to previously reported analytical predictions.

After ascertaining the nature of expansion, we next model the generation of turbulence within a condensate, driven through experimental means. Here, we study how the large-scale driving, used by experimental groups, drives the condensate out of equilibrium. We compare our results to experimental data kindly provided by group of Vanderlei Bagnato. What we find is not what we had originally expected; the nature of the turbulence is not one which is discussed in previous literature but a limiting case of documented Vinen turbulence coupled with large density fluctuations.

Finally, we propose a new method of generating turbulence within a condensate. We deliberately ensure the method is viable using experimentally accessible techniques. Here, it is shown that we can reproduce the strong turbulence characterised earlier, but in a cleaner manner that eases computational study. We also demonstrate that the more typical Vinen turbulence is achievable from such a driving. We end this by bringing together our driving technique and our adaptive computational grid code to begin to present the beginnings of a study on how the disorder in a condensate affects the momentum distribution obtained from the time-of-flight images.

We end this thesis on the discussion of the areas of this thesis which can be built upon at a later date. The author hopes that this thesis brings a small step toward an enhanced understanding on both quantum turbulence and turbulence as a whole.

1.2 Papers

The work presented in this thesis has resulted in published papers outlined below.

- The work regarding the detection and characterisation of solitons in 1D condensates in Chapter 4 was published in Europhysics Letters [13].

- Data from the Chapter 6 was used to create a figure referencing the differences between Kolmogorov, Vinen and strong turbulence is used in a paper accepted in AVS Quantum Science [14].

- The computational modelling of the generation of vortex turbulence in a Bose-Einstein condensate presented in Chapter 6 has been accepted by Physical Review Research [15].

Two paper drafts have been created and will be submitted to journals after the submission of this thesis. These two topics are:

- Computational verification of analytical predictions of the effect of vortices on the expansion of Bose-Einstein condensates, as shown in Chapter 5.

- A proposal for a tunable method of creating turbulence within a condensate, as outlined in Chapter 7.

Part I

Prelude:
A Study of Cold Atoms

2 A Study in the Underpinnings of Bose-Einstein Condensates

In order to understand cold atom physics, one must have a comprehensive knowledge of many areas of physics, from statistical mechanics, to quantum mechanics to fluid dynamics. In this Chapter, we introduce the reader first to the idea of Bose-Einstein statistics before deriving our chosen method of modelling of condensates - the Gross-Pitaevskii equation. We then move our focus onto turbulence where we begin by determining some results often used in the field of quantum turbulence, before then following on with a comparison between turbulence in classical and quantum fluids. Finally, we reflect on typical experimental techniques one would see in any cold atom experiment, from cooling to imaging of the atomic cloud.

2.1 Bose-Einstein statistics in an ideal Bose gas

If one has N identical particles in M available quantum states in a cubic box, then the number of different arrangements of the particles is

$$W = \frac{(N+M-1)!}{N!(M-1)!}.$$ (2.1)

The wavefunction describing a collective of atoms forming a plane-wave in the space $\mathbf{x} = (x, y, z)$ and momentum $\mathbf{k} = (k_x, k_y, k_z)$ is

$$\Psi(\mathbf{x}) = \frac{1}{V^{1/2}} \exp{(i\mathbf{k} \cdot \mathbf{x})},$$ (2.2)

where

$$\mathbf{k} = \left(\frac{2\pi n_x}{L_x}, \frac{2\pi n_y}{L_y}, \frac{2\pi n_z}{L_z} \right),$$ (2.3)

where $L_{x,y,z}$ are the lengths of the system in each direction, $n_{x,y,z}$ are integers, and V is the volume of said system ($V = L_x L_y L_z$). We can evaluate the system as a sphere with a number of thin shells with radii k_s and a thickness δk_s. A infinitesimal volume $d^3k = dk_x dk_y dk_z$ of k-space contains

$$\frac{V}{(2\pi)^3} d^3k,$$ (2.4)

states. A single shell can therefore have

$$M = 4\pi k_s^2 \delta k_s \frac{V}{(2\pi)^3},$$ (2.5)

states, the energy of which is given by

$$\epsilon_{\mathbf{k}} = \frac{\hbar^2 k^2}{2m}, \tag{2.6}$$

where $\hbar$ is the reduced Planck's constant $\hbar = h/2\pi$ and m is the particle mass. The number of states between ϵ_s and $\epsilon_s + \delta\epsilon_s$ is

$$M = \frac{V m^{3/2} \epsilon^{1/2}}{\sqrt{2}\pi^2 \hbar^3} \delta\epsilon_s. \tag{2.7}$$

In many textbooks, this is often written in the form

$$M = V g(\epsilon_s)\delta\epsilon_s, \tag{2.8}$$

where $g(\epsilon)$ is referred to as the density of states per volume,

$$g(\epsilon) = \frac{m^{3/2}}{\sqrt{2}\pi^2 \hbar^3} \epsilon^{1/2}. \tag{2.9}$$

Reminding ourselves of statistical mechanics [16], we know that the entropy of a system S is related to the total microstates, W of a given energy E via

$$S = k_B \ln W. \tag{2.10}$$

where k_B is the Boltzmann constant. The total number of microstates of the whole system can be calculated from Eq. (2.1) by

$$W = \prod_S W_S = \prod_S \frac{(N_S + M_S - 1)!}{N_S!(M_S - 1)!}. \tag{2.11}$$

Assuming N_S and $M_s \gg 1$ we can use the Stirling approximation

$$\ln(\alpha!) = \alpha \ln \alpha - \alpha + \mathcal{O}(\ln \alpha). \tag{2.12}$$

Substituting Eq. (2.12) into Eq. (2.11), the total entropy of the system is therefore

$$S = k_B \sum \left[(N_s + M_s) \ln(N_s + M_s) - N_s \ln N_s - M_s \ln M_s \right], \tag{2.13}$$

In this system, particles organise in such a way to maximise the entropy of the system. The total internal energy of the system is

$$U = \sum_s \epsilon_s N_s. \tag{2.14}$$

The total norm (number of particles) of the system is $N = \sum_s N_s$ and stays constant (as does the total energy, U). To find the maxima of Eq. (2.13), one uses the Lagrange multiplier method such that

$$\frac{\partial S}{\partial N_s} - k_B \beta \frac{\partial U}{\partial N_s} + k_B \beta \mu \frac{\partial N}{\partial N_s} = 0. \tag{2.15}$$

We can follow through by differentiating the above equation to find,

$$\ln{(N_S + M_S)} - \ln{(N_S)} - \beta\epsilon_s + \beta\mu = 0. \tag{2.16}$$

Rearranging this, one obtains

$$N_s = \frac{M_s}{\exp{[\beta(\epsilon - \mu)]} - 1}. \tag{2.17}$$

This can be redefined as the famous Bose-Einstein occupation number:

$$f_{BE} = \frac{1}{\exp{[\beta(\epsilon - \mu)]} - 1}. \tag{2.18}$$

To understand β and μ one has to recall the first law of thermodynamics

$$dS = \frac{1}{T}(dU + PdV - \mu dN), \tag{2.19}$$

where T is the temperature of the system and P is the pressure. Using Eq. (2.17), it can be shown that

$$dS = \sum_s \frac{\partial S}{\partial N_s} dN_s, \tag{2.20}$$

which goes to

$$dS = k_B\beta(dU - \mu dN). \tag{2.21}$$

One can therefore see that $\beta = 1/k_BT$. The constant μ is simply the chemical potential of the system. Using these results, we can various useful results such as the critical temperature of the gas, and the condensate ratio - the ratio of condensate to thermal atoms at a given temperature.

The total particles in a system is the summation over all wavevectors of the Bose-Einstein distribution,

$$N = \sum_{\mathbf{k}} f_{BE}(\epsilon_{\mathbf{k}}). \tag{2.22}$$

If instead of a proverbial box, we go towards an infinite case, this summation tends toward an integral

$$N = \frac{V}{(2\pi)^3} \int f_{BE}(\epsilon_{\mathbf{k}}) d^3k, \tag{2.23}$$

and the subsequent particle density, n, is N/V. Recalling the previously defined density of states, we can define the particle density as

$$n = \int \frac{g(\epsilon)}{\exp{([\epsilon - \mu] - 1)}} d\epsilon. \tag{2.24}$$

The fugacity of the system can be defined as $z = \exp{(\beta\mu)}$. Using this and $x = \beta\epsilon$, one can rewrite Eq. (2.24) as

$$n = \frac{(mk_bT)^{3/2}}{\sqrt{2}\pi^2\hbar^3} \int_0^\infty \frac{z\exp{(-x)}}{1 - z\exp{(-x)}} x^{1/2} dx. \tag{2.25}$$

One can expand this integrand to find that

$$\frac{z\exp(-x)}{1-z\exp(-x)} = \sum_{q=1}^{\infty} z^q \exp(-qx), \tag{2.26}$$

so that

$$\int_0^\infty \frac{z\exp(-x)}{1-z\exp(-x)} x^{1/2} dx = \frac{1}{q^{3/2}} \int_0^\infty y^{1/2} \exp(-y) dy. \tag{2.27}$$

This integral is in the form of a standard integral one can find in any textbook, where

$$\Gamma(t) = \int_0^\infty y^{t-1} \exp(-y) dt. \tag{2.28}$$

The term $\Gamma(t)$ is simply the gamma function which for our system will be $\Gamma(3/2) = \sqrt{\pi}/2$. We recall the fugacity earlier and now express the density of a system as a function of it, such that

$$n = \left(\frac{mk_BT}{2\pi\hbar^2}\right)^{3/2} \sum_{q=1}^{\infty} \frac{z^q}{q^{3/2}}. \tag{2.29}$$

The summation will obviously diverge for $|z| \geq 1$ but converges for $|z| < 1$. The summation above can be labelled as $g_{3/2}(z)$. We therefore assume z is only between $z \in (0,1)$. The critical temperature of a gas in a homogeneous system is therefore given by the value in which $g_{3/2}(z)$ reaches its maximum (2.612). This works out to be

$$T_c = \frac{2\pi\hbar^2}{k_Bm} \left(\frac{n}{2.612}\right)^{3/2}. \tag{2.30}$$

When the temperature of the system $T < T_C$, out of N particles, N_0 can fall down and occupy the lowest quantum state $\epsilon_\mathbf{k} = 0$. Rearranging the Bose-Einstein distribution in terms of the chemical potential μ,

$$\mu = -k_BT \ln\left(1 + \frac{1}{N_0}\right) \approx -k_BT \frac{1}{N_0}. \tag{2.31}$$

As the number of particles in the lowest mode goes to infinity, the chemical potential of the system goes to 0. The ratio of particles in the condensate mode then becomes

$$\frac{n_0}{n} = 1 - \left(\frac{T}{T_C}\right)^{3/2}. \tag{2.32}$$

Up until now, the condensate is assumed to be either in an infinite system or in a simple 3D box. In experiments, this does not happen. The critical temperature of a condensate is defined by its background density. The typical trap for an experimental condensate is that of a harmonically trapped condensate with a harmonic potential defined as

$$V(x,y,z) = \frac{1}{2}m\omega_x^2 x^2 + \frac{1}{2}m\omega_y^2 y^2 + \frac{1}{2}m\omega_z^2 z^2, \tag{2.33}$$

where ω_x, ω_y and ω_z are the individual potential oscillator frequencies in each cartesian directions. The wave function from Eq. (2.2) is now given as

$$\Psi(x,y,z) = \left(\frac{m(\omega_x\omega_y\omega_z)^{1/3}}{\pi\hbar}\right)^{3/4} \exp\left[-\frac{m}{2\hbar}(\omega_x x^2 + \omega_y y^2 + \omega_z z^2)\right]. \quad (2.34)$$

The derivation of the critical temperature can be shown by following the derivation of Bagnato et al. [17] to be

$$T_c^0 = 0.94\frac{\hbar(\omega_x\omega_y\omega_z)^{1/3}}{k_B}N^{1/3}, \quad (2.35)$$

with the condensate ratio being

$$\frac{N_0}{N} = 1 - \left(\frac{T}{T_C^0}\right)^3. \quad (2.36)$$

2.2 A weakly interacting Bose gas

Now that we understand the mathematics behind bosons and the temperature for condensation we can behind to derive a mean-field method of modelling a condensate. We now no longer assume that the bosons are ideal and that the individual atoms interact weakly. For a system of bosons with a particle number N, a linear combination of single-particle operators can be used to define so-called creation and annihilation field operators. These creation and annihilation operators at a position $\mathbf{x} = x, y, z$ at a time t are

$$\hat{\Psi}(\mathbf{x},t) = \sum \hat{a}(t)\phi(\mathbf{x},t), \quad (2.37)$$

and

$$\hat{\Psi}^\dagger(\mathbf{x},t) = \sum \hat{a}(t)\phi^\star(\mathbf{x},t), \quad (2.38)$$

respectively, where $\star$ denotes the complex conjugate. The Hamiltonian operator of a system is associated to the total energy of the system, and hence reads as follows

$$\hat{H} = \hat{P} + V_0. \quad (2.39)$$

where $\hat{P}$ and V_0 are the momentum and potentials energies of the system. Writing this in terms of field operators, this becomes

$$\hat{H} = \int \left[\frac{\hbar^2}{2m}\nabla\hat{\Psi}^\dagger(x)\nabla\hat{\Psi}(x)\right]dx$$
$$+ \frac{1}{2}\int[\hat{\Psi}^\dagger(x)\hat{\Psi}^\dagger(x')V_0(x'-x)\hat{\Psi}(x)\hat{\Psi}(x')]dx. \quad (2.40)$$

Due to our system being bosonic, these fields operators satisfy the following commutation relations:

$$[\hat{\Psi}(x), \hat{\Psi}^{\dagger}(x')] = \delta(x - x'), \tag{2.41a}$$

$$[\hat{\Psi}(x), \hat{\Psi}(x')] = 0. \tag{2.41b}$$

where $\delta(x - x')$ is defined as the Kronecker delta function. The Heisenberg picture

$$
\begin{aligned}
i\hbar\frac{\partial}{\partial t}\hat{\Psi}(\mathbf{x}, t) &= [\Psi(\hat{x}, t), \hat{H}] \\
&= \Big[-\frac{\hbar^2}{2m}\nabla^2 \\
&\quad + \int \hat{\Psi}^{\dagger}(x', t)V_0(x' - x)\hat{\Psi}(x', t)dx' \Big]\hat{\Psi}(x, t),
\end{aligned}
\tag{2.42}
$$

The integral of the effective potential $V_0(x' - x)$ integrates to $\mathcal{V} = \int V_0 dx$. From the Born approximation this can be shown to be

$$g = \frac{4\pi\hbar^2 a}{m}, \tag{2.43}$$

where a is the s-wave scattering length. With the system being a low temperature dilute Bosonic gas, we can state that the field operator $\hat{\Psi}(x)$ is made up of both the condensate and non-condensate parts (be that thermal modes or other) we can express that

$$\hat{\Psi}(x) = \psi(x) + \delta\hat{\Psi}(x). \tag{2.44}$$

There are issues in this approach, however in a large particle system (such as in the condensates we will study in this thesis) they can be neglected. Assuming that the number of the non-condensate particles can be neglected (as can be assumed in a very low temperature system), we can substitute the commutator relations (2.41) back into Eq. (2.40), to find a the quasi-classical Gross-Pitaevskii equation,

$$i\hbar\frac{\partial}{\partial t}\psi(\mathbf{x}, t) = \Big[\frac{-\hbar^2\nabla^2}{2m} + V(\mathbf{x}, t) + g|\psi(\mathbf{x}, t)|^2\Big]\psi(\mathbf{x}, t). \tag{2.45}$$

where $V(\mathbf{x}, t)$ is the external potential applied to the system.
The Gross-Pitaevskii equation has a conserved norm (number of particles),

$$N = \int |\Psi(\mathbf{x}, t)|^2 d\mathbf{x}, \tag{2.46}$$

and linear momentum

$$p = \frac{i\hbar}{2}\int [\psi^{\star}(\mathbf{x}, t)\nabla\psi(\mathbf{x}, t) - \psi(\mathbf{x}, t)\nabla\psi^{\star}(\mathbf{x}, t)]d\mathbf{x}. \tag{2.47}$$

Equation (2.45) was derived separately by Gross [18] and Pitaevskii [19]. Further modifications can be made in order to model finite temperature effects, but these are beyond the scope of this thesis. The interaction parameter g given in Eq. (2.45) is a function of the scattering length. This scattering length can be of any value and the sign of which dictates the type of condensate formed. In this thesis, we focus

on repulsive condensates, i.e., when $g > 0$.

We can obtain the energy functional of the system in order to see the separate energies of the system,

$$\mathcal{E} = \frac{\hbar^2}{2m}|\nabla \psi(\mathbf{x}, t)|^2 + V|\psi(\mathbf{x}, t)|^2 + \frac{g}{2}|\psi(\mathbf{x}, t)|^4. \tag{2.48}$$

These different energies will be used throughout the thesis and will thus be identified here. Assuming the trapping potential, V is time-independant, the total energy of the system is conserved in time,

$$E_{tot} = \int \left[\frac{\hbar^2}{2m}|\nabla \psi(\mathbf{x}, t)|^2 + V|\psi(\mathbf{x}, t)|^2 + \frac{g}{2}|\psi(\mathbf{x}, t)|^4 \right] d\mathbf{x}. \tag{2.49}$$

The first term of Eq. (2.48) when integrated is the kinetic energy of the condensate,

$$E_{kin} = \int \frac{\hbar^2}{2m}|\nabla \psi(\mathbf{x}, t)|^2 d\mathbf{x}, \tag{2.50}$$

the second being the potential energy of the condensate,

$$E_{pot} = \int V|\psi(\mathbf{x}, t)|^2 d\mathbf{x}, \tag{2.51}$$

and the third being the interaction energy,

$$E_{int} = \int \frac{g}{2}|\psi(\mathbf{x}, t)|^4 d\mathbf{x}. \tag{2.52}$$

From the energy integrand, Eq. (2.48), One useful measure from fluid dynamics is the velocity field, which is related to the phase of the wavefunction by

$$\mathbf{v}(\mathbf{x}, t) = \frac{\hbar}{m}\nabla S(\mathbf{x}, t) d\mathbf{x}. \tag{2.53}$$

The wavefunction of the condensate, $\psi(\mathbf{x}, t)$ can be separated into real and imaginary parts by the Madelung transformation,

$$\psi(\mathbf{x}, t) = \sqrt{n(\mathbf{x}, t)} \exp\left[iS(\mathbf{x}, t)\right], \tag{2.54}$$

where $n(\mathbf{x}, t)$ is the density of the condensate, $n(\mathbf{x}, t) = |\psi(\mathbf{x}, t)|^2$. One can use the Madelung transform and substitute it back into the GPE, Eq. (2.45). If one then separates the real and imaginary parts of this, one obtains the Euler equation

$$m\frac{\partial \mathbf{v}}{\partial t} = -\nabla\left(\frac{1}{2}mv^2 + V + gn - \frac{\hbar^2}{2m}\frac{\nabla^2\sqrt{n}}{\sqrt{n}} \right), \tag{2.55}$$

and the continuity equation

$$\frac{\partial \mathbf{v}}{\partial t} + \nabla \cdot (n\mathbf{v}) = 0. \tag{2.56}$$

The last term in Eq. (2.55) is referred to as the quantum pressure of the system, and is related to the zero-point quantum mechanical motion of the condensate. Substituting Eq. (2.54) into the energy integrand Eq. (2.48) reveals two terms, the quantum kinetic energy,

$$E_q = \int \frac{\hbar^2}{2m} |\nabla \sqrt{n(\mathbf{x}, t)}|^2 d\mathbf{x}, \tag{2.57}$$

and the fluidic kinetic energy

$$E_K = \int \frac{1}{2} mn |\mathbf{v}(\mathbf{x}, t)|^2 d\mathbf{x}. \tag{2.58}$$

The fluidic kinetic energy of the condensate can be split into two parts; the compressible (associated with density fluctuations) and the incompressible energies (associated with the quantum vortices),

$$E_K = E_i + E_c. \tag{2.59}$$

Defining a density averaged velocity field [20],

$$\mathbf{w}(\mathbf{x}, t) = \sqrt{n(\mathbf{x}, t)} \mathbf{v}(\mathbf{x}, t), \tag{2.60}$$

and separating with the Helmholtz theorem with $\nabla \cdot \mathbf{w}_i(\mathbf{x}, t) = 0$ and $\nabla \times \mathbf{w}_c(\mathbf{x}, t) = 0$, the incompressible and compressible energies are defined as

$$E_i = \int \frac{m}{2} |\mathbf{w}_i(\mathbf{x}, t)|^2 d\mathbf{x}, \tag{2.61}$$

and

$$E_c = \int \frac{m}{2} |\mathbf{w}_c(\mathbf{x}, t)|^2 d\mathbf{x}, \tag{2.62}$$

respectively. The incompressible energy of a turbulent system is often given in Fourier space as a one-dimensional spectra, referred to as the incompressible energy spectrum. Defining the incompressible energy in Fourier space,

$$E_i(\mathbf{k}, t) = \int \frac{m}{2} |\tilde{\mathbf{w}}_i(\mathbf{k}, t)|^2 d\mathbf{k}, \tag{2.63}$$

where k denotes the Fourier spacial domain, and $\tilde{w}$ is the Fourier transform of the density averaged velocity field. The one dimensional incompressible energy spectra is thus the angle-averaged incompressible energy,

$$E_i^{(1D)}(k) = 4\pi k^2 E_i(\mathbf{k}). \tag{2.64}$$

The wavefunction of the condensate is both dependant on both space and time. We can instead find a time-independant solution by

$$\psi(\mathbf{x}, t) \to \psi(\mathbf{x}) \exp\left(-\frac{i\mu t}{\hbar}\right). \tag{2.65}$$

Substituting Eq. (2.65) back into the GPE, one finds the *time independant* GPE to be

$$\left(-\frac{\hbar^2}{2m}\nabla^2 + V(\mathbf{x}) + g|\psi(\mathbf{x})|^2 - \mu\right)\psi(\mathbf{x}) = 0. \tag{2.66}$$

Equation (2.66) is surprisingly useful and has a few applications. The first of these will be discussed later, where it is employed computationally to find the ground state of any repulsive system for a given norm N. Secondly, it provides a good approximation for the shape of a condensate given its potential. Assuming a large collective of atoms, we can assume that the ∇^2 term in Eq. (2.66) is negligible such that we can arrange to

$$\mu\psi - V(\mathbf{x})\psi(\mathbf{x}) + g|\psi(\mathbf{x})|^2\psi. \tag{2.67}$$

For a box trap where the potential is

$$V(\mathbf{x}) = \begin{cases} 0, & \text{where } \mathbf{x} < L, \\ A, & \text{otherwise,} \end{cases} \tag{2.68}$$

where $A \gg \mu$. This gives a Thomas-Fermi profile as a top-hat function where $|\psi|^2 = \mu/g$ where $V = 0$ and 0 otherwise. For a harmonic condensate, the potential is defined as

$$V(\mathbf{x}) = \frac{1}{2}m\omega_{\mathbf{x}}^2\mathbf{x}^2, \tag{2.69}$$

the corresponding Thomas-Fermi profile is given as

$$n(\mathbf{x}) = \begin{cases} \frac{\mu}{g}\left(1 - \frac{\mathbf{x}^2}{R_{\mathbf{x}}^2}\right), & \text{where } \mathbf{x} < R_{\mathbf{x}}, \\ 0, & \text{otherwise.} \end{cases} \tag{2.70}$$

The term $R_{\mathbf{x}}$ is defined as the "Thomas-Fermi" radius of the condensate and provides a useful measure for the width of the condensate. Akin to the time-independent GPE, these density functions offer a suitable first guess to find the ground state of a system. Although the Thomas-Fermi profile and radii were derived here using the TIGPE (time-independent Gross-Pitaevskii Equation), they can be used to find approximations for the collective modes and expansion of a given harmonic condensate. As well as the oft-used estimation of the shape of a condensate, one can also categorise the smallest scale-length of the system. Looking at the Thomas-Fermi shape of a condensate in a box [Eq. (2.68)], the density of the condensate is uniform at all locations that the potential is $V = 0$. In reality this is not the case; towards the edges of the box, the condensate has to fall to zero, with the width of this change being able to be defined (see Fig. 2.2). If we assume for now that we have a one-dimensional GPE with a hard-wall potential $V(x \leq 0) = A$ and $V(x > 0) = 0$. If $A = \infty$, the boundary conditions of the wavefunction must state that $\Psi(x = 0) = 0$ and $\Psi(x \to \infty) = \sqrt{\mu/g}$. A solution that satisfies this is

$$\Psi(x) = \sqrt{\frac{\mu}{g}}\tanh\left(\frac{x}{\xi}\right). \tag{2.71}$$
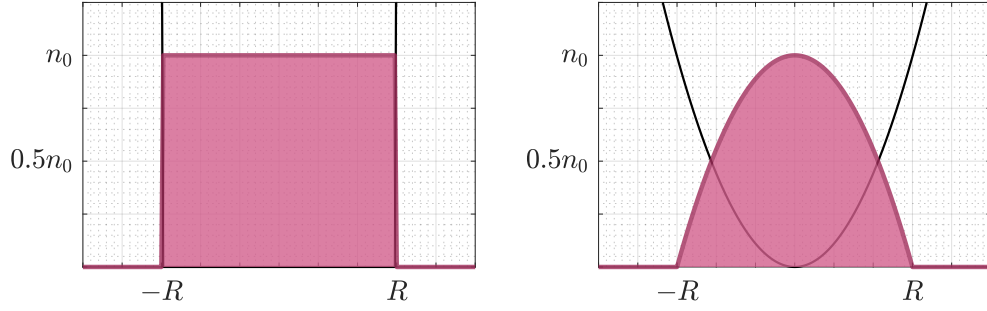
FIGURE 2.1: The Thomas-Fermi density profiles of a condensate in
a 1D box potential (left) and a harmonic potential (right) with back-
ground potentials marked in black.

The parameter ξ denotes the minimum scale length in which Ψ can spatially alter
and is referred to as the "healing length" of the system; the healing length of a
condensate is given as

$$\xi = \frac{\hbar}{\sqrt{m\mu}}. \tag{2.72}$$
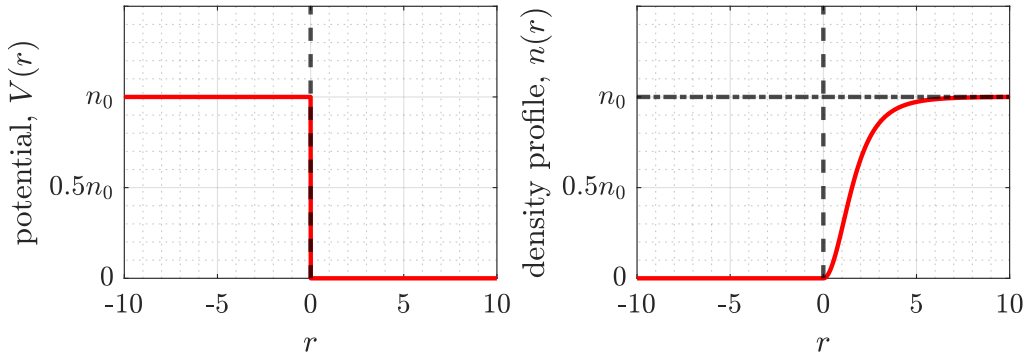
FIGURE 2.2: The potential (left) of a hard-wall and (right) the cor-
responding density profile at this edge. Marked is the boundary of
the wall (dashed) and the peak density $n_0 = \mu/g$.

2.3 Non-dimensionalising the Gross-Pitaevskii Equation

In this thesis, we use two different kinds of nondimensionalizing for the Gross-
Pitaevskii equation. For the majority of this work we use *natural* units, where the
length and time is dictated by the healing length $\xi = \hbar/\sqrt{m\mu}$ such that $\mathbf{x}' = \mathbf{x}/\xi$,
$t' = t/\tau$, where $\tau = \hbar/\mu$, the energy being rescales by μ and $V' = V/\mu$ so that

$$i\frac{\partial \psi'}{\partial t'} = -\frac{1}{2}\nabla^2 \psi' + |\psi'|^2 \psi' + V'\psi'. \tag{2.73}$$

The system is normalised such that the peak density $n_0 = 1$.

In Chapter 6, to match the given experimental parameters we use the *harmonic oscillator* units. The units of time and length are now a function of the harmonic oscillator length $\ell = \sqrt{\hbar/m\omega_r}$, where the trapping frequency in the r direction, ω_r. The lengths are therefore $\mathbf{x}' = \mathbf{x}/\ell$ and $t' = t\omega_r$ so that

$$i\frac{\partial \psi'}{\partial t'} = -\frac{1}{2}\nabla'^2\psi^2 + \mathcal{C}|\psi'|^2\psi' + V'\psi', \tag{2.74}$$

and the interaction energy is given as $\mathcal{C} = 4\pi a_s N/\ell$, where N is the number of atoms in the condensate. The condensate is normalised so that $\int |\psi'|^2 d^3\mathbf{x}' = 1$. The trapping frequencies, ω_r' and ω_z' are a ratio of ω_r such that $\omega_r' = 1$ (and is therefore left out). The interaction strength $\mathcal{C}$ is chosen by assuming a Thomas-Fermi profile in the harmonic trap where the potential is $V(x,y,z) = \frac{1}{2}(x^2 + y^2 + \omega_z'^2 z^2)$, such that

$$\mathcal{C} = \mu'^{5/2}\frac{16\sqrt{2}\omega_r}{15\omega_z}, \tag{2.75}$$

where μ' is the rescaled chemical potential, $\mu' = \mu/\hbar\omega_r$. From now on, primes are ignored.

2.4 Toplogical Defects in Bose-Einstein Condensates

2.4.1 Solitons

A soliton is a non-dispersive, localised wave which travels at a constant velocity; whereas a normal wave will break down in time, the balance of the dispersive nature of the system and the nonlinearity means that it is able to preserve its shape. There are different types of solitons. In a repulsive condensate (the focus of this thesis), dark solitons are a solution to the reduced dimensionality Gross Pitaevskii equation. The Gross-Pitaevskii equation given in three-dimensions in Eq. (2.45) in a harmonic potential can be reduced down to be applicable to one-dimensional systems. One can make the ansatz that the wavefunction,

$$\psi(x,y,z,t) = \psi_x(x,t)G_y(y)G_z(z), \tag{2.76}$$

where $G_{y,z}$ are Gaussian functions. In this limiting case of $\hbar(\omega_x\omega_y) \gg \mu$ and $\omega_{x,y} \ll \omega_z$, one can derive the Gross-Pitaevskii equation in the one dimensional limit,

$$\frac{\partial \psi}{\partial t} = -\frac{\hbar^2}{2m}\frac{\partial^2 \psi}{\partial z^2} + g_{1D}|\psi|^2\psi + \frac{1}{2}m\omega_z^2 z^2 - \mu_{1D}\psi, \tag{2.77}$$

where

$$g_{1D} = \frac{g}{2\pi\ell_x\ell_y}, \tag{2.78}$$

and

$$\mu_{1D} = \mu - \frac{\hbar\omega_x}{2} - \frac{\hbar\omega_y}{2}. \tag{2.79}$$

A black soliton is a stationary state in the 1DGPE equations. As well as this stationary state, the GPE allows semi-stationary states known as *dark* solitons (technically,

these are not solitons, however are considered as such in both optical and atomic physics [21]). The 1DGPE in Eq. (2.77) has a non-trivial solution [22], defined as

$$\psi(z,t) = \sqrt{n_0} \left(B \tanh \left[\frac{B(x - vt)}{\xi} \right] + i\frac{v}{c} \right), \quad (2.80)$$

where $\mathcal{B} = \sqrt{1 - v^2/c^2}$, u is the speed of the soliton and c is the speed of sound at x. The density dip and width of a soliton is directly related to the speed of the soliton, $\Delta n = n_0(1 - v^2/c^2)$; the faster the soliton, the shallower the shape, and example of a dark soliton with speed $v = 0.5c$ is shown in Fig. 2.3. The
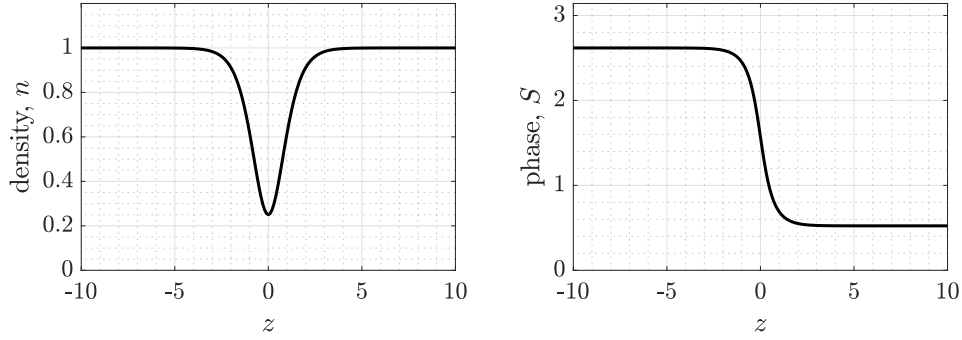
FIGURE 2.3: The density (left) and phase (right) of a dark soliton in a homogeneous 1D background, with a speed of $v = 0.5c$.

black soliton ($v = 0$) is a special case of a dark soliton and is stationary. A dark soliton in a homogeneous system will travel to infinity. In practice, however, an infinitely large homogeneous condensate is not possible and so of use is the study of a vortex in a harmonically trapped condensate or a soliton in a hard-wall box. The background condensate in a harmonically trapped condensate is varying, and as such a vortex moving in one direction will change speed corresponding to the change in the background density. At the point in which $n(z) = \Delta n$, the soliton will change direction. This movement corresponds to an oscillatory motion through the condensate with the frequency $\omega = \omega_z/\sqrt{2}$ [23]. A dark soliton colliding with a hard wall will also rebound and change direction [24]. As solitons traverse a trapped condensate, they will also emit sound [25]; the soliton-sound interaction is as well studied. Various other decay mechanisms for dark solitons in condensates have been reported, such as due to the trap shape [26] and the temperature of the system [27]. Originally postulated by Carr *et al* in 2001 [28], the combination of phase-imprinting and density-engineering was shown by Fristch *et al* [29] in 2020 to give a dark soliton of any arbitrary speed. Early techniques [30, 31], were also able to create solitons of the experimentalist's choice, albeit only ones with a large speed (and hence shallow shape).

2.5   Vortices in condensates

Dark solitons are inherently unstable in 3D systems and break down into density waves and ring vortices [32]. There is, however, another phase defect in condensates - vortices. Vortices are ubiquitous in nature; whether they are a few millimetres, metres or thousands of kilometres wide, vortices are a natural occurrence that appear in every aspect of our universe. A quantum fluid is no exception with vortices being observed in both liquid helium and condensates, although their nature is significantly different as result of quantum mechanical constraints.
As $\mathbf{v} = (\hbar/m)\nabla\phi$, the velocity field is irrotational,

$$\nabla \times \mathbf{v} = 0. \tag{2.81}$$

However, BECs may sustain topological defects, where the phase has a singularity and the amplitude of $\psi \to 0$. These topological defects are effectively one-dimensional and the quantum fluids is expelled from their core. Furthermore, the whole vorticity of fluid is confined on these 1D objects: quantised vortices. The term "quantised" is related to a peculiar characteristic regarding the circulation of the velocity field. The wavefunction of the condensate is single valued, and ergo it must be that the change of phase $\Delta\phi$ around the closed contour around the vortex's axis much be a multiple of 2π

$$\Delta\phi = \oint \nabla\phi \cdot d\mathbf{l} = 2\pi q, \tag{2.82}$$

where q is any integer. The circulation around this is therefore,

$$\Gamma = \oint \mathbf{v} \cdot d\mathbf{l} = \frac{h}{m}q. \tag{2.83}$$

Any circulation of a quantised vortex is therefore quantised by units of h/m. If $q \neq 0$, the closed contour contains a vortex. Although allowed mathematically, due to the scaling of energy associated with the circulation of the condensate scaling with q^2, any "multiply-charged" vortex (that is, a vortex with $|q| > 1$) is inherently unstable and will break up into q vortices each with unitary circulation [33].
Vortices are valid solutions in both two-dimensional and three-dimensional systems. The dynamics of vortices is heavily dependant on the dimensionality of the system. When two 2D vortices meet the do not reconnect (as 3D vortices do), but form either a vortex-anti vortex pair, rotate around each other or annihilate. This thesis concerns only 3D vortices and therefore will be the focus here, but interesting 2D vortex dynamics can be reviewed in Ref. [34] and references therein. In 3D systems, vortices can either be lines (where the ends terminate at the condensate's boundaries) or rings (where the vortex is in a closed loop). Almost immediately after the first experimental creation of condensates, methods of creating vortices in condensates were proposed and used to observe the first vortex structures in condensates [35–38]. For example, from a method proposed by Williams and Holland in 1999 [38], Matthews *et al* [39] were able to observe vortices in a two component system. Any attempt at a complete inventory of the early techniques of vortex creation and studies would be non-exhaustive, however a detailed historiography of

early vortex experiments in BECs can be found in [34]. Examples regarding the creation of vortices include Leanhardt et al's imprinted vortices by imprinting phases [40], Henn et al.'s creation of vortices via the superposition of oscillating [41] and the merging of condensates to create vortices [42]. As well as in simple bosonic systems, vortices have also been created in strongly interacting Fermi systems [43]

When two 3D vortices approach each other, they combine and then split apart, referred to as a *reconnection* and shown in Fig. 2.4. Here, they get close enough that
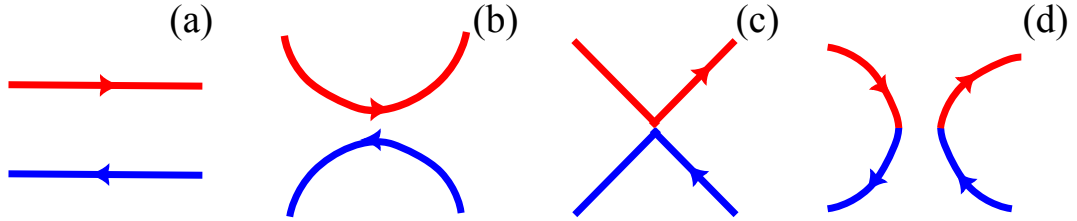
FIGURE 2.4: Two oppositely charged vortices reconnecting; (a) two vortices of opposite sign (denoted by the arrows) are near each other, (b) they begin to interact and thus approach, (c) they combine and then (d) travel apart, having exchanged tails.

they exchange tails and the topological nature of the system changes. Multiple possibilities have been postulated on reconnection characteristics. One such is how the minimum distance between two vortices $\delta(t)$ scales with time before and after the reconnection [44–51]. Many of these authors have postulated and computationally shown that a the minimum distance goes as $\delta(t) \sim t^{1/2}$ scaling [44–53]. It has recently been shown [54] that there is a further scaling law for larger times, $\delta(t) \sim t$. This exchange is not conservative; as the reconnection occurs, the vortices release a sound pulse which adds density waves into the system [55]. In a system with a large amount of vortices, reconnections occur constantly. Due to the sound emission, the overall incompressible energy of the vortices in the condensate falls as it is converted to compressible energy associated with sound emission and a cascade of energy is observed; in a system where this happens again and again, this becomes vortex turbulence [14].

2.6 Turbulence

In this thesis we study quantum turbulence. In order to understand quantum turbulence, we must first have an understanding of the principles of classical turbulence. The Navier Stokes equations govern the flow of a classical fluid where for a system with density ρ, velocity $\mathbf{v}$, fluidic pressure p and viscosity ν,

$$\rho\frac{\partial \mathbf{v}}{\partial t} = -\rho(\mathbf{v} \cdot \nabla)\mathbf{v} - \nabla p + \rho\nu\nabla^2\mathbf{v}. \tag{2.84}$$

We start by a qualitative description of classical turbulence before introducing the mathematics. Classical turbulence is determined by the large scale driving of a system which creates eddies at a large length scale (eddies being a rotation of fluid; a tornado or a whirlpool). These large-scale eddies are inherently unstable due to the chaotic nature of three-dimensional turbulence and begin to break down

and "seed" eddies at smaller length scales. These eddies break further and further down until the smallest eddies where energy is dissipated by viscosity. it is useful to introduce a non-dimensional parameters known as the Reynolds number

$$Re = \frac{v\ell}{\nu},$$ (2.85)

where u is the typical velocity of the system at the large scale ℓ of the flow ν is the kinematic viscosity of the system. To a nonspecialist, the Reynolds number of a flow is what often tells the observer the nature of the flow being analysed. When it is small, the flow is smooth and laminar. When the Reynolds number of the system, however, rises then we begin to see the chaotic nature of flow. When $Re \to 1$, viscous dissipative effects cannot be neglected, implying that at small scales viscocity is important. At larger k scales, the only relevant phenomenon is ϵ. We define here the velocity and length scale of the largest eddies to be u and ℓ respectively and the velocity and length scale for the smallest eddies to be v and η. The rate of strain at the lowest scale is given by $s_{ij} \to u/v$. Another useful measure is the rate of dissipation of the energy at the small scalelength, η, which is defined by $\epsilon \to v s_{ij} s_{ij} = v(v^2/\eta^2)$. From this, we can define two useful relations which are used later on

$$\eta = \left(\frac{v_\eta^3}{\epsilon}\right)^{1/4},$$ (2.86)

and

$$v = (v\epsilon)^{1/4}.$$ (2.87)

We here derive two useful measures from classical turbulence which will be used in this thesis to study quantum turbulence. The first is the correlation function, specifically for the velocity of a turbulence system. The velocity correlation function is defined as the workhorse of turbulent theory by Davidson [3] and we will follow his derivations here. The velocity correlation function is defined as

$$Q_{ij}(r\hat{e}_x) = \langle v_i'(\mathsf{x})v_j'(\mathsf{x} + r\hat{e}_\mathsf{x})\rangle,$$ (2.88)

where the primed velocity fluctuation v' is the velocity at $\mathsf{x} = x, y, z$ minus the mean velocity of the system, and $\langle\rangle$ denotes the ensemble averaging. We now ignore primes for aesthetic reasons as assume the mean flow of our example system is 0. In real terms, the correlation of the system defines how similar the velocities at two locations separated by a distance r are. Describing this qualitatively, one can think of an arbitrary distance r and a size of an eddy R. If $r \ll R$, then it can be assumed the two points are well correlated. If, however, $r \gg R$, we can assume the correlation is small or negligible. We define a longitudinal velocity correlation function $f(r)$, where $Q_{xx}(r\hat{e}_x) = v^2 f(r)$. One can therefore define a scalelength, l to denote a measure corresponding

$$l = \int_0^\infty f(r)dr$$ (2.89)

or expressed differently,

$$l = \int_0^\infty \frac{\langle v_i'(\mathbf{x})v_j'(\mathbf{x} + r\hat{e}_\mathbf{x})\rangle}{\langle v_i'(\mathbf{x})v_j'(\mathbf{x})\rangle} dr. \tag{2.90}$$

Rescaling the correlation length may come across as otiose, however rescaling by the $v(\mathbf{x})^2$ provides a worthwile relative measure which is more workable for us for comparisons between systems and times, t. The quanity l provides a useful measure to define the length of the largest eddies in the turbulent system. In a system of decaying turbulent system, it can be assumed that as the size of the eddy grows smaller, the measure l will also. In this thesis, we now refer to $f(r)$ as the correlation function as it is more useful to our work than the strict correlation function $Q(r)$.

This correlation function, $f(r)$ can be useful to determine the map of the velocities of our hypothetical system of classical turbulence. Also useful would be to use this to gain a measure on how the kinetic energy of the system exists at every scalelength. We can define an incompressible kinetic energy spectra from the velocity of the system. According to Davidson, we must first begin by defining a longitudinal velocity increment,

$$\Delta v = v(\mathbf{x} + r\hat{e}_\mathbf{x}) - v(\mathbf{x}), \tag{2.91}$$

of which a second-order longitudinal structure function can be defined as

$$\langle [\Delta v]^2 \rangle = \langle [v(\mathbf{x} + r\hat{e}_\mathbf{x}) - v(\mathbf{x})]^2 \rangle. \tag{2.92}$$

Simple algebraic manipulation can show that the second order structure function and the correlation function are related by

$$\langle [\Delta v(r)]^2 \rangle = 2v^2(1 - f). \tag{2.93}$$

If we consider a infinitely large r,

$$\langle [\Delta v(r \to \infty)]^2 \rangle \to \frac{4}{3}\langle \frac{1}{2}k^2 \rangle. \tag{2.94}$$

If one stops thinking of eddy size and begins to think about wave numbers, it can be proposed that one can look at the Fourier Transform to identify contributions to the incompressible energies at different lengthscales. We can define this as the energy spectrum where

$$E(k) = \frac{2}{\pi} \int_0^\infty R(r)kr\sin(kr)dr. \tag{2.95}$$

We assume that the distribution of $\mathbf{v}$ globally is homogeneous and thus,

$$R(r) = \frac{1}{2}\langle \mathbf{v}(\mathbf{x}) \cdot \mathbf{v}(\mathbf{x} + r)\rangle. \tag{2.96}$$

When taking $r \to 0$, the incompressible energy of the system can be expressed as

$$\frac{1}{2}\langle [\Delta v]^2 \rangle = \int_0^\infty E(k)dk. \tag{2.97}$$

It can be stated that $\langle [\Delta v]^2 \rangle$ can be expressed as a universal function $\hat{F}(u, \ell, r, t, v)$. Through dimensional analysis, it can be shown that this can be reduced down to

$$\langle [\Delta v]^2 \rangle = v^2 F\left(\frac{r}{\eta}\right). \tag{2.98}$$

We obtain the Kolmogorov *two-thirds* law, which relates the longitudinal structure function to the length r and ϵ at scales dictated by $\eta < r < \ell$.

$$\langle [\Delta v]^2 \rangle = \beta \epsilon^{2/3} r^{2/3}, \tag{2.99}$$

where β is a dimensionless parameter roughly equal to 2. Rewriting Eq. (2.99) in terms of the incompressible energy, we obtain the famed *Kolmogorov five-thirds* law

$$E(k) = C\epsilon^{2/3}k^{-5/3}, \tag{2.100}$$

In classical fluids, $C \approx 0.76\beta$ as the Reynolds number goes to infinity [3, 56]; Sreenivasan predicts $C = 1.62 \pm 0.17$ [57].

2.6.1 Kolmogorov Turbulence in Quantum Fluids

We can split the wavefunction of our condensates, Ψ, into a density and a phase using the Madelung transform

$$\Psi(\mathbf{x}, t) = \sqrt{n(\mathbf{x}, t)} \exp is(\mathbf{x}, t), \tag{2.101}$$

where n and s denote here the density and phase of the quantum fluid, we can substitute this into the Gross-Pitaevskii equation derived earlier, Eq. (2.45), one can observe the results

$$m\frac{\partial \mathbf{v}}{\partial t} = -\nabla\left(\frac{1}{2}mv^2 + V + gn - \frac{\hbar^2}{2m}\frac{\nabla^2\sqrt{n}}{\sqrt{n}}\right), \tag{2.102}$$

and

$$\frac{\partial n}{\partial t} + \nabla \cdot (n\mathbf{v}) = 0. \tag{2.103}$$

In the limit of $\hbar \rightarrow 0$, this equation resembles the Navier Stokes equation introduced above in classical fluids. It can be proven that In the region of $k_D < k < k_\eta$, the energy transfer to the smallest (Kolmogorov) length scale, k_η is self-similar and the scaling of the incompressible kinetic energy scaling is $E \sim k^{-5/3}$, akin to that of turbulence in classical fluids. There also is another scale present in the system for a quantum system; an observable k^{-3} is present in the top pane of Fig. 2.5 between the k_ξ and k_ℓ, corresponding to the contribution on the scale of single vortex lines. Stalp *et al.* [58] argued that the vorticity of a quantum fluid (Helium-II in their example) is

$$\omega = \kappa L, \tag{2.104}$$

where κ is the quantum of circulation, $\kappa = h/m$, and L denotes the vortex line length per unit volume of the system. They then further assumed that the dissipation of the turbulence in liquid helium must be

$$\epsilon = v' \kappa^2 L^2. \tag{2.105}$$

From here the total turbulent energy of a system of size D is given by [59]

$$\begin{aligned} E &= \int_{2\pi/D}^{\infty} C\epsilon^{2/3} k^{-5/3} dk, \\ &= \frac{3}{2} C\epsilon^{2/3} D^{2/3}. \end{aligned} \tag{2.106}$$

Knowing that the dissipation of the system is related to the decay in energy over time, it can be shown that

$$\epsilon = 27 C^3 D^2 (t + t_0)^{-3}, \tag{2.107}$$

where t_0 is simply a constant. We can therefore use the proposed relation in Eq. (2.105) to find a relation on how the total vortex line length decays in time as

$$L = \frac{(3C)^{3/2} D}{\kappa v'^{1/2}} (t + t_0)^{-3/2}. \tag{2.108}$$

In the majority of literature revolving quantum turbulence, this is simplified down and presented as a relation to only the time, so that the vortex length length decays in time as

$$L \sim t^{-3/2}. \tag{2.109}$$

Kolmogorov turbulence has been numerically studied in multiple studies using both the GPE and vortex filament method [60] for quantum fluids. It has also been experimentally observed in liquid Helium with techniques including rotating propellers [61, 62], moving grids [63, 64], and wind tunnels [65]. In a condensate, the healing length is on a comparable size to the condensate's width (roughly $D/a_0 \approx 10^2$) compared to the largest Helium experiments with $\approx 10^{10}$ [66]. In a similar vein, vortices are easily imaged in the Helium using tracer particles [67]. One other distinct advantage of Helium is the ability to measure the local velocity (and hence gain the incompressible energy spectrum) via multiple methods such as Pitot tubes [61] and cantilever anemometers [62]. At this point, the reader may consider the clash in the discussion of quantised vortices and the idea of vortex size declining in characteristic size along the energy cascade: how can this picture hold in the presence of quantised discrete vortices? The answer is in polarisation of condensates; collectives of vortices come together and form a bundle of like sign vortices within a quantum fluid [68–72]; these polarised bundles will act as if they are a larger singular larger classcial eddy.

The theoretical prediction of the total vortex line length decaying as $L \sim t^{-3/2}$ has been observed computationally and experimentally in Helium systems [63, 64, 73–75]. Kolmogorov turbulence is yet to be observed experimentally in condensates.

2.6.2 Vinen Turbulence

Alongside the pseudo-classical turbulence discussed above, we know of another type of vortex turbulence within quantum fluids: Vinen turbulence. In some texts this is also referred to as ultra-quantum turbulence [76]. Predicted by Vinen [77–79] and observed experimentally in Helium [74, 76] it is often quantified by its lack of classical signatures [80–82]. Many numerical studies in condensates have detected the signatures of Vinen Turbulence, such as in a decaying multiply charged vortex [83] and a thermal quench [84] in a BEC. The determination of the type of vortex turbulence formed has been shown to be determined by the length-scale of the driving [85, 86], where if a system is driven at a length-scale of $> \ell$, a quasi-classical system is created whereas driving on the scale of $< \ell$ gives a system of Vinen turbulence; one difference between the two regimes is that of the decay of vortex length [87]. Another difference between Vinen and Kolmogorov turbulence is that of the polarisation discussed previously; Vinen turbulent tangles do not contain the bundles of like-sign vortices. A consequence of this is a lack of the $E(k) \sim k^{-5/3}$ observed in Kelvin turbulence. In this regard, the energy spectrum of Vinen turbulence is distinctively different to that of Kelvin turbulence. If the velocity field of a single straight vortex is defined as

$$\mathbf{v} = \frac{\kappa}{2\pi r}, \tag{2.110}$$

the corresponding energy spectra for a for a randomly oriented, non-polarised collection of vortices is

$$E(k) = \frac{\kappa^2 L}{4\pi} k^{-1}. \tag{2.111}$$

The tangled vortices in a Vinen system do not correlate or orientate themselves. Figure 2.5 shows the comparison between the two; where Kolmogorov turbulence exhibits the famous five-thirds law, Vinen turbulence has a smaller scaling of k^{-1}. Although not observable in both subfigures of Fig. 2.3, both results will contain the contributions of individual quantum vortices with a k^{-3} at the larger k scales. The decay of the total vortex length in the system is given as

$$L \sim t^{-1}. \tag{2.112}$$

2.7 A note on wave turbulence

As well as vortex turbulence, there is also turbulence relating to weakly interacting, nonlinear out-of-equilibirum, dispersive waves in a system - *wave turbulence*. Wave turbulence has applications in many areas of physics such as ocean mechanics [88] and the cosmology [89]. Nazarenko defines wave turbulence as *the out-of-equilibrium statistical mechanics of random nonlinear waves* and a system of waves rather than vortices. In a Bose-Einstein condensates wave turbulence can be studied in two scenarios, the first of which is as a turbulence of fluctuations on a background condensate. Assuming a condensate in a box with length L, the Fourier
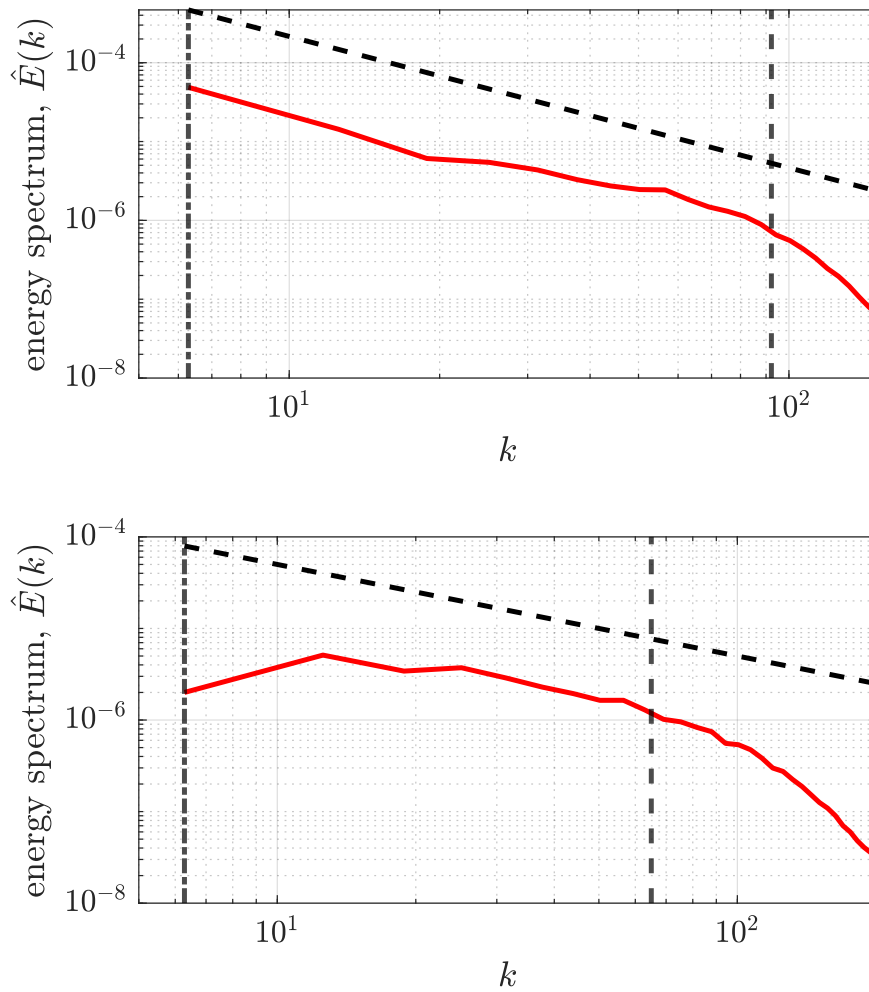
FIGURE 2.5: The incompressible energy spectra (Eq. (2.64)) for (top) Kolmogorov turbulence and (bottom) Vinen turbulence. Marked are the scaling laws, $k^{-5/3}$ (top) and k^{-1} (bottom) and the k values corresponding to the size of the domain D (dot-dashed) and the inter-vortex spacing ℓ (dashed).
Image produced from data provided by L. Galantucci.

transform of the wavefunction can be given as

$$\hat{\psi}_{\mathbf{k}} = \frac{1}{L^2} \int \psi(\mathbf{x}) \exp(-i\mathbf{k} \cdot \mathbf{x}) d\mathbf{x}, \tag{2.113}$$

where

$$\mathbf{k} = \left(\pm \frac{2\pi n_x}{L}, \pm \frac{2\pi n_y}{L}, \pm \frac{2\pi n_z}{L} \right) \tag{2.114}$$

where $n_{x,y,z} = [0, 1, 2, ...]$. The wave spectrum of this system is given as

$$n_{\mathbf{k}} = \frac{L^2}{4\pi^2} \langle |\hat{\psi}_{\mathbf{k}}|^2 \rangle. \tag{2.115}$$

Assuming that the fluctuations upon the condensate are very small and in a homogeneous, infinite box, one can therefore define

$$n_{\mathbf{k}} = 4\pi \int n_{\mathbf{k}_1} n_{\mathbf{k}_2} n_{\mathbf{k}_3} n_{\mathbf{k}} \left[\frac{1}{n_{\mathbf{k}}} + \frac{1}{n_{\mathbf{k}_3}} - \frac{1}{n_{\mathbf{k}_1}} - \frac{1}{n_{\mathbf{k}_2}} \right]$$
$$\delta(\omega_k + \omega_{k_3} - \omega_{k_1} - \omega_{k_2})\delta(\mathbf{k} + \mathbf{k}_3 - \mathbf{k}_1 - \mathbf{k}_2) d\mathbf{k}_1 d\mathbf{k}_2 d\mathbf{k}_3. \tag{2.116}$$

The term ω_k here is the dispersion relation

$$\omega_k = k^2. \tag{2.117}$$

Solutions to Eq. (2.116) are given in the form of

$$n_k = Ck^\alpha, \tag{2.118}$$

where C is a constant, and α denotes a scaling factor. For the direct energy cascade, as measured experimentally in Ref. [11], is given as $\alpha = -3$. Secondly, one can study the effects of kelvin waves on a vortex in a quantum fluid, where six-wave processes conserve both wave action and energy [90]. This mechanism - that of kelvin waves upon vortices - is thought to be very important to the final state of vortex turbulence [91].

2.8 Experimental Techniques

The rational for studying turbulence within a Bose-Einstein condensate is only possible due to experimental achievements and advancements. It is therefore imperative for theorists to understand the basics of experimental procedures both the physically inherent and contemporaneous limitations of experimental setups. Some theoretical papers (whether that be focusing on turbulence or other aspects of cold atoms studies) are published with results that are not experimentally repeatable with the current generation of cold atom experiments. Examples include systems with a very large homogeneous background density or in the measurement of velocity fields. In this thesis I aim to explore the type of turbulence obtained from the current level of experimental cold atom turbulence research and propose possible methods which are viable for current experimentalists. We therefore, here,

provide an investigation of current experimental methodologies, written for a theorist in mind. We focus our attentions on the techniques of the Sao Carlos group, however also bring to light other experimental procedures.

2.8.1   Cooling and trapping of atoms

The thermal energy of an individual particle per degree of freedom as a function of temperature, T, is

$$E = \frac{1}{2}k_B T. \tag{2.119}$$

We can equate this relation to the particle kinetic energy, i.e.

$$\frac{1}{2}mv_x'^2 = \frac{1}{2}k_B T. \tag{2.120}$$

The route-mean-squared velocity, v_{rms}, in three dimensions can therefore be found to be

$$v_{rms} = \frac{\sqrt{3k_B T}}{m}, \tag{2.121}$$

such that the the slower the atoms in the sample, the colder they become. Originally proposed by Hansch and Schawlow [92], one can use this correspondence as the basis for laser cooling, the first step in an experiment. When the frequency of a laser is close to an atomic transition the absorption of the light by the atoms causes a transfer of momentum, thus changing the kinetic energy of the atom. This implies a slowing down of the atom in the given direction and thus it begins to cool. In an experiment, this is applied in the three cartesian directions to cool the gas of atoms. This is often referred to as an optical molasses [93]. There is a limit to the cooling one can achieve in this setup called the "Doppler cooling limit",

$$T_D = \frac{\hbar\Gamma}{2k_B}, \tag{2.122}$$

where T_D is the Doppler temperature. For an example, one can cool a sample of Sodium down to $T_D = 240\mu K$ using the optical molasses technique. The optical molasses technique is not able to cool the sample enough to undergo condensation. After the molasses cooling in the magneto-optical trap (MOT), the sample is transferred to another trap so that the sample can undergo evaporative cooling. If one has a large sample of atoms, there will be a large range of temperatures (and therefore energies) present. Evaporative cooling, unlike that of the optical molasses, has no mathematical lower limit to temperatures achieved [94]; the lowest temperature possible is instead dictated by the experimental apparatus and discretion of the experimentalist.

The "typical" bosonic condensate is trapped within a magneto-optical trap where the shape of the potential gives a non-homogeneous shape to the condensate. One can use optical techniques to create a hard-box (and ergo has a quasi-uniform background) condensate in two and three dimensions [10]. Another semi-recent advancement of trapping involves a Digital Micrometer Device (DMD) [95], where one can project an arbitrary 2D greyscale image onto a condensate, giving an infinite number of combinations of condensate shapes.

2.8.2 Generation of turbulence

As shown in Section 2.6, there have been multiple theoretical and computational proposals for creating turbulence within a cold atomic system. At the time of writing, however, all experimental realisations of quantum turbulence in an atomic system have been achieved by a large scale driving of the condensate. We give a particular focus on the experiment of the Sao Carlos group in Brazil.
The Sao Carlos experiment took the proposal of Kobayashi and Tsubota [96] to use two separate rotations in a trapped system [97]. With the equipment available to them, they used the concept of the transfer of angular momentum via external magnetic traps. A pair of anti-Hemholtz coils is applied in addition to the background harmonic potential, placed at an off-angle (roughly $\theta = 5°$ to the trap axis). These coils are driven from 0 to the maximum in an oscillatory fashion, $I(t) = I_0[1 - \cos \Omega t]$ [41]. A small amplitude of excitement gives various oscillation modes (dipole, monopole, scissor etc.). Above a given maximum amplitudes, vortices are formed, then turbulence and then a final state of granulation [98], defined as very small, spatially and phase separated bits of condensate. The fluctuations and driving during the creation of granulations means that our Gross-Pitaevskii framework employed in this thesis is not suitable; the mean-field Gross-Pitaevskii equation assumes that the number of particles in the system is large and the system is weakly interacting - very small fragmented parts of condensate therefore cannot be assumed to be well modelled. Therefore, granulation is not studied here. After the system has been driven, the condensate is left in the original harmonic trapping potential for 20ms, before being released and imaged.

2.8.3 Imaging of condensates

The imaging of two-dimensional system has obviously provided more advanced results compared to their three-dimensions counterparts. Here, vortices can been shown *in-situ* [99] with multiple image captures taken from the same experiment. Identification of the sign of vortices in a turbulent 2D condensate using Bragg scattering [100]. Imaging in 3D systems is inherently much more difficult, but recent advancements have been made. One such example is the use of absorption imaging to visualise the reconnection of two vortices in a 3D cigar shaped condensate [101]. Nevertheless, imaging of 3D condensates remains a challenge, especially if one wishes to view a turbulent condensate. We will briefly reflect on the method of absorption imaging, with focus on the Sao Carlos experiment.
An experimentalist will typically release a condensate from the trapping potential to visualise it; the density of the condensate will fall and any phase defects (solitons, vortices) will grow at a larger rate than the condensate; resulting in easier observation of them. As a condensate expands outwards, a collimated laser beam will be shone onto the sample. This beam will be resonant with one of the electronic transitions of the imaged atom species. As the beam passes through the condensate, some of the photons will be absorbed and scattered whereas some will pass straight through. This results in a "shadow" image of the condensate, where the absorption is proportional to the shape of the density profile of the system. Multiple images are taken. As well as an image of the cloud, an image of the imaging beam is taken. Secondly, a "dark" image is taken, to negate any errors in the system

(such as in the camera or any arbitrary light in the system). The resultant image is known as an absorption image, which is an image of the density, integrated in the direction of imaging,

$$n_{2D}(x,z) = \int n(x,y,z)dy. \tag{2.123}$$

Some experimental setups can image from more than one direction at the same time, however the Sao Carlos experiment cannot. Assuming the condensate is uniform in the xy plane, one can make use of techniques such as the Abel transform to create an estimated 3D profile of the cloud [8]. As well as a way of observing the condensate itself, images from experiments can be used to estimate the number of particles in the condensate by simply taking the norm,

$$N = \int n_{2D}(x,z)dxdz. \tag{2.124}$$

Also obtainable is the temperature of the system. When one is able to image the expansion at a few different times, one is able to gain the velocity of expansion. From this one can relate it to the temperature of the sample,

$$\frac{3}{2}k_B T = \frac{1}{2}mv^2, \tag{2.125}$$

where v is the velocity of the condensate. When imaging, one can obtain what is referred to as a bimodal distribution; if the temperature of the system is high, one can see both the condensate in the shape of a Thomas-Fermi profile surrounded by the Gaussian shape of the thermal atoms. A useful measure obtained from the integrated image is that of the momentum spectra, of which for a turbulent system can contain a scaling law.

3 Computational Approaches for Three-Dimensional Condensates

In this chapter, we explain and derive the computational methods used in this thesis. To develop a code that both is able model the large driving of condensates and also run on very large computational domains to model the Time-Of-Flight of the system, we had to ensure the computational method is as robust and efficient as possible to provide accurate, workable results in a practical timescale. The code used to model all the work in this thesis was built upon an open-source GPE code by George Stagg [102]. During this thesis, the codes were ran on Newcastle University's High Performance Computer ROCKET where we could benefit from developing a highly-parallelised code to ensure it can run as effectively as possible.

3.1 Solving Partial Differential Equations

There are many ways where one can can solve a partial differential equation like a Gross-Pitaevskii equation. For a discrete computational grid, we can split the grid into spaces of `dx` and increment the solution forward in steps of `dt`. One popular method is the split-step Fourier method, where if one knows the wavefunction at time t, then one can calculate the wavefunction after the next time step $t + $ `dt`. In these examples we will express the GPE in the natural form (Eq. (2.73)). We define our spatial domain as

$$\mathbf{x} = \mathtt{dx}[-\mathrm{NX}/2 : \mathrm{NX}/2] \tag{3.1}$$

where NX is a integer and the length of the domain is $\mathrm{NX} + 1$ points long. When defining our computational method we must also contemplate boundary conditions. If we are to model the expansion of a condensate, the wavefunction will obviously move outwards and thus boundary conditions can be an issue. The expanding wavefunction and the reflection from the edges collide, beating begins to occur and oscillations are seen near the edge of the computational domain. Although very small at first, this effect begins to build up. In time, this causes a mis-shaping of a spherically shaped condensate as the condensate becomes large. Therefore, we have to ensure that the computational box is much larger than the expansion we wish to simulate. We keep to periodic boundary conditions, such that for the edges of our domain,

$$\mathbf{x}[-NX/2 - 1] \to \mathbf{x}[NX/2], \tag{3.2}$$

and

$$\mathbf{x}[NX/2 + 1] \to \mathbf{x}[-NX/2]. \tag{3.3}$$

We use here the fourth-order Runge-Kutta method which is the sterotypical one used in such simulations. Provided one chooses an appropriate spatial step, dx and time step dt, any Schrodinger equation can be we simulated to the RK4 method. Returning to Eq. (2.73), we can denote a value k_1 as the "right-hand side" of the GPE so that,

$$k_1 = \psi(t),$$
$$= \frac{1}{i}\left[-\frac{1}{2}\nabla^2\psi + |\psi|^2\psi + V\psi\right] \tag{3.4}$$

$$k_2 = \psi\left(t + \frac{\texttt{dt}}{2}, \psi + \texttt{dt}\frac{k_1}{2}\right), \tag{3.5}$$

$$k_3 = \psi\left(t + \frac{\texttt{dt}}{2}, \psi + \texttt{dt}\frac{k_2}{2}\right), \tag{3.6}$$

and

$$k_4 = \psi(t + \texttt{dt}, \psi + \texttt{dt}k_3), \tag{3.7}$$

One therefore states that the wavefunction at the next time step is a summation of Eqs. (3.4) to (3.7),

$$\psi(x, y, z, t + \texttt{dt}) = \frac{\texttt{dt}}{6}(k_1 + 2k_2 + 2k_3 + k_4). \tag{3.8}$$

The ∇^2 term, signifying the second order spatial differential can be calculated on a discrete grid by finite differences with a large order of accuracy [103]. For each spatial direction $\nabla^2 \to \frac{\partial^2\psi}{\partial x^2}$, this term is

$$\frac{\partial^2\psi}{\partial x^2} \approx \frac{1}{12\texttt{dx}^2}[-\psi(x-2) + 16\psi(x-1) - 30\psi(x)$$
$$+ 16\psi(x+1) - \psi(x+2)] + \mathcal{O}(\texttt{dx}^2). \tag{3.9}$$

Usually, simulations use a "$[-1, 0, 1]$" grid

$$\frac{\partial^2\psi}{\partial x^2} = \frac{1}{\texttt{dx}^2}[\psi(x-dx) - 2\psi(x) + \psi(x+dx)], \tag{3.10}$$

for the laplacian term, however this was shown to not have the required accuracy for the work in this thesis (explained in Section 3.3). The ∇^2 term for the edges of the condensate is treated via the boundary conditions stated in Eqs. (3.2) and (3.3). The discretisation of the computational domain is such that dx is set to half of the healing length of the system, dx=0.5ξ and dt chosen to be an appropriate ratio of dt/dx^2.

 The first step in any computational simulation is to find the ground state of the system. To do this we must make a first initial guess of a condensate shape. We recall the Thomas-Fermi density profile defined in Eq. (5.4) and use this as a initial guess. One method of thus finding the ground state of the given system from this is using the imaginary time method where one substitutes the time $t \to t - i\Delta t$, where i is the imaginary number. Given the Thomas-Fermi profile, it can be imagined as a superposition of eigenstates. When running this through imaginary time,
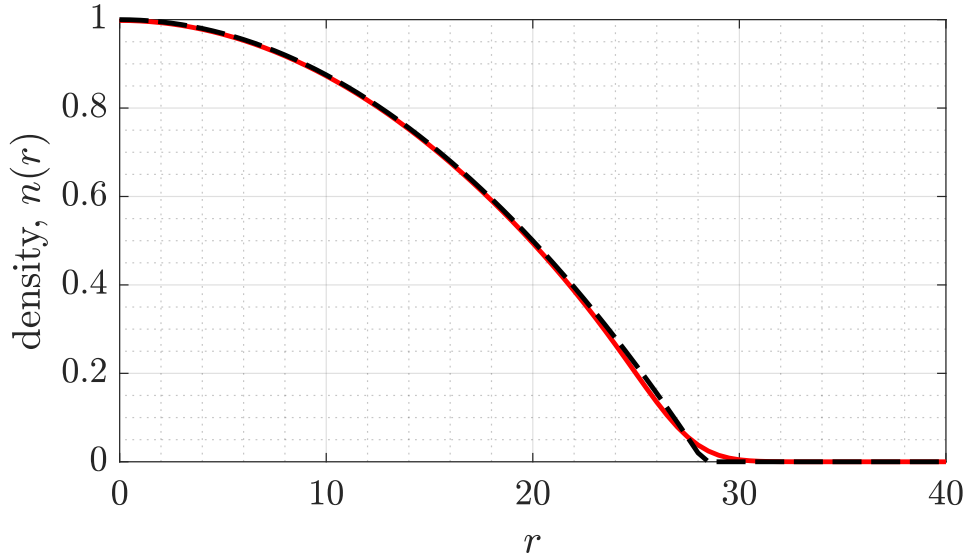
FIGURE 3.1: The density slice $n(x > 0, y = 0, z = 0)$ of the initial Thomas-Fermi profile of a spherical condensate (dashed black) and the corresponding ground state (red) ran to a tolerance $\delta E = E(t + \delta t)/E(t) = 10^{-10}$, where E is the total energy of the system. The condensate is normalised such that the peak density $n_0 = n(0, 0, 0) = 1$.

all the eigenstates will decay, with the ground state delaying slowest. Therefore, if running in imaginary time and ensuring the norm of the system is conserved, we will be left with the ground state of the condensate - the lowest energy mode. Figure 3.1 shows both our initial guess and the ground state of the system; the only discernible difference is along the edges of the condensate.

We need to decide when we have a good enough ground state to use in our simulations; we can either monitor the change in the norm of the system, or the total energy of the system (which we use in this work). We monitor the change in energy over time $\delta E = E(t + \Delta t)/E(t)$ until it falls beneath a given tolerance. If the tolerance is too high, there will be too much excess energy in the system, leading to the triggering of modes and density oscillations. In Fig. 3.2, we show how in time this can happen; in the right pane where the total energy of the ground state oscillates for the two largest tolerances to a large degree. This is due to excess energies still left in the simulation.

3.1.1 Adding in Vortices

No true analytical solutions for vortices exist but various approximations exist. One such well known one that is often used in analytical prediction of the density profile of a vortex along the z direction in cylindrical coordinates, $r = \sqrt{x^2 + y^2}$, is given as

$$\psi(r, z) = \sqrt{\frac{r}{1 + r^2}} \exp\left(i\kappa\theta\right), \tag{3.11}$$

where κ is the circulation and θ is the azimuthal angle around the vortex core. In this thesis we instead use the approximation given by Berloff [104], where the
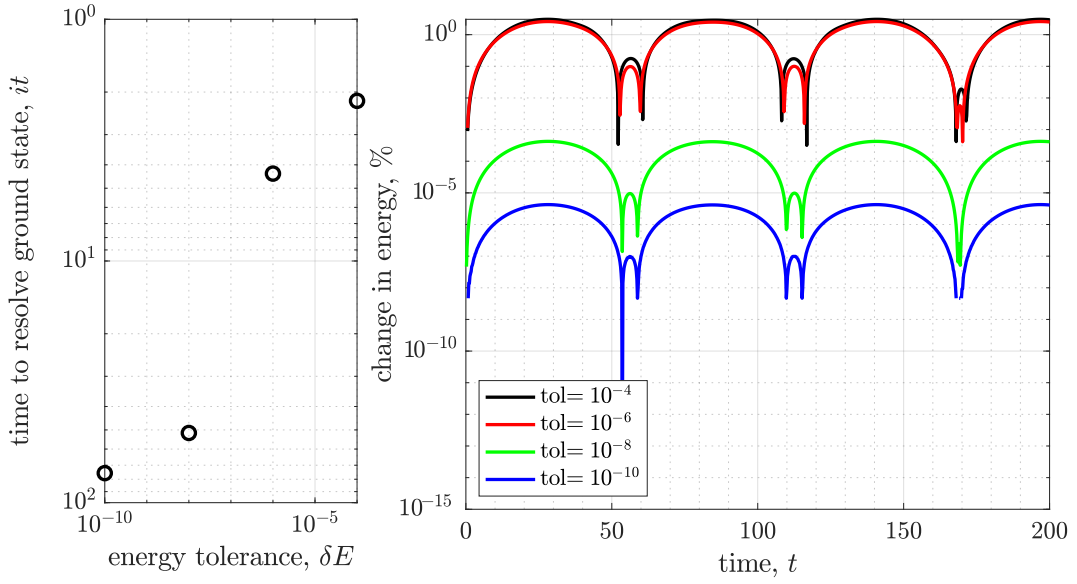
FIGURE 3.2: The simulated time (in the natural units derived earlier in Eq. (2.73)) to find the ground state of the system as a function of the given energy tolerance (left) and the change in the total energy when the ground state is ran in real time over a time of $t = 200$ for various tolerances.

resulting approximation of the density of a straight line vortex in an infinite system is given as

$$\psi(x,y,z) = \sqrt{\frac{r^2(0.3437 + 0.0286r^2)}{1 + 0.3333r^2 + 0.0286r^4}}. \tag{3.12}$$

A vortex does not have to just be a straight line but can be in the shape of a ring, where the ends terminate on each other. This approximation can be adapted for such a topology. If we assume the ring is aligned to the x, y plane and perpendicular to the z plane, with a given radius r at a location x_0, y_0 and z_0. To computationally add in the vortex ring, we define a wavefunction which can me multiplied into the intended ground state of the system. As well as a vortex line, Berloff's approximation can be reworked into describing a vortex ring in a homogeneous system such that

$$\psi(x,y,z) = \psi(x,y,z)\sqrt{\frac{r_1^2(0.3437 + 0.0286r_1^2)}{1 + 0.3333r_1^2 + 0.0286r_1^4}}\sqrt{\frac{r_2^2(0.3437 + 0.0286r_2^2)}{1 + 0.3333r_2^2 + 0.0286r_2^4}} \tag{3.13}$$
$$(z + i\kappa S + r)(z - i\kappa S - r)$$

where

$$r_1 = \sqrt{(z - z_0)^2 + (\sqrt{x^2 + y^2} + r_0)^2}, \tag{3.14}$$

and

$$r_2 = \sqrt{(z - z_0)^2 + (\sqrt{x^2 + y^2} - r_0)^2}. \tag{3.15}$$
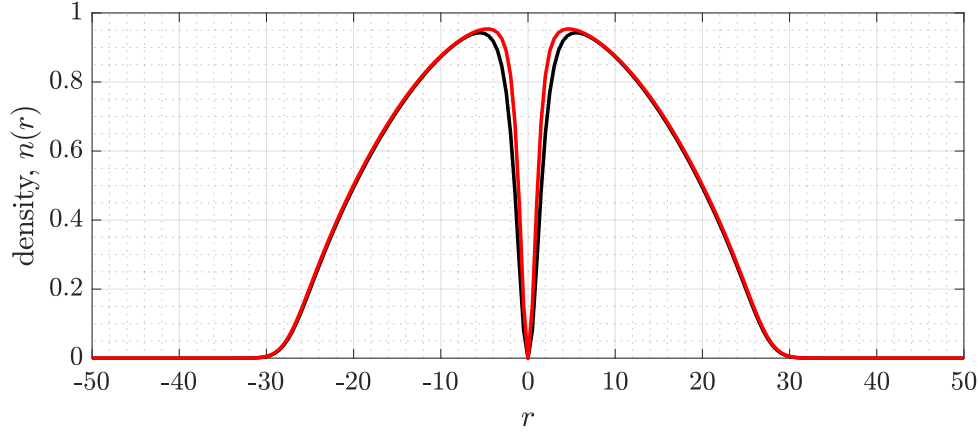
FIGURE 3.3: The one dimensional slice of the initial density approximation (Eq. (3.12)) of a vortex line through the centre of a spherical condensate (black) and the same condensate ran in imaginary time to a tolerance of 10^{-8}.

We add in vortices and then run through imaginary time again so that the vortex state converges. Akin with the ground state solution, the given approximation will converge to the lowest energy state. When looking for the ground state, running through imaginary time will converge to the true ground state of the system if left to run in infinite time (provided the wavefunction is normalised at every step). The only choice one has to make is how low a tolerance to go to is the time in which it'll take to get there. We have to be careful, as a line vortex placed in a trapped system running in imaginary time will move, and a ring vortex will shrink. Conversely, a system with a vortex ran to too high a tolerance once ran in real time will result in density waves emanating from the vortex core. We therefore have to be careful in which tolerance we choose and run a few tests to make sure any vortex states we create are as converged as possible. We look at two cases for two specific reasons. Firstly, we look at a line vortex placed within the centre of a spherical condensate ran to a few different energy tolerances. If not a good enough approximation, there will be an introduction of compressible (sound wave) energy into the system. We monitor this and see how the ratio of the compressible to incompressible energies change when the system is ran in real time, as shown in Fig. 3.4. We find that a tolerance of 10^{-6} gives a sufficient lack of creation of compressible energy. The final test is when a vortex is placed off-centre in the same spherical condensate; a vortex is placed at $(x, y, z) = (5, 0, 0)$ with the system then ran in imaginary time. Unlike in the previous two cases, this cannot be ran for an infinitely small tolerance as the vortex will leave the system. If we monitor the location in the x direction as a function of the energy tolerance the system has been ran to (see Fig. 3.5) for three different locations in y then we see this shifting; very quickly, the location of the vortex in x has changed. We have to weigh up the creation of density fluctuations and the placement of vortices and therefore decide to run any vortex codes for a tolerance of $\Delta E / E = 10^{-6}$.
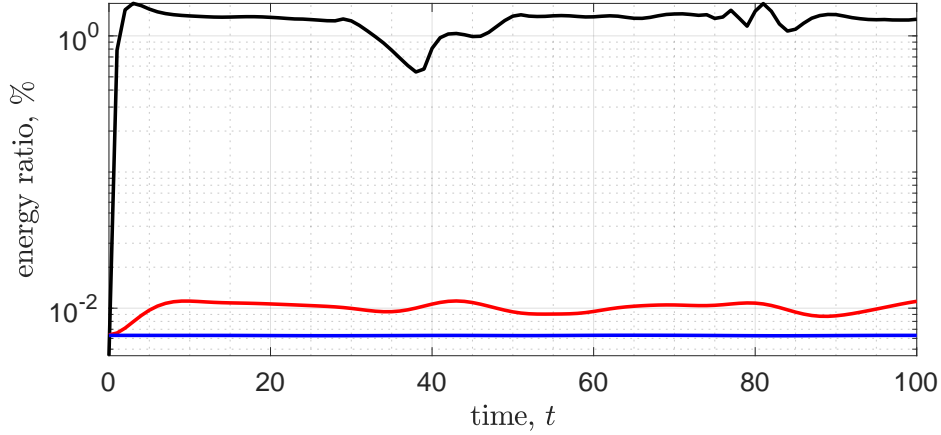
FIGURE 3.4: The ratio of the compressible energy created from the shedding of energy from a vortex ran to a tolerance of 10^{-4} (black), 10^{-6} (red) and 10^{-8} (blue).

3.2   Detection of vortices

Vortices are detected in our condensates using an adapted method from Villois *et al.* [105] and Galantucci *et al.* [101]. Two dimensional slices of the three-dimensional wavefuction are used to pinpoint the locations of vortex points within them using these slices. The algorithm calculates the pseudovorticity unit vector of the two dimensional slice,

$$\hat{\omega} = \frac{\nabla \Re e(\psi) \times \nabla \Im m(\psi)}{|\nabla \Re e(\psi) \times \nabla \Im m(\psi)|} \tag{3.16}$$

where $\Re e(\psi)$ and $\Im m(\psi)$ denote the real and imaginary part of the wavefunction. Where this is larger than a ratio of 2π, and the density is lower than a ratio of the peak density of the system (denoting the existence of an empty vortex core), it decides the location of the vortex core in the 2D space. Using a steepest descent algorithm, it can then work out which cores in each 2D slice correspond to the same 3D vortex, and can also obtain locations at a sub-grid resolution. From this, one ends up with 1D arrays of locations corresponding to the core of the 3D vortex; from this information, the length, locations and topologies of the individual lines can be found, as well as the total line length of the condensate and the minimum distances between the vortices.

In Chapter 6, the condensates generated contain many vortices as well as large density fluctuations and fragmentation. To avoid the extraneous detection of the large fluctuations as vortices, we calculate the correlation length of the density fluctuations first. This quantity is found by computing the correlation lengths $\chi_{\mathbf{x}}$ ($\mathbf{x} = x, y, z$,t) of the condensate's density fluctuations at time t in the three Cartesian planes, defined as

$$\chi_i(t) = \int_0^\infty \frac{\langle n_{fl}(\mathbf{x}, t) n_{fl}(\mathbf{x} + \mathbf{e_x} \cdot r, t) \rangle}{\langle n_{fl}(\mathbf{x}, t)^2 \rangle} dr, \tag{3.17}$$
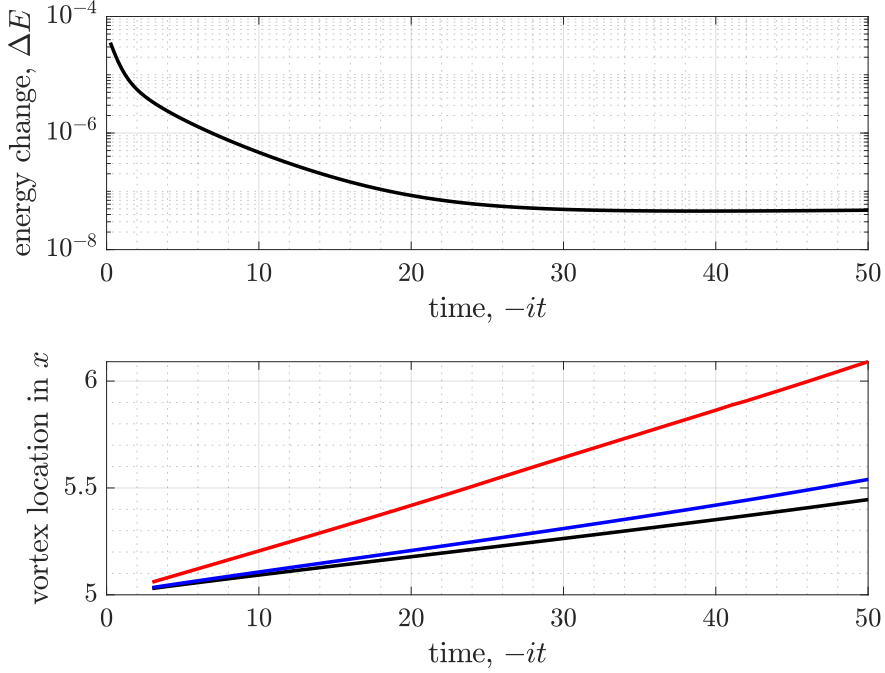
FIGURE 3.5: The change in energy (top) of a vortex placed at initially at $x = 5$ ran in imaginary time, and the vortex location in x at $z = 0$ (black), $z = 0.25R_z$ (blue) and $z = 0.5R_z$ (red).

where n_{fl} is the density of the condensate with a fitted Thomas-Fermi profile removed, $n_{fl} = n - n_{TF}$, and $i = (x, y, z)$. The overall correlation is then defined as $\chi(t) = (\chi_x(t) + \chi_y(t) + \chi_z(t))/3$. If the algorithm detects a vortex in a location where the local correlation length is as given ratio smaller than the average correlation length of the system, it is ignored and defined as a fragmentation of the condensate density.

3.3 Expansion of Condensates

In this thesis we model the time-of-flight of condensates in order to quantify both how the structure within a condensate affects its expansion and the how the nature of an expansion may give an experimentalist a better idea to what is inside the condensate when it is released. This poses an instant issue to anyone who wishes to model this expansion computationally. We recall that it was stated earlier that the computational dx of the system is kept to $\xi_0/2$, where ξ_0 denotes the healing length at the peak density, n_0. With the healing length at $n \neq n_0$ being larger than this value, this ensures that the system is well sampled and therefore well modelled. This is a problem when wanting to expand the condensate; a simulation to accurately describe the expansion on the same scale as an experimental TOF will need to expand to ten times the original width of the condensate. An ordinary spherically shaped condensate with a width typical of the condensates presented in this thesis would require a computational grid of $\sim 1500^3$. This is extremely

costly both in terms of storage and CPU time (even with the use of the university HPC and adequate usage or parallel computing). There is, however, an approach one can implement. Thinking of the peak density of a system with Thomas-Fermi widths defined in the three Cartesian direction, the peak density of a Thomas-Fermi profile is given as

$$n_0 = \frac{8\pi}{15} \frac{N}{R_x R_y R_z} \tag{3.18}$$

Defining now a dimensionless scaling factor b (where the Thomas-Fermi in time is expressed as $R_{\mathbf{x}}(t) = b_{\mathbf{x}}(t) R_{\mathbf{x}}(t = 0)$, we know that as $b(t)$ increases, the peak density will change by

$$n_0(t) = \frac{n_0}{b_x(t) b_y(t) b_z(t)}. \tag{3.19}$$

If the individual widths increase to twice the original size, the peak density will fall and the healing length at the peak of the system will double. Using this, we can therefore remesh the wavefunction onto a new, courser, grid once the healing length has doubled. The concept of remeshing has been deployed in many areas of physics [106], such as in transport equations [107], astronomy [108] and geophysics [109]. While testing, many methods where tried, some more advanced than the others. Interestingly, the simplest method is both very effective and resulted in the fastest computations.

Remeshing algorithm:

- A condensate which we wish to measure the expansion of is produced in a computational grid defined with $\mathtt{dx} = \xi/2$, on the computational grid from Eq. (3.1). The peak density at $t = 0$ is calculated by taking an average of the largest 5% of the points of the density with the value kept as $n_{(t=0)}$.

- The potential of the system is set to zero, $V = 0$ so the condensate spreads out in a way derived later in Eqs. (5.16) and (5.17).

- The peak density is monitored at every 0.1 time units (again by taking an average of the largest 5% of the points of the density).

- Once this peak falls to a given ratio of the original peak density, we state that the healing length grown large enough.

    - For a spherical condensate, this ratio is that the peak density has fallen to 1/8th of the original value at $t = 0$. For a cigar condensate, we instead use a 1/16th - the anisotrophy of the expansion means that the z direction for the cigar condensate with $\omega_z > \omega_{x,y}$ expands slowly comapred to the radial direction.

- A new computational box, $\mathcal{X}_1$, is defined with $dx = 2dx_0$ and $\mathtt{x} = d\mathtt{x}[-NX/2 : NX/2]$.

- Every second point in the original wavefunction,

$$\mathcal{X}_0([-NX/2, -NX/2 + 2, ..., -2, 0, 2, ..., NX/2 - 2, NX/2]) \tag{3.20}$$

is placed within the new wavefunction at

$$\mathcal{X}_1([-NX/4, -NX/4+1, ..., -1, 0, 1, ..., NX/4-1, NX/4]) \qquad (3.21)$$

- The areas of the grid where

$$\mathcal{X}_1([-NX/2, -NX/2+1, ..., -NX/4-2, -NX/4-1]) \qquad (3.22)$$

and

$$\mathcal{X}_1([NX/4+1, NX/4+2, ..., NX/2-1, NX/2]) \qquad (3.23)$$

are seeded with very small complex randomised noise on the scale of 10^{-10}. Although not needed for the background expanding condensate, it helps ensure that the phase profile of vortices is quickly adapted into the new area of the computational domain. It was found that if the wavefunction at locations denoted in Eqs. (3.22) and (3.23) were simply set to zero, the phase winding of vortices developed a discrepancy.

- The wavefunction in the new grid is renormalised and the GPE continues.

- By the time the condensate bulk expands into the domain denoted in Eqs. (3.22) and (3.23), the phase profile is as well defined as if the simulation was ran on a hypothetical grid of $dx_0[NX, NX+1, ..., NX-1, NX]$.

To ensure that the reader agrees with us that the remeshing algorithm works, we present a test case of a spherical condensate expanding with a single straight line vortex through the centre of the condensate. We run this in an ordinary computational grid and on a computational grid that remeshes. We see in Fig. 3.6 that both the total energy of the system and the individual energies of the system have a percentage difference of lower than a single percent. It must also be stated that there will be a slight error in the measurement of the energies themselves; since the integration and differentiation methods used to calculate the energies presented here rely on the dx value themselves, a certain amount of error will be due to that difference. Indeed, if one measures the energies of the original grid only analysing every second point, one finds that the percentage difference between the energies measured on the remeshed grid and the sampled original grid is much smaller than the one presented in Fig. 3.6.

As well as the energies, we must also study how if the shape of the condensate is affected by the remeshing. Here, it must be stated, that we originally wrote the algorithm to remesh constantly. It was found, however, that the simulation would break down and the condensate would begin to take on a more squarish shape if remeshed a second time; we thus remesh the grid of the simulation only once. This limits our level of expansion, however with our computational resources we are still able to observe an expansion of ~ 15 times the original condensate's size.

Figure 3.7 shows a 1D slice of the density of the expanding spherical condensate with a vortex through the centre at a time $t = 60$. We see no difference between the two simulations, the only noticeable difference is towards the edges and even then is negligible. Now we know we can expand our condensate to a reasonable degree with our adaptive grid, we can conclude that we have all the computational resources to study both the expansion of condensates with systematically placed
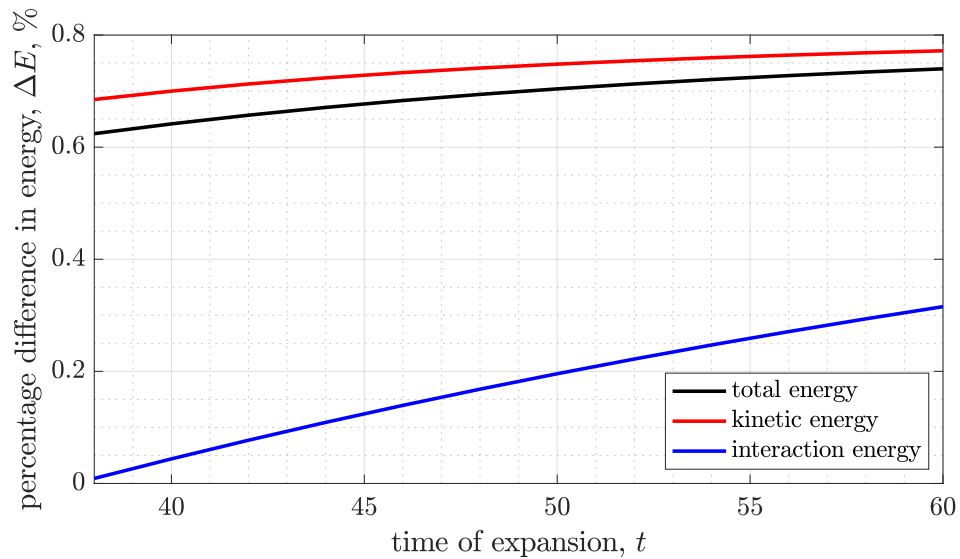
FIGURE 3.6: The percentage difference, $\Delta E(t)$, calculated from the difference between in the individual energies between two simulations (one remeshing, one not) of an expanding spherical condensate with a vortex in the centre on a ordinary computational grid and a remeshing one. The remeshing point happens at $t = 38$, on the left edge of the graph.
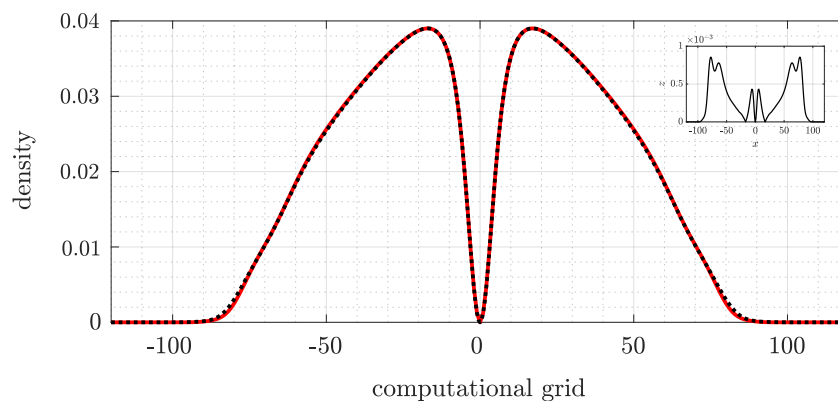
FIGURE 3.7: The one dimensional density slice of an expanding spherical condensate with a single line vortices in the centre of the condensate at $t = 60$ on an ordinary computational domain (black dotted) and remeshing computational domain (red). Inset is the percentage difference between the two, highlighting the very small difference between the two densities.

vortices and density fluctuations and also the generation of turbulence (and the expansion of such cases!).

4 Creation and measurements of solitons in One-Dimensional Condensates

We begin the research of this thesis by using 1D systems as a test case. We first begin by deriving a new method of measuring the speed of a soliton in a condensate. The results of this Chapter was published in Europhysics Letters [13].

4.1 Detection of solitons in 1D systems

Quantifying the nature of turbulence in a three-dimensional (3D) Bose-Einstein condensate requires a way of identifying individual phase defects present in the system. Quantum turbulence proves to be an experimental challenge. Such an entangled 3D system provides a difficult system to optically image; if the individual vortices are not aligned with the direction of visualisation then they are barely visible within the turbulent cloud. This work was concluded as a test-bed to create a method of detecting phase defects in condensates. We hence take a step back and begin our journey with the study of one-dimensional (1D) repulsive Bose-Einstein Condensates and the dark solitons within them. Solitons are present in many nonlinear systems, from optics [110–112], thin films [113, 114] and fluids [115–117] to atomic BECs [21, 30, 31, 118–129]. Multiple methods of creating dark solitons [37, 130, 131] were proposed shortly after realisation of BECs [132–135] and the subsequent creation of low dimension condensates [136]. These methods can be broken into two categories: phase imprinting [30, 31, 121, 137] and density engineering [122, 124, 131], and also a combination of the two [129, 130]. Recently, new methods to create solitons [138] through quenching have also been discussed [139, 140]. Dark solitons are stable in BECs confined in quasi-1D geometries, at $T = 0$, and under certain specific forms of trapping potential, such as a harmonic trapping potential [141]. If any of these constraints are broken, the solitons are prone to decay, due to unstable excitation of the dark soliton into vortex rings/pairs (the snake instability) [32, 118, 142–146], thermal dissipation [27, 147, 148], and net sound emission [23, 24, 26, 141], respectively. The first generation of dark soliton experiments in BECs showed the possibility of non-dispersive solitary waves propagating through the background condensate [30, 31, 118, 132, 137]. In these particular experiments, propagation was very short-lived. Dark solitons were shown to break down quickly due to a mixture of thermodynamic and dynamical instabilities which occurred if the background density was not strongly enough within the quasi-1D regime [143]. Unlike theoretical work based on the 1D mean field limit, experimental quasi-1D condensates consist of cigar-like clouds of trapped atoms

in which a strong radial confinement prevents excitations in the radial plane. The second generation of experiments were able to both keep the condensate cold and confined enough in the radial directions to sustain dark solitons for long periods (that is, for at least one oscillation of the soliton) [121, 124]. Notable experiments include verification of the oscillation frequency of the soliton in a harmonic trap being $\omega/\sqrt{2}$ (where ω is the trapping frequency of the 1D system) for systems consisting of a single soliton [124, 149] and the deviation from this prediction for multiple soliton systems [124]. Interesting theoretical models include the study of interactions of multiple dark solitons [150, 151] and solitons in two-component systems [152–154]. Analysis of the complex structure present in a condensate - be that a single vortex/ soliton or quantum turbulence [7, 11, 20, 155] - requires accurate detection of the density. Techniques to image the density of the condensate include dispersive methods [156], absorption [157, 158] and phase-contrast imaging [159, 160]. Each technique has its own advantages and disadvantages; the choice is made depending on the type of experiment taking place. Imaging happens either *in situ* (that is, imaging the trapped condensate) or during a time-of-flight (TOF) expansion (releasing the condensate from the trap). Absorption methods, either *in situ* or after TOF expansion, are inherently destructive - due to the heating of the condensate by the imaging laser and the loss of the condensate in the case of TOF imaging. The viability [161] and search for minimally/ non-destructive imaging techniques has been an active topic recently [95, 99, 100]. A particularly effective method of imaging the condensate with minimal destruction of the sample called Partial Transfer Absorption Imaging (PTAI) was experimentally demonstrated by Freilich *et al* [162] and perfected by Ramanathan *et al* [157] and has the distinct advantage of working for almost any optical depth. A small given percentage of atoms are outcoupled and imaged, leaving the original condensate almost unaltered. Using PTAI, the condensate can be imaged up to 50 times before breakdown [157]; The PTAI method was used successfully to visualise solitonic vortices [163] and reconnecting vortex lines [101, 164] in cigar shaped condensates. PTAI can be particularly useful for studying the evolving dynamics of moving solitons within a condensate. Shining light upon the outcoupled cloud and projecting this onto a charge-coupled device camera, experimentalists can thus gain multiple column integrated density profiles of the system [165, 166].

We will employ the success of the PTAI method to show that, by taking multiple snapshots of a condensate, there is a link between the averaged density spectra and the dark solitons present. In this chapter, we solve the Gross-Pitaevskii equation for a harmonically trapped 1D system with dark solitons present. We will study condensates with single and multiple solitons and introduce the idea of a spectral shift to identify the depth of any soliton present. We utilise the density engineering method in order to study more experimentally valid systems and finally, will discuss the implications for 3D condensates.

4.1.1 Model

In the zero temperature limit, the mean field approximation for the wavefunction $\psi(x, y, z, t)$ of a condensate provides a quantitative model of the dynamics in the form of the Gross-Pitaevskii equation (GPE) (Eq. 2.45). We can reduce Eq. (2.45) [167] by taking the perpendicular trapping frequencies to be sufficiently

large, $\omega_\perp \gg \omega_x$, and integrate out the dependence on y, z. We present the results in this chapter using the natural units for a homogeneous condensate, as outlined in section 2.3, so that the 1D GPE used is defined as

$$i\frac{\partial \psi}{\partial t} = -\frac{1}{2}\frac{\partial^2 \psi}{\partial x^2} + \frac{1}{2}\omega^2 x^2 \psi + |\psi|^2 \psi - \psi \qquad (4.1)$$

All results presented are for $\omega = 0.02$, which ensures we are within the Thomas-Fermi limit $R_x \gg \omega^{(-1/2)}$, where R_x denotes the Thomas-Fermi radius. Provided this relation is satisfied, we can model the shape of the 1D condensate by the Thomas-Fermi profile [168, 169]; for $\omega = 0.02$, $R_x \approx 70$. As discussed above, phase defects in a repulsive 1D condensate take the form of dark solitons. The analytic expression for a dark soliton of prescribed speed v in a homogeneous background is [21],

$$\Psi_S(x, t) = \sqrt{n}\Big[B \tanh\big\{B(x - x_0(t))\big\} + iv\Big], \qquad (4.2)$$

where $B = \sqrt{1 - v^2}$, and $v = v/\sqrt{n}$. The parameter $x_0(t)$ defines the location of the soliton at time t, where $x_0(t) = vt + b$, where b is an arbitrary constant denoting the initial location of the soliton. To set up the initial condition for a numerical simulation of a single soliton in our condensate we multiply Ψ_s by the ground state Ψ of a harmonically trapped condensate. The density depletion at the minimum of the resulting condensate and the speed of the soliton are related via,

$$\Delta n = 1 - v^2. \qquad (4.3)$$

For clarity, hereafter primes are dropped throughout. In the numerical simulations the GPE is solved via a fourth-order Runge-Kutta method using `MATLAB` with $dx = 0.1$ and $dt = 0.01$. At desired times, we compute the density spectrum, defined as the Fourier transform of the density of the condensate, $\tilde{n}(k) = \mathcal{F}(n(x)) = |\mathcal{F}(|\Psi(x)|^2)|$, using inbuilt `MATLAB` subroutines for the Fast Fourier Transform, where k is the wavenumber $k = 2\pi/x$.

4.1.2   Ground state

We begin our investigation by first studying the density spectrum of the ground state of a 1D harmonically trapped condensate. Figure 4.1 compares the density spectrum of a ground state solution, obtained numerically, to the density spectrum of its Thomas-Fermi approximation. The two spectra are consistent in the region of k-space corresponding to the central region within the Thomas-Fermi width, R_x, and the order of a few healing lengths, 5ξ (the scale of the edges of the condensate), but they deviate at large wavenumbers.

4.1.3   Single Soliton

As discussed earlier, a condensate containing a single soliton is easily obtained by multiplying the ground state wavefunction by the expression for a dark soliton, Eq. (4.2), in a homogeneous system (see Fig. 4.2(a)). Upon comparing the spectrum of the ground state and the spectrum of the single-soliton condensate, we notice a shift rightwards towards the smaller length scale (larger k) region. We quantify
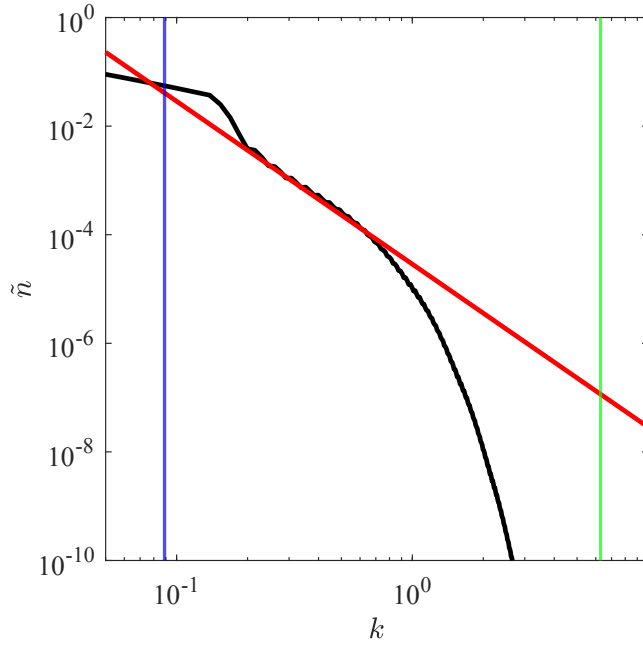
FIGURE 4.1: The density spectra $\tilde{n}$ of the ground state (black) and of its Thomas-Fermi approximation, (red), vs wavenumber k; the wavenumbers corresponding to the healing length (green) and the Thomas-Fermi radius (blue) are marked as vertical lines.

this spectral shift and relate it to the soliton's depth Δn (hence its speed v), and proceed in the following way. Consider a single soliton at the condensate centre. As
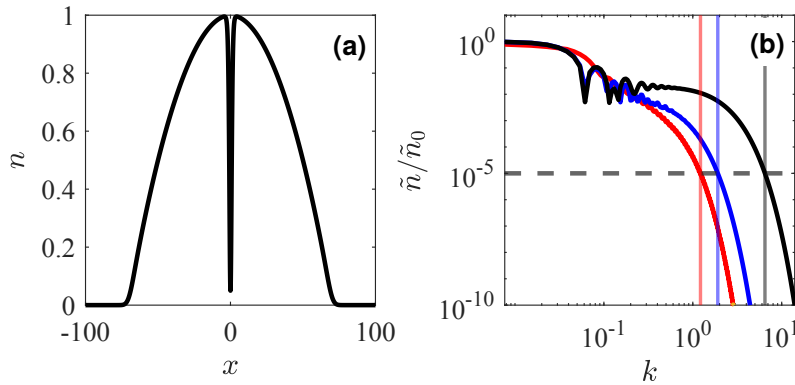
FIGURE 4.2: (a) The density of a condensate with a soliton with a depth $\Delta n = 0.9$ inserted at the centre; (b) the scaled spectra $\tilde{n}/\tilde{n}_0$ of a ground state condensate (red) and of a condensate containing a soliton of depth $\Delta n = 0.1$ (blue) and a soliton of depth $\Delta n = 0.9$ (black), with n_i marked by horizontal black line. The corresponding intercept wavenumber k_is are also marked by vertical dashed lines.

mentioned earlier, a single soliton in a harmonically trapped condensate oscillates around the trap's minimum at frequency $\omega/\sqrt{2}$ with an amplitude depending on the soliton depth Δn. We let the system evolve in time for $t = 500$, averaging density spectra taken for every 0.5 time units. The total time of the simulation equates to a few oscillations of the soliton on the trap, a timescale achievable in experiments (using the trapping parameters of the experiment of Weller *et al.* [124], this corresponds to a timescale of 20-30ms). We verify that the the resulting time-averaged spectrum does not change in time, and also verify that the location of the soliton at a given t does not affect the measurement. Figure 4.2(b) shows that the addition of a soliton drastically shifts the density spectrum to larger wavenumbers (compare the blue curve with the red and yellow curves). For the sake of making comparisons, the density spectra $\tilde{n}(k)$ we present are rescaled by $\tilde{n}_0$, defined as $\tilde{n}$ for $k \to 0$. To quantify the shift of density spectrum to larger wavenumbers arising from the presence of solitons, we define the relative spectral shift $\Delta k_i = k_i/k_i^{(0)}$; here k_i, which we refer to as the intercept wavenumber, is the wavenumber corresponding to the value $\tilde{n}_i = 10^{-5}\tilde{n}_0$ in the presence of the soliton, and $k_i^{(0)}$ is the intercept wavenumber of the ground state. For the ground state with $\omega = 0.02$, $k_i^{(0)} = 1.22$. Comparing Δk_i obtained for a variety of soliton depths from 0.1 to 0.9 we observe the following power law relation between soliton depth and relative spectral shift of the density,

$$\Delta k_i \sim \Delta n^\alpha, \tag{4.4}$$

with $\alpha = 0.55$ (see Fig. 4.3). Clearly, the deeper the soliton the larger the spectral shift. We have verified that this result does not depend on the precise definition of n_i; all evaluated measurements of n_i give a result for α of 0.55 ± 0.05. We have also checked that Eq. 4.4 is valid for a variety of harmonically trapped condensates, as long as these condensates are deeply in the Thomas-Fermi regime. Rescaling n_0 from 1, and hence altering the norm of the system, we have verified that the norm of the condensate does not affect the spectral shift. If we look at systems with $\omega \neq 0.02$, we find that for $\omega \ll 1$, the same relation (albeit with a different power law) is present. When $\omega \to 1$, we see that it begins to falter; the condensate itself begins to have structure on the same lengthscales as the dark solitons.

4.1.4 Two solitons

The strong dependence of the spectral shift on the depth of a single soliton moving within the condensate enables us to determine the depth, and hence speed, of the soliton existing in the system. The next logical step is to assess how multiple solitons affect the density spectrum, whether a spectral shift is still observable, and finally whether it can be related to the number or the depths of the solitons.

For two solitons of equal depth, the power law relationship between the soliton's depth and the relative spectral shift (Eq. (4.4)) holds true. The combination of two solitons of two different speeds, as presented in fig. 4.4(a), exhibits a more complicated spectral signature. Figure 4.4(b) shows results for two solitons. We immediately see that Δk_i depends mainly on the deepest soliton (the shallower soliton having only a minor effect). Although direct determination of the depths
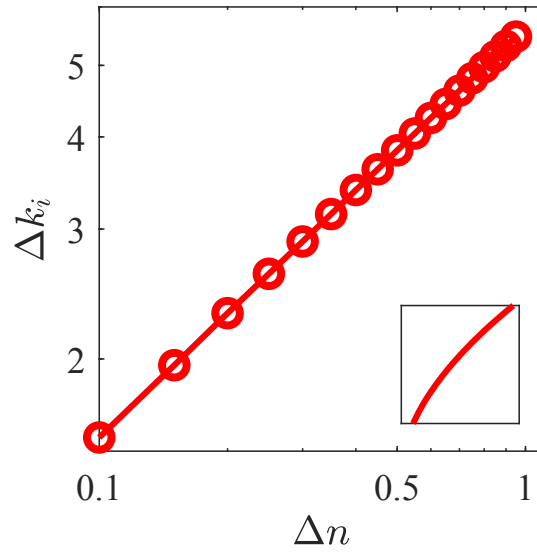
FIGURE 4.3: The spectral shift Δk_i for different soliton depths Δn on a logarithmic scale (main Figure) and linear scale (inset; same ranges as the main Figure).
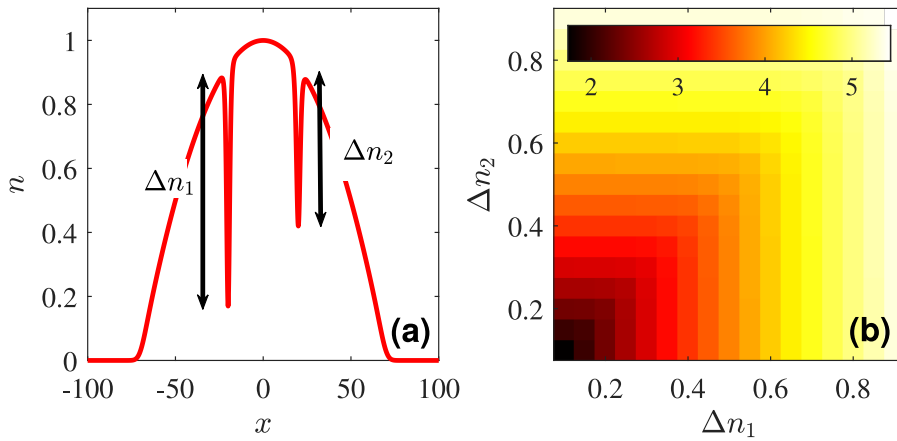
FIGURE 4.4: (a) The density profile, $n(x)$, of condensate with two solitons with depths $\Delta n_1 = 0.75$ and $\Delta n_2 = 0.5$ respectively; (b) the spectral shift Δk_i (values on the colorbar) obtained for a range of values of Δn_1 and Δn_2.

(and hence speed) is not possible from the spectra, the concentric nature of the results presented in Fig. 4.4(b) shows that if we know the shift, we can easily narrow down the depths to a range of results.

4.1.5 Many solitons

We have established that in a two-soliton system the spectral shift is mostly affected by the deepest soliton. However, the methods of creating solitons, as discussed in the introduction, can often lead to a train of solitons. To make better contact with

experiments, in this section we describe the spectral shift caused by a relatively large number, N, of solitons. We choose $N = 9$, with the first soliton of depth Δn_1 and the other eight of the same depth Δn_{N-1}, as shown by Fig. 4.5(a). Figure 4.5
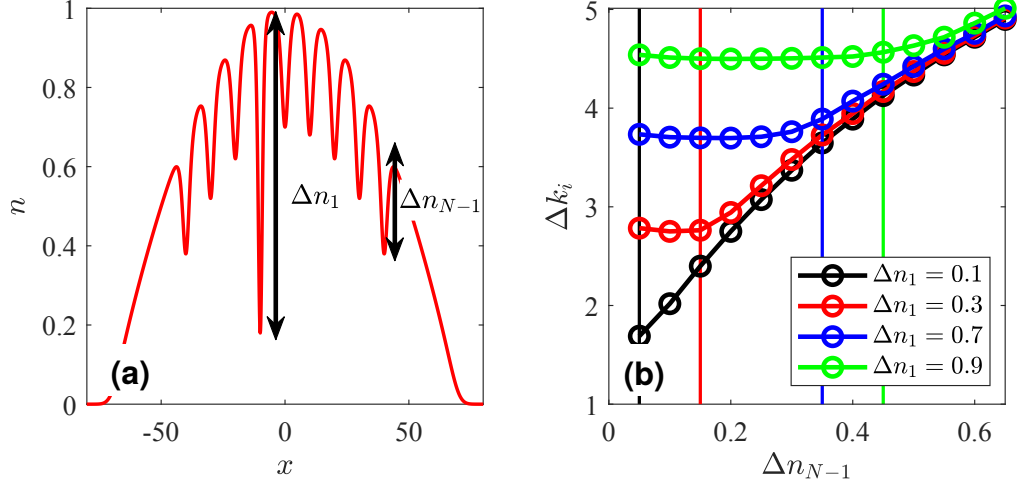
FIGURE 4.5: (a) Density of a condensate with $N = 9$ solitons: one soliton has depth $\Delta n_1 = 0.7$ and the other eight solitons have depth $\Delta n_{N-1} = 0.3$, (b) the resulting spectral shift Δk_i as a function of Δn_{N-1} for varying Δn_1, with $\Delta n_1/2$ marked with vertical lines in their corresponding colours.

further supports the previous finding that the deepest soliton contributes the most to the shift of spectrum, hence a higher value of Δk_i. The spectral shifts shown in the figure display the same dependence on solitons' depth displayed in Fig. 4.4: that is Δk_i only begins to change when Δn_{N-1} is comparable to Δn_1. More precisely, Δk_i is noticeably affected only when Δn_{N-1} is roughly half the value of Δn_1 (marked with vertical lines in Fig. 4.5(b)).

4.1.6   Effects of perturbations

All results described in the previous sections refer to solitons imprinted into the ground state. In many experiments, because of the method used to generate them, solitons coexist with sound waves. The following density engineering method allows us to mimic this more realistic situation numerically. We apply a Gaussian potential of width σ and amplitude A for a time $\mathcal{T}$ in the centre of the trap, before instantaneously removing it. This overall potential has the form

$$V(x,t) = \begin{cases} \frac{1}{2}\omega^2 x^2 + A\exp\left(-x^2/\sigma^2\right) & \text{for } t \leq \mathcal{T} \\ \frac{1}{2}\omega^2 x^2 & \text{for } t > \mathcal{T} \end{cases}. \tag{4.5}$$

This mimics the creation of solitons via density engineering methods and causes a density dip to form at the centre of the condensate. When removed, both solitons and sound waves are generated during the collapse inwards of the two sides, as shown in Fig. 4.6(a). We measure the depth of the two main solitons created in order to imprint them into a ground state for comparison (Fig. 4.6(b)). We choose $\sigma = 2$, $\mathcal{T} = 5$ and vary the amplitude, A, of the central Gaussian pulse. The larger
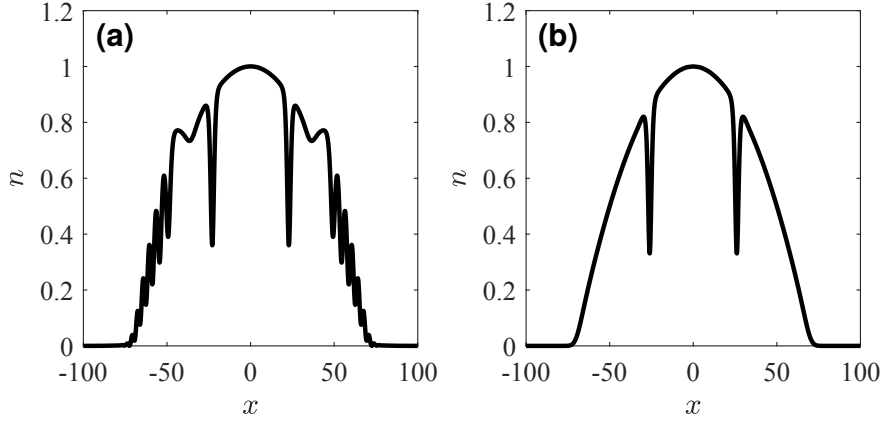
FIGURE 4.6: (a) The density of a condensate after being excited by a pulsed Gaussian potential with $A = 1$; note the creation of two main deep solitons (here with $\Delta n \approx 0.53$) together with sound waves. For comparison, (b) shows two solitons of the same depth $\Delta n = 0.53$ imprinted into a ground state.

the amplitude A, the deeper the leading solitons created (see Fig. 4.7(a)). In Fig. 4.7(b), we compare the relative spectral shifts Δk_i resulting from solitons which are imprinted in the ground state (red line) and density engineered (blue line). We see immediately that although the spectral shifts Δk_i in the two systems are not equal, the relationship between the soliton depths and the intercept wavenumbers still holds, regardless of the presence of sound waves. When $A \to 0$, no solitons are cre-
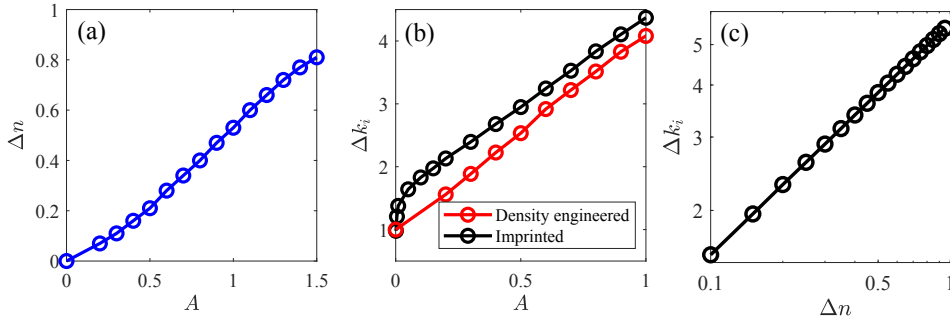
FIGURE 4.7: (a) The depth Δn of the leading solitons created by a Gaussian pulse with amplitude A; (b) comparison between the spectral shifts Δk_i arising from two solitons in the presence of sound waves (black) and two solitons of the same depth imprinted in the ground state (red) and (c) the repeated results from Fig. 4.3 for direct comparison with the Gaussian results in (b).

ated. Notice the rapid change of the spectral shift for very small amplitudes A (Fig. 4.7(b)); these small spectral shifts correspond to systems with no detectable soliton. The relation between the amplitude and the intercept wavenumber k_i begins to level off at roughly at $A = 0.2$, corresponding to two solitons of depth $\Delta n = 0.07$.

We conclude that sound waves can shift the density spectrum, but the shift is small compared by the larger shift induced by solitons.

4.1.7   Conclusion

We have presented a method for accurately ascertaining the depth (and hence the speed) of a single soliton in a harmonically trapped condensate from the density spectrum alone. We have also shown that, in a system with multiple dark solitons, the spectral shift is mainly determined by the deepest soliton.

The analysis of the spectral shift which we have presented here for 1D systems may potentially be applied to 3D turbulent systems. A spectral shift of the momentum of the condensate has indeed already been reported in an experiment with a turbulent 3D condensate [8]. While 1D phase defects are solitons whose width depends on its speed, the phase defects present in 3D system are vortices. Since multiply charged vortices are unstable in most cases, the width of the vortex cores is constant (although, in a harmonically trapped condensate, this width increases near the edge). Therefore it may be possible to relate the measured spectral shift to the number or the length of vortices present in the system, thus providing a quantitative measure of the intensity of the turbulence in the condensate.

5 The expansion of simple Three-Dimensional condensates

The expansion of a condensate is used ubiquitously in experimental studies of BECs. Here, an experimentalist is able to estimate the temperature of the system, and thus if they have obtained a large enough condensate fraction. As the condensate expands rapidly out, the density falls and one is, hence, able to pass light through the condensate in order to image any feature within the condensate. If a spherically shaped condensate expands out, it simply grows larger. If a harmonically trapped condensate with uneven trapping expands, however, the condensate will invert (see Fig. 5.1). It has been reported [11, 170] that when a turbulence con-
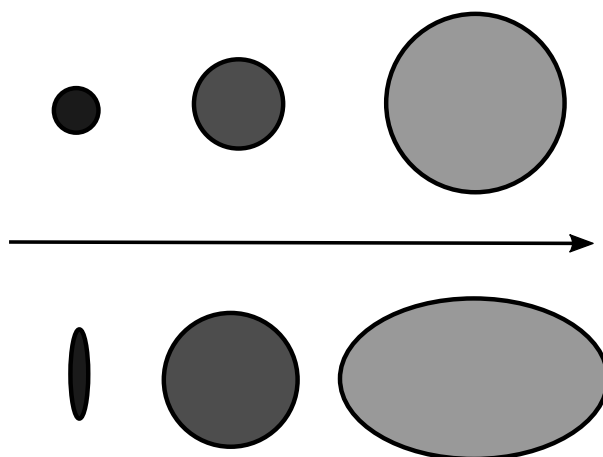
FIGURE 5.1: The expansion of (a) a spherical cloud and (b) and cigar condensates.

densate expands, the inversion is not observable and one sees what is referred to as a "self-similar" expansion. It has been predicted that this is due to the vortices within a condensate. We therefore study here how phase-defects effect a condensate and look at what analytical studies best model our computational results. We also look at a couple of smaller problems, such as how the reconnection of vortices is affected by expansion; it is often assumed that as soon as a condensate is released, the interactions and motions within the condensate bulk freezes. We also verify that the expansion is effected not by a generic addition of energy (modelled here as large density fluctuations) but the vortices themselves that cause this diversion of expansion scalings.

5.1 Review of Time-of-Flight

Akin to the 1D case outlined previously, a set of equations can be derived using the Thomas-Fermi radii and a scaling parameter b to give a approximated form of the change of the Thomas-Fermi radii for an expanding condensate. This results in a coupled ODE of the scaling factors b_r and b_z, Reminding ourselves of the 3D Gross-Pitaevskii equation,

$$i\hbar\frac{\partial\psi}{\partial t} = -\frac{\hbar^2}{2m}\nabla^2\psi + g|\psi|^2\psi + V\psi - \mu\psi, \tag{5.1}$$

with a harmonic trapping potential of

$$V = \frac{1}{2}m\omega^2 r^2. \tag{5.2}$$

Assuming that the condensate does not change in time and the condensate is large, the GPE can change to

$$\mu\psi = gn\psi + V\psi. \tag{5.3}$$

For a harmonically trapped condensate, we can therefore express the Thomas-Fermi profile of the condensate as

$$n = \begin{cases} n_0\left(1 - \frac{r^2}{R^2}\right) \\ 0 \end{cases} \tag{5.4}$$

where the peak density $n_0 = \mu/g$ and the Thomas-Fermi width $R = \sqrt{2\mu/m\omega^2}$. The wavefunction of the condensate can be expressed as a Madelung transform, where

$$\Psi(\mathrm{x}, t) = \sqrt{n(\mathrm{x}, t)}\exp\left(iS(\mathrm{x}, t)\right) \tag{5.5}$$

where n, as usual, is the density of the condensate and S denotes the phase. The fluid velocity is defined as,

$$\mathbf{v}(\mathrm{x}, t) = \frac{\hbar}{m}\nabla S(\mathrm{x}, t). \tag{5.6}$$

One can insert Eq. (5.5) into the GPE, and separate the real and imaginary parts to gain two hydrodynamical equations. First, the continuity equation

$$\frac{\partial n}{\partial t} + \nabla\cdot(n\mathbf{v}) = 0, \tag{5.7}$$

which dictates the conservation of atoms and

$$m\frac{\partial\mathbf{v}}{\partial t} + \nabla\left(\frac{mv^2}{2} + ng + V - \frac{\hbar^2}{2m}\frac{\nabla^2\sqrt{n}}{\sqrt{n}}\right) = v\times(\nabla\times v). \tag{5.8}$$

The

$$\frac{\nabla^2\sqrt{n}}{\sqrt{n}} \tag{5.9}$$

term denotes the quantum pressure and can, for now, be ignored but will become important later. The right hand term of the second hydrodynamical equation can be neglected for the ground state we consider here. When assuming $\partial \psi / \partial t = 0$ in Eq. (5.8), one can recover the Thomas-Fermi profile from Eq. (5.4). We can use the above devices to work out scaling solutions. Assuming a static, large, harmonic condensate, Eq. (5.8) becomes

$$\nabla \left(\frac{1}{2} m (\omega_x^2 x^2 + \omega_y^2 y^2 + \omega_z^2 z^2) + gn \right) = 0. \tag{5.10}$$

Rearranging, for $n > 0$,

$$n = \frac{2\mu - m(\omega_x^2 x^2 + \omega_y^2 y^2 + \omega_z^2 z^2)}{2g}. \tag{5.11}$$

For a condensate of N atoms, the peak density of the condensate is given as

$$n_0 = \frac{15N}{8\pi R_x R_y R_z}. \tag{5.12}$$

If we now consider a change in the trapping potential $\omega \to \omega(t)$, we can assume that the Thomas-Fermi widths change in time, $R \to R(t) \to b(t)R(t = 0)$ so that the profile in time is

$$n(x, y, z, t) = \frac{n_0}{b_x b_y b_z} \left(1 - \frac{x^2}{b_x^2 R_x^2} - \frac{y^2}{b_y^2 R_y^2} - \frac{z^2}{b_z^2 R_z^2} \right). \tag{5.13}$$

We know that at $t = 0$, $b(t = 0) = 1$ and $\partial b(t = 0)/\partial t = 0$. The velocity of the system must satisfy the continuity equation and is therefore of the form,

$$\mathbf{v}(\mathbf{x}, t) = \frac{1}{2} (\alpha_x(t) x^2 + \alpha_y(t) y^2 + \alpha_z(t) z^2) \tag{5.14}$$

where $\alpha_i(t) = b_i(t)/\dot{b}_i(t)$. If one has a system where the trapping potential has changed in time, one can define the trapping as the initial trapping potential ω_i and one changing in time $\omega_i(t)$. One therefore ends up at

$$\frac{\partial^2 b_i}{\partial t^2} + \omega_i^2(t) b_i - \frac{\omega_i^2}{b_i b_x b_y b_z} = 0. \tag{5.15}$$

where $i = (x, y, z)$. For a condensate with $x = y = r$, the scaling solutions are therefore

$$\frac{\partial^2 b_r}{\partial t^2} + \omega_r(t)^2 b_r - \frac{\omega_r^2}{b_r^3 b_z} = 0, \tag{5.16}$$

and

$$\frac{\partial^2 b_z}{\partial t^2} + \omega_z(t)^2 b_r - \frac{\omega_z^2}{b_r^2 b_z^2} = 0. \tag{5.17}$$

Equations (5.16) and (5.17) can be used to model various modes such as the monopole mode and the quadropole mode of the condensate. If we, instead of changing the

trap, switch the trap off at $t = 0$, we can negate the trap in time in Eq. (5.16) and (5.17), so that

$$\frac{\partial^2 b_r}{\partial t^2} - \frac{\omega_r^2}{b_r^3 b_z} = 0, \tag{5.18}$$

and

$$\frac{\partial^2 b_z}{\partial t^2} - \frac{\omega_z^2}{b_r^2 b_z^2} = 0. \tag{5.19}$$

For the rest of this chapter onwards, we will express our results in natural units. These coupled ordinary differential equations can be simply solved in MATLAB using an `ode45` solver; `ode45` is an off-the-shelf technique solving differential equations using the Runge-Kutta technique. This results of which are shown in Fig. 5.2. On the left is an ordinary spherical condensate with $\omega_{r,z} = 0.08$. On the right is a cigar condensate with $\omega_{r,z} = [0.08, 0.02]$. Both have similarities; in the small time
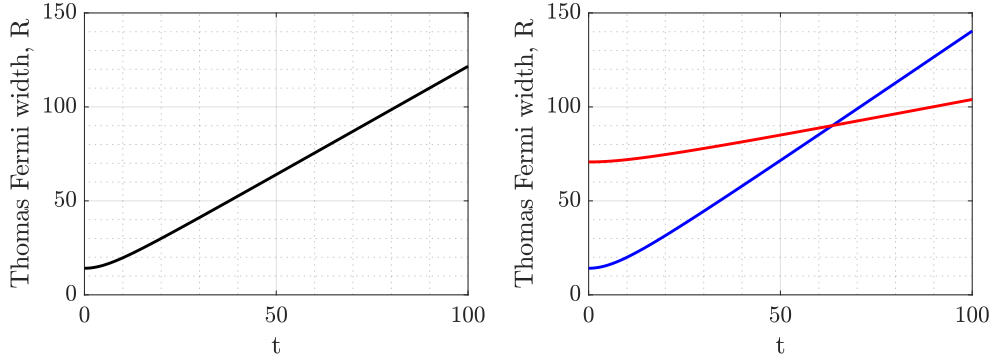
FIGURE 5.2: The ODE prediction for the change in the Thomas-Fermi width, $R_{x,y,z} \equiv R_r$, of an expanding spherical condensate (left) and the R_r (blue) and R_z (red) of an expanding cigar condensate (right), highlighting the aspect ratio inversion at $t \sim 60$.

there is an acceleration outwards, followed by a linear regime. In the cigar case, the tightly bound radial direction rapidly expands out compared to the axial and, at a time $1/\omega_z$, the shape of the condensate inverts. This signature inversion has historically been used to identify to experimentalists whether they have achieved condensation. We can recall the total energy of the condensate

$$E = \int d^3\mathbf{x} \left[\frac{1}{2} |\nabla \psi(\mathbf{x}, t)|^2 + V |\psi(\mathbf{x}, t)|^2 + \frac{1}{2} |\psi(\mathbf{x}, t)|^4 \right], \tag{5.20}$$

and can use this to model the energies of an expanding Thomas-Fermi profile. The three terms in the integral are the kinetic, interaction and potential energies of the system respectively. We see in Fig. 5.3 at the change in the scaling parameter b in respect of time and the growth of the kinetic energy (from the rapid expansion of the condensate) has almost exactly the same profile. As the interaction energy becomes negligible, the condensate then expands linearly. A computational simulation of an expanding ground condensate using our computational techniques is given in Fig. 5.4.
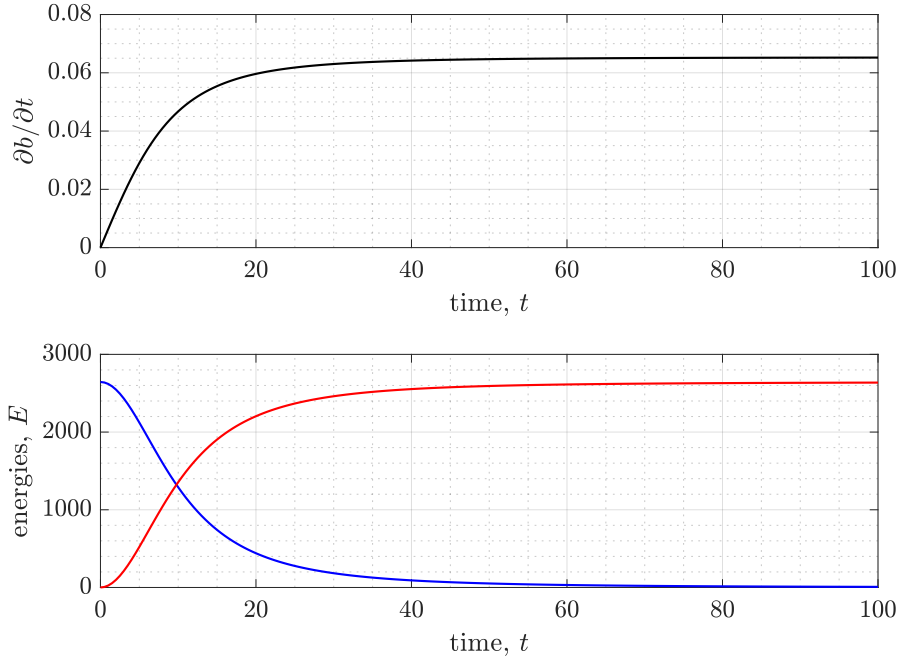
FIGURE 5.3: The (top) change in the scaling factor in time $\partial b/\partial t$ for a spherical expanding condensate and the (bottom) interaction energy (blue) and kinetic energy (red) of an expanding spherical Thomas-Fermi profile.

5.2 Expanding ground states and quantification of width

The derivation of Eqs. (5.16) and (5.17) assumes a Thomas-Fermi profile with a scaling parameter $b_{(r,z)}$. We see, however, that in our turbulent work (see later in this thesis, e.g. Fig. 6.4) that such a quantification cannot be assumed. We also know that experimentalists do not have access to quantifying a Thomas-Fermi profile from an integrated TOF image. Through discussions with the Sao Paulo group, we know that experimentalists quantify the width by simply looking at the width in which the density falls down to a certain percentage of the measured peak density. We first compare the expansion the ground state of a spherical and cigar condensate with our remeshing computational grid. The spherical condensate has a trapping potential of $\omega = 0.06$ corresponding to a Thomas-Fermi radius of $R = 23.5$ while our cigar condensate here is defined by the trapping potentials $\omega_{(r,z)} = [0.08, 0.02]$ with the corresponding Thomas Fermi radii of $R_{r,z} = [17.6, 70.7]$. Fitting is acheived using a least squared fitting of of the Thomas-Fermi profile. We see in Fig. 5.5 that none of the percentages totally recover the Thomas-Fermi radii of the system. Even so, the aspect ratio of the condensate is almost exactly replicates the fitted Thomas-Fermi result for a width quantified by the location corresponding to 10% of the peak density given in the integrated density.
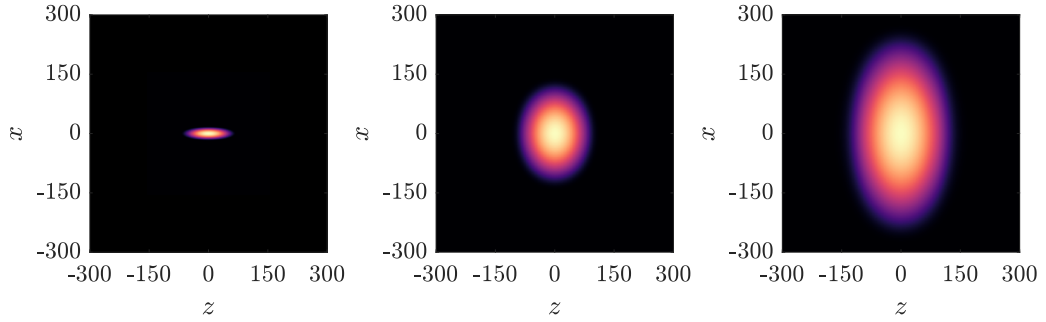
FIGURE 5.4: The expansion of a ground state cigar condensate at (a) $t = 0$, (b) $t = 100$ and (c) $t = 200$.
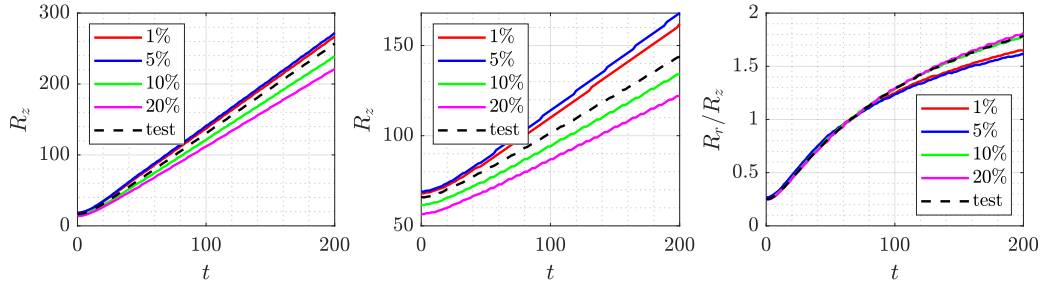
FIGURE 5.5: The widths of the condensate quantified from a measurement of the width given by a given percentage of the peak density from the integrated density compared with the fitted Thomas-Fermi radii for a cigar condensate expanding in time in the (a) radial and (b) axial directions and the (c) aspect ratio for different percentages in coloured solid lines and the aspect ratio given from the measured Thomas-Fermi radii in black dashed lines.

5.3 Expansion of arbitrary vortex states

In order to quantify the mechanism behind self-similar expansion of condensates originally trapped in an anisotropic trap, we do not jump straight into looking at how turbulent systems expand but how states with arbitrary vortices expand and the effect of interior structure changes the nature of expansion. Although for a system with large numbers of vortices, this setup is specifically for when all vortices have the same sign so the system has a net rotation. When considering a random collection of vortices, although each vortex will have its own velocity field associated with it, it can be assumed that the overall macroscopic velocity of the condensate will be negligible. Once again negating the term associated with quantum pressure, Eq. (5.8) can therefore be expressed as

$$m\frac{\partial \mathbf{v}}{\partial t} + \nabla\left(\frac{1}{2}mv^2 + gn + V\right) = 0. \tag{5.21}$$

The $mv^2/2$ term can be equated to a turbulent kinetic term, which for now we label as αn. Taking for now the steady states solution, Eq. (5.21) can therefore be expressed as

$$\nabla(V + [\alpha + g]n) = 0. \tag{5.22}$$

This effectively rescales the interaction term so that

$$\hat{g} = g + \alpha = g\left(1 + \frac{\alpha}{g}\right), \tag{5.23}$$

assuming that $\alpha \ll g$. This method does not give the intended result and instead simply rescales the effective interaction parameter, $g \rightarrow \hat{g}$. If one follows through with a derivation of the coupled ODEs, one will find that the adding of the extra energy term α simply changes the initial condition of the Thomas-Fermi profile and gives a result for a ground state with a different initial Thomas-Fermi width,

$$\hat{R} = R\left(1 + \frac{1}{5}\frac{\alpha}{g}\right), \tag{5.24}$$

and peak density

$$\hat{n}_0 = n_0\left(1 - \frac{3}{5}\frac{\alpha}{g}\right). \tag{5.25}$$

We can have a spherical system with a number of vortices N and see how the vortices affect the Thomas-Fermi radii of the system, Eq. (5.24), to see how strong an effect they have on the system. The total vortex line length is obtained from our vortex detection method discussed in Section 3.2. Looking at Fig. 5.6 we see that compared to the total vortex line length of the system, the effect is small; a standard fitting procedure shows that if we find a value of α based on the vortex line length of the system, $\alpha \rightarrow \beta L$, then we find $\beta = 0.00359$, i.e., that it is an exceptionally small scaling. Here, we note a later result by Caracanhas et al. [171], where a condensate is filled with a vortex tangle with no direction of associated vorticity. From this, they derived coupled ODEs, where the Thomas-Fermi radius of the turbulent expanding condensate changes in time as

$$
\begin{aligned}
\frac{\partial^2 R_j}{\partial t^2} =& 14\pi \frac{\hbar^2}{m^2} \frac{\mathcal{L}(R_{x0}^2 + R_{y0}^2 + R_{z0}^2)R_j(t)}{(R_x(t)^2 + R_y(t)^2 + R_z(t)^2)^2} \ln\left(\frac{\ell}{\xi}\right) \\
&+ \frac{15\hbar^2 a_s}{m^2} \frac{N}{R_j(t)R_x(t)R_y(t)R_z(t)}
\end{aligned}
\tag{5.26}
$$

where $j = (x, y, z)$, $\mathcal{L}$ denotes the initial total vortex line density and ℓ denotes the average inter-vortex spacing, $\ell \approx \mathcal{L}^{-1/2}$.

5.4 Analytical approximations of vortices

We begin by looking at the affect of vortices on the energy of the background condensate. As stated previously, a vortex can either be a line, where it terminates at
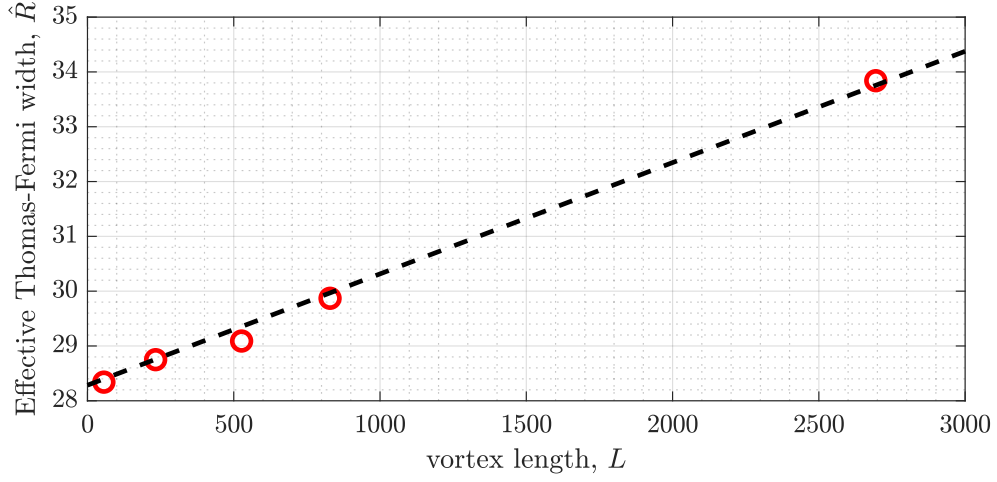
FIGURE 5.6: The rescaled Thomas-Fermi radii, $\hat{R}$, as a function of the total vortex line length in the system, L for the five condensates we study the expansion of later.

edges of a condensate, or it can be a vortex ring, where it terminates on itself. We first look at how the incompressible energy of the vortices scales with both the size and topology of the vortex. The incompressible kinetic energy per unit length of a line vortex in a condensate can be approximated and ends up as directly proportional to the length of the vortex,

$$E = \frac{\Gamma^2}{2\pi} n \ln\left(\frac{\ell}{\bar{\xi}}\right), \tag{5.27}$$

where Γ is the phase winding 2π and ℓ here denotes the average inter-vortex length $\ell = 1/\sqrt{L/\mathcal{V}}$. The parameter, $\mathcal{V}$, refers to the volume of the condensate. For a spherical harmonically trapped condensate, the volume can be calculated from the standard volume of a sphere using a Thomas-Fermi radii. The kinetic energy of a vortex ring per unit length [172, 173], however, can be expressed as

$$E = \frac{n}{2}\Gamma^2 \left[\ln\left(\frac{8r}{a}\right) - 2 \right], \tag{5.28}$$

where r is the radius of the ring, often with the stipulation $r > a$. We compare this result with the energy calculated from computational means. We assess a spherically trapped condensate with $\omega = 0.02$ and study both systems of lines and rings. The above approximations make the assumption that the background density is homogeneous; not the case for a harmonically trapped condensate. We therefore first briefly see how the randomisation of vortices affects this approximation. We then add in either randomised vortex lines with an arbitrary orientation, or vortices of a given radius r and present these results in Fig. 5.7. Comparing the computationally calculated incompressible energy to the estimation gives an almost exact result for the straight line vortices and rings or large radii. The system with the

smallest radius ($r = 5\xi$) vastly overestimates the energy, however for all simulations presented, the incompressible energy is proportional to the total length of the system. It is worth pointing out in the straight line plots, that the first point is off by a lot; this is simply because the randomized single vortex is by chance right on the edge of the condensate, and therefore the approximation fails. We now move
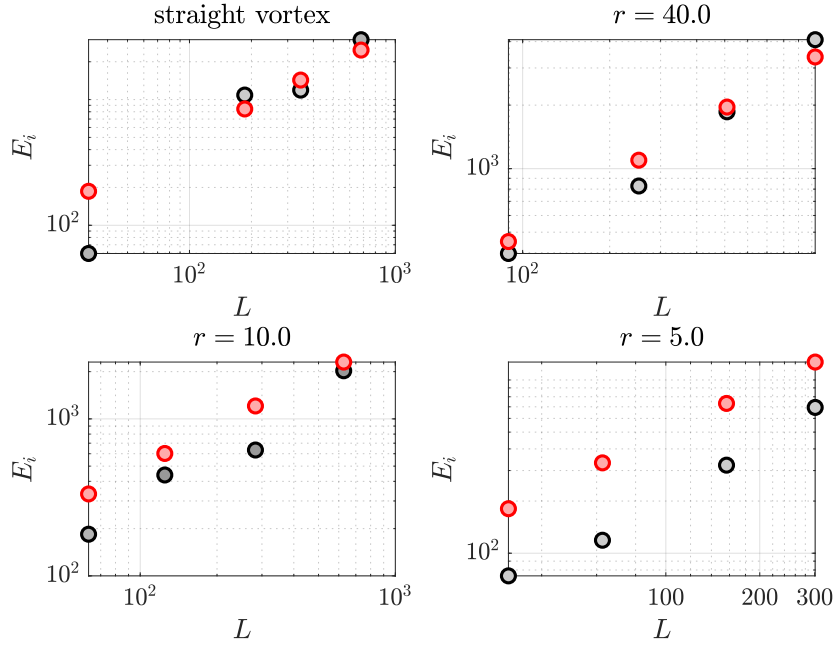
FIGURE 5.7: The comparison of the calculated incompressible energy (black) and the straight line analytical result from Eq. (5.27) for the incompressible energy for a condensate of straight vortices (top-left) ring vortices a denoted radii.

on to looking at the approximation in Eq. (5.29) and how it works for our ring setup. Due to the inhomogeneous background of the condensate, some rings are far enough towards the edges of the condensate to become "arc"-vortices and the overall incompressible energy is therefore calculated to be

$$E = \sum_{i=1}^{N} \frac{L_i}{C} \frac{n}{2} \Gamma^2 \left[\ln \left(\frac{8r}{a} \right) - 2 \right], \tag{5.29}$$

where L_i is the length of the individual vortex and C simply corresponds to the the circumference of a circle, hereby considering that some of the randomized vortices will be arc-vortices. We find smaller vortices, that the ring approximation works better than the line approximation. For larger rings, however, the reverse is true. To summarise, we find that both approximations work reasonably well for vortex rings, when the ring is relatively large. For systems will small numbers of vortex rings, the ring approximation becomes more precise. Both approximations fail for when $r \to a$. This is to be expected.
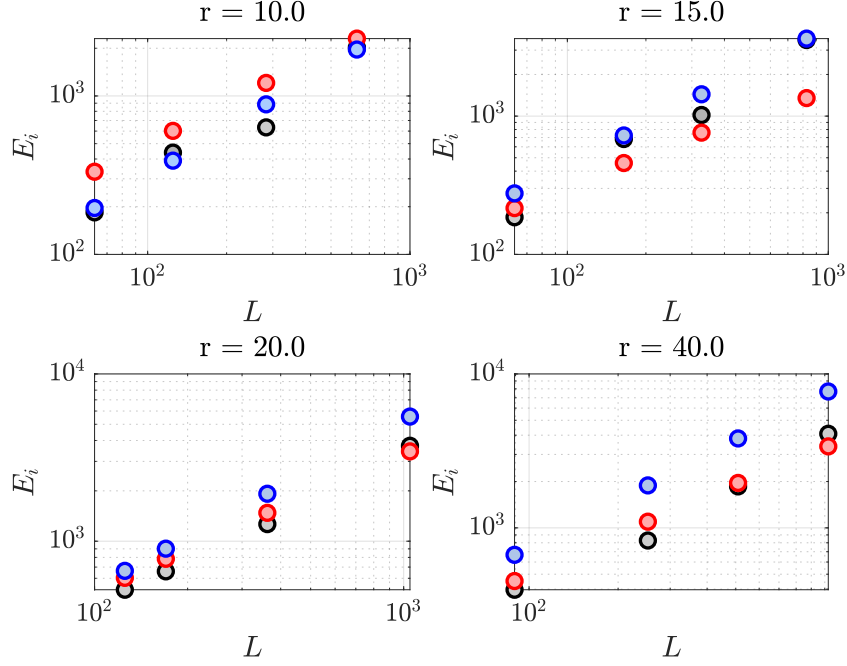
FIGURE 5.8: The comparison of the calculated incompressible energy (black), the vortex line approximation (red) (Eq. (5.27)) and the vortex ring approximation (blue) (Eq. (5.29)).

5.5 Expansion of arbitrary vortex states

Now we have analytical predictions for both the energy of vortices in a system and a predicted ODE as a function of the vortex line density. We revisit the result originally derived by Caracanhas *et al.* [171]. In our dimensionless formulation, this can be shown to be

$$
\frac{\partial^2 R_j}{\partial t^2} = \frac{14 \mathcal{L} R_j(t)(R_{x0}^2 + R_{y0}^2 + R_{z0}^2)}{[R_x^2(t) + R_y^2(t) + R_z^2(t)]^2} \ln(\ell)
$$
$$
+ \frac{2 R_{x0} R_{y0} R_{z0}}{R_x(t) R_y(t) R_z(t) R_j(t)}. \tag{5.30}
$$

where $j = (x, y, z)$. To see how this works, we begin by studying the expansion of a spherical condensate before then moving to a cigar condensate to determine whether vortices can cause a self-similar expansion.

5.5.1 Expansion of spherical condensates

We expand the condensates which were plotted in Fig. 5.6. This Figure plots the result as a function of the total vortex line length; in terms of number of vortices, these results are for $N = 1, 5, 10, 20$ and 50 vortices; the vortices are orientated in random orientations with a randomised circulation of either -1 or 1 with a random location given between $x \in [-0.75 R_r \; 0.75 R_r]$ (see Fig. 5.9). We expand these condensates

for $t = 150$ and do a fitting to a Thomas-Fermi profile to quantify the width to monitor the expansion in time. We compare these results to both the ground state expansion ODE (Eqs. (5.18) and (5.19)) with a re-scaled effective Thomas-Fermi radii and the predicted expansion dependant on the vortex density, Eq. (5.30). To
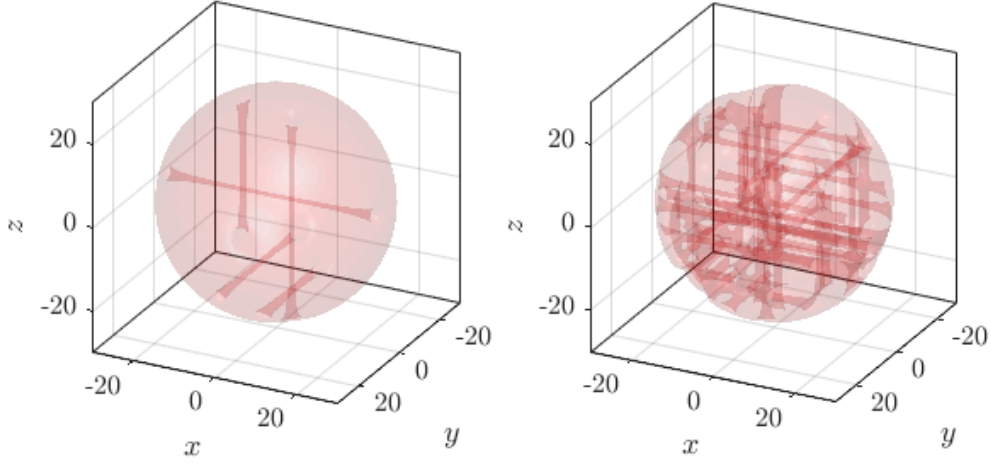
FIGURE 5.9: Isosurfaces of example spherical condensates with (*left*) 5 and (*right*) 50 vortices.

get vortex line density of the system, we evaluate the volume V over the areas of density larger than $n(x, y, z) \geq 0.25$ and calculate the total vortex line length. The vortex line density is therefore

$$\mathcal{L} = L/V. \tag{5.31}$$

The intervortex spacing ℓ in our spherical system is

$$\ell = \mathcal{L}^{-1/2}. \tag{5.32}$$

Interestingly, for our spherical system, both techniques work well, as shown in Fig. 5.10. We see in spherical expanding systems that both methods accurately model the change in the dynamics of expansion; the reliable matching of results presented in Fig. 5.10 is also present in the other cases stated earlier. Looking at the expansion, we see what can be thought of as the most obvious result - the more vortices in the system, the faster it expands (Fig. 5.11).

5.5.2 Expansion of cigar condensates

We further use this to investigate a cigar condensate expanding. We align vortices along the r directions in random locations and directions. We have a cigar condensate of $\omega_{r,z} = [0.08, 0.02]$ and let it expand for a time $t = 150$. We note that Eq. (5.30) again gives a relatively good result. Where it falters is for the $N = 100$ case; it wildly overestimates the ratio of the expansion in the late-time. It must be noted also that the computational result for $N = 100$ failed after $t \sim 120$; the condensate expanded at such a rapid rate that it collided with the edges of the computational
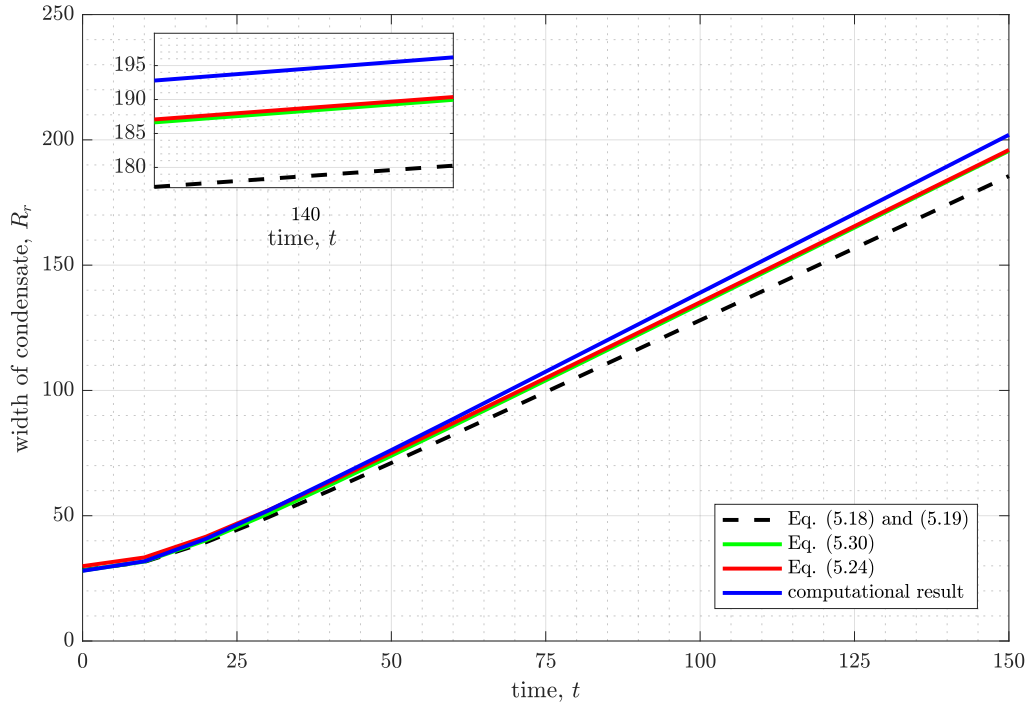
FIGURE 5.10: The predicted expansion of a spherical ground state condensate (black dashed), the result from Eq. (5.30) (green), the re-scaled ODE using the rescaled Thomas-Fermi radii (Eq. (5.24)) (red) and the expansion modelled computationally (blue) of a condensate expanding with $N = 20$ vortices. *Inset:* a zoomed in view of the same data for reference.

domain at around $t \sim 130$. We could not run many simulations or ensemble average the results due to the quantity of computing hours and storage requirements of each simulation. The fact the ODE begins to give a poorer result for systems with larger number of vortices makes sense; such a condensate will have the ratio of $\ell/\xi \to 1$ and therefore $\ln(\ell/\xi) \to 0$. As more vortices are added into the system, the inter-vortex spacing of the condensate becomes smaller and smaller. As this happens, there will be inter-vortex forces at play - something which is not taken into account in the ODE model. The self similar expansion reported in Caracanhas *et al.* [171] was found by minimising Eq. (5.30) for $\mathcal{L}$ and ℓ such that the ratio does not change. It must be noted that even when the model disregards a lot of features, it still holds a good estimation to the inhibition of the inversion of the aspect ratio of the expanding cigar condensate.

5.5.3   Reconnections

The reconnection of vortex lines have been observed in both liquid Helium and atomic condensates [164]. In 2D condensates, reconnections do not occur; vortex-anti-vortex pairs instead undergo *annihilation*. Galantucci et al [54] proposed that
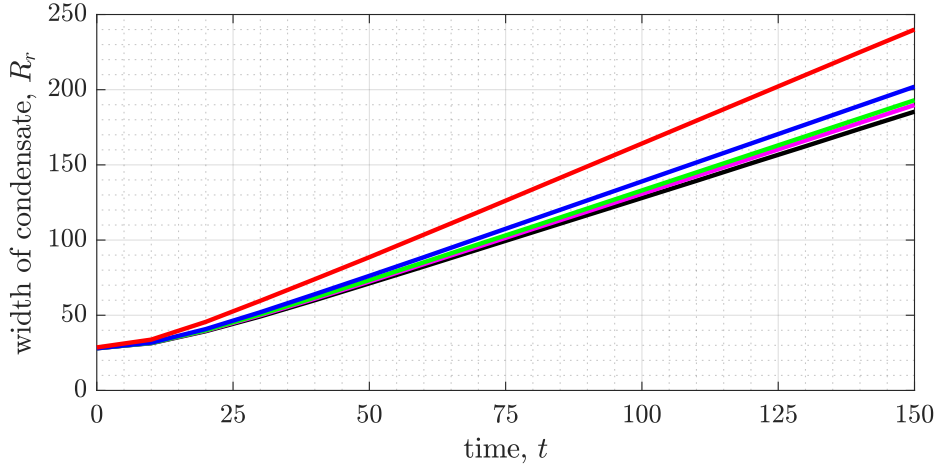
FIGURE 5.11: The calculated widths of an expanding spherical condensate modelled computationally; one vortex (black), five vortices (magenta), 10 vortices (green), 20 vortices (blue), and 50 vortices (red).

in a homogeneous system that there are two scaling dynamics for the reconnection of two vortices and further went on to study reconnections in an inhomogeneous system, observing the reconnections for two vortices within. A harmonically trapped condensate introduces numerous complications - such things include "image" vortices, and the shape and density of the background condensate introduce complexities to the system. We wish to focus primarily on the effect of expansion and therefore keep the system as simple as possible. We first see how vortex reconnection is affected by the geometry of the condensate before moving onto studying dynamics during expansion. We study vortices placed perpendicular to each other (see Fig. 5.13) with a distance from 2ξ to 8ξ. We find that for systems with $\delta_0 > 8\xi$, that the vortices begin to be too affected by the background density and hence do not reconnect in a time feasible in our simulations. We follow Galantucci *et al* [54] in monitoring the minimum distance δ with a rescaled healing length.

We first verify that the shape of the condensate by briefly looking at the differences between three systems; two spherical condensates with $\omega = 0.025$ and $\omega = 0.05$ respectively and a cigar condensate of $\omega_{(r,z)} = (0.050, 0.025)$. With different background condensates, we can test how expansion affects the condensates - as we know from previous sections, the shape of the original condensate dictates the expansion. We chose these three setups as they will all give a different rate of expansion. Visible in Fig. 5.14 is the time of expansion in the trapped systems; we are therefore satisfied that the effect of the background condensate on the reconnection can be neglected in our study. Now that we know how the vortices interact in our system, we can now expand certain situations to see how the vortex dynamics change. We first look at the time of reconnection akin to Fig. 5.14 to identify when the reconnection is frozen. From this, we study the minimum distance $\delta(t)$ as a function of time for the corresponding expanding condensate. We denote the time of reconnection in the trapped condensate as t_n^*. We find that if $t_n^* < 1/\omega_r$, then
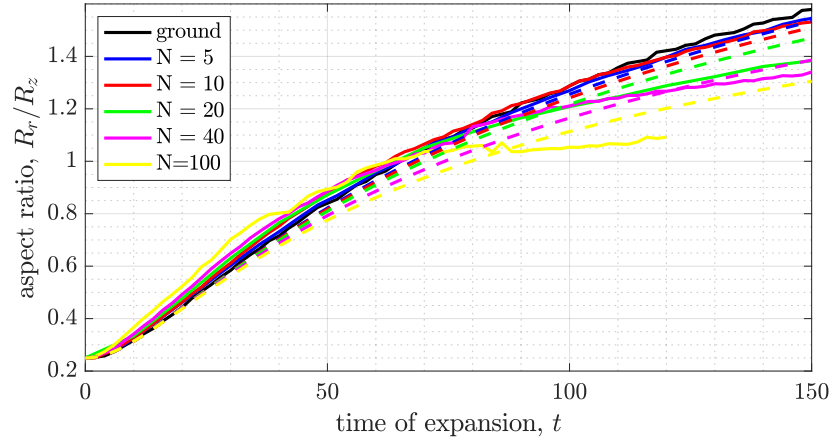
FIGURE 5.12: The calculated widths of an expanding cigar condensate; a solid line denotes the computational result whereas the dashed line denotes the ODE result (Eq. (5.26)) calculated using the estimated vortex line length and inter-vortex spacing from the computational result.
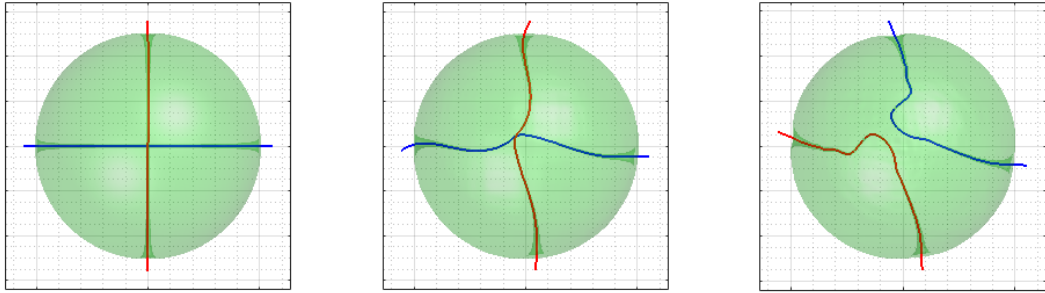
FIGURE 5.13: An example of a vortex reconnection; two perpendicular vortices are placed within a spherical condensate and shown at (a) $t = 0$, (b) $t = 150$ and $c = 200$.

the vortices will reconnect in the expanded case in a time close to t_n^*, with a reconnection scaling $\neq t^{1/2}$ after reconnection. For systems approaching $t_n^* \to 1/\omega_r$, the time for reconnection in the expanding case suddenly exponentially increases. For systems with $t_n^* \geq 1/\omega_r$, the two vortices will never reconnect.

5.6   Expansion of noisy condensates

We have studied the way vortices in a BEC both affect and are effected by the expansion of condensates. As we know, turbulence is not just just a tangle of vortices in a homogeneous background; it contains density fluctuations. The reconnections of vortices is also a mechanism for which sound is introduced into a condensates,
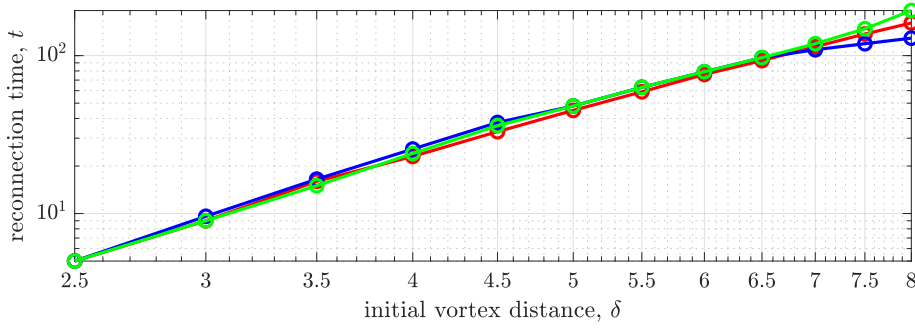
FIGURE 5.14: The time for reconnection of two perpendicular vortices initially at distance δ in a trapped condensate of $\omega = 0.025$ (*red*), $\omega = 0.05$ (*blue*) and $\omega_{(r,z)} = (0.05, 0.025)$.
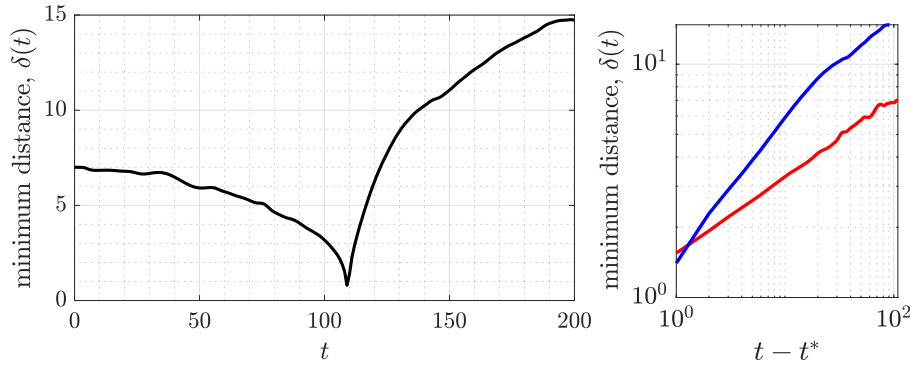
FIGURE 5.15: The minimum distance between two vortices originally 7 healing lengths apart (left) and the same data rescaled (right) to see the difference between the distance of the two vortices before reconnection (red) and after reconnection (blue).

seeding more and more random fluctuations into the system. We therefore artificially add sound into our condensate by adding in randomised sinusoidal fluctuations,

$$\psi = \psi + A \sum_{i=1}^{10} \sin\left(\tilde{\Lambda}\tilde{z}' + \tilde{\phi}_i\right) \tag{5.33}$$

where A is the amplitude, $\tilde{\Lambda}$ is a randomised wavelength, $\tilde{\Lambda} \in [0,1]$ and $z' = \cos\left(\tilde{\phi}_0\right)r - \sin\left(\tilde{\phi}_0\right)z$ with $\phi_{0,1}$ denoting a random angle $\phi_{0,1} \in [\pi/2, \pi/2]$. The resulting condensate (in Fig. 5.16) is then renormalised to the norm of the ground state. We expand two different condensates with $A = 0.1$ and 0.2 respectively and model both how quickly the condensate expands and how the aspect ratio changes. Figure 5.16 shows that there is a slight change to the aspect ratio although one that is relatively insignificant and on par with that of the effect from a single vortex. The widths in the *r* and *z* directions show that overall the condensate expands quicker than that of the ground state. We can conclude therefore that for the expansion of a condensate, the vortices are indeed the most important aspect that governs the way an excited condensate expands.
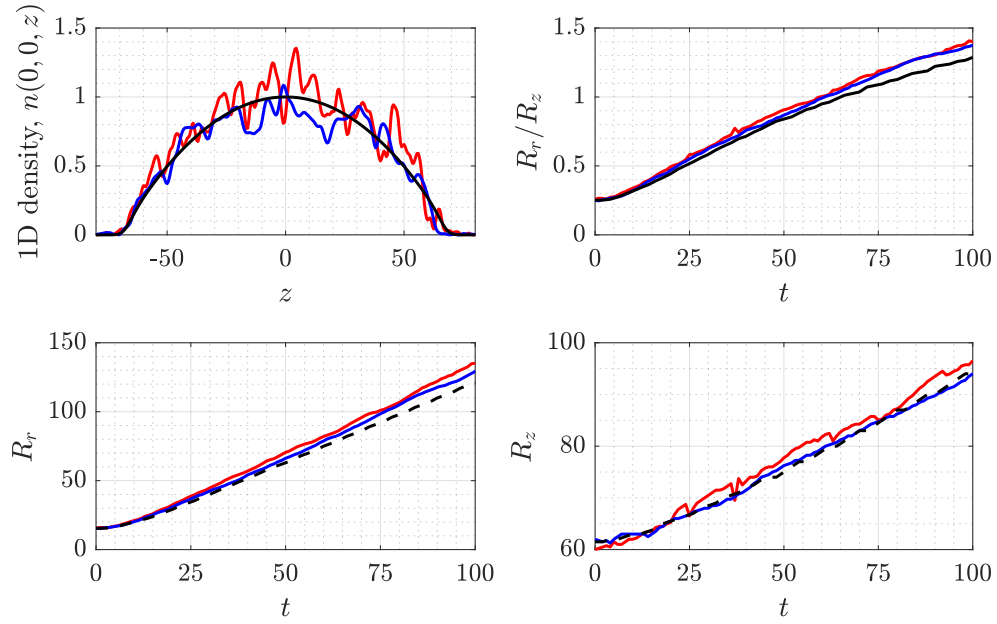
FIGURE 5.16: The (a) one-dimensional density slice before expansion and (b) aspect ratio of the expanding condensates, the width in the (c) r (d) z directions for the ground state (black), $A = 0.1$ (blue) and $A = 0.2$ (red).

5.7   Conclusion

After showing the derivation of the oft-quoted expansion scaling factors for a ground state of a condensate, we began this chapter showing the use of our new computational system to model the expansion of condensates by using the example of an expanding ground state. We study various analytical predictions, including how good estimations of vortex energy are when applied to simulations before presenting the analytical prediction of another groups. We then verify the preciseness of their prediction and conclude the result matches very well for a spherical expanding condensate and matches well (to a limit) to the expanding cigar condensate. We finally show that density fluctuations negligibly effect the nature of expansion in a condensate and thus conclude it is indeed vortices that bring about the suppression of the aspect ratio inversion.

6 Generation of Turbulence in a Mechanically Driven Condensate

6.1 A comment on experimental and numerical methods

The work presented in this chapter was in collaboration with the group of the Sao Carlos group in Brazil and is the topic of a joint theory and experimental paper submitted to Physics Research Reviews [15].

6.1.1 Experimental Procedures

A cloud of $N = 3 \times 10^5$ [87]Rb atoms is confined in a magneto-optical trap, cooled to around 140μK, and then transferred by radiation to a second magneto-optical trap, which captures, accumulates and allows cooling to temperatures of a few μK. After this new entrapment and cooling, the optical fields are switched off, and the atoms are transferred to a magnetic trap composed of several coils forming a so-called IOFFE-PRITCHARD trap. Once in this trap, radio-frequency fields operating at a few MHz promote transitions causing the sample to evaporate. The loss of atoms during this phase is compensated by cooling, reaching temperatures of the order of 100nK, where condensate begins and progresses, until we have a condensate fraction ranging from 50% to 80% of the total atoms. The condensate is trapped into a elongated harmonic potential with $\omega_r = 2\pi \times 21$ and $\omega_z = 2\pi \times 130$. Once the condensate has been successfully cooled within the final trap, a secondary oscillating magnetic field is applied to the condensate. Here, a pair of anti-Helmholtz coils is applied close to the longitudinal axes of the static trap. The condensate is driven for a time, before the anti-Helmholtz coils are turned off and the system is left to evolve in the IOFFE-PRITCHARD trap. After the condensate is held for a time, T_H, it is allowed to expand freely for a period of 20 to 40 ms. At the end of this free-flight, a resonant probe laser takes an absorption image, revealing the 2D projection of the expanded density. This projection allows the extraction of the momentum distribution as well as the fluctuation profile. For more details on the measurements and experimental techniques we refer to back to Refs. [7, 41, 174]).

6.1.2 Computational Methods

To match the experimental study with parameters reported to us from our collaborators, we reformulate the Gross-Pitaevskii equation into the *harmonic oscillator units*, Eq. (6.1),

$$i\frac{\partial \psi}{\partial t} = -\frac{1}{2}\nabla^2 \psi + \mathcal{C}|\psi|^2\psi + V\psi' - \mu\psi. \tag{6.1}$$

and the normalization $\int |\psi|^2 d\mathbf{x} = 1$. The parameters are chosen to match those of the experiment; the resulting dimensionless chemical potential and longitudinal trapping frequency are respectively $\mu = 8.$ and $\omega_z = 0.11$. These values, combined with the large oscillation which is imposed to the condensate, would require a computational domain too large to simulate numerically. For this reason we increase the longitudinal trapping frequency to $\omega_z = 0.5$. The dimensionless interaction parameter $C = 4\pi a N / \ell$ is calculated using all the experimental values, albeit with the stronger trapping in the longitudinal direction, obtaining $C = 1715$. The mechanical driving detailed in Section 6.1.1 is modelled computationally. The trapping potential here, V, is a combination of the aforementioned harmonic trapping potential, V_{harm} and an oscillatory driving force,

$$V_{osc}(x,y,z,t) = A\mu[1 - \cos(\Omega t)]z'/R_z, \tag{6.2}$$

and is visually represented in Fig. 6.2. The parameters A, Ω and z'/R_z denote the amplitude, frequency and length of the driving with R_z being the Thomas-Fermi radius in the z direction, $R_z = \sqrt{2\mu}/\omega_z$ and z' being the direction of driving, $z' = \cos\theta_z z - \sin(\theta_z)$, where $\theta_z = 5°$ to break the computational symmetry. We match the value of the amplitude A, frequency Ω, and time T_D to the experiment with $A = 1.25$, and $\Omega = 0.97$ and $T_D = 10\pi/\Omega = 32.4$ (all values are reported in non-dimensional units). The direction of the driving is $z' = \cos(\theta_z)z - \sin(\theta_z)x$ where $\theta_z = 5°$ breaks the symmetry of the system around the z-axis [7, 41, 174, 175]. For $t > T_D$, the condensate is left to evolve and oscillate for T_H in the static harmonic potential. In the experiments, images of the condensate are typically taken from a light source which has travelled through the expanding condensate in the imaging plane after the trapping harmonic potential has been switched off. During the time-of-flight (TOF), the momentum distribution is obtained by observing the number of atoms travelling different distances from the beginning of the ballistic motion. Our group and others [11] have demonstrated the validity of the TOF technique to obtain the 2D column-integrated density spectrum $n(k)$ for a self-similar turbulent cloud. In our original study, we did not expand the condensate but obtained the momentum distribution from the column-integrated density,

$$n(x,z) = \int |\psi(x,y,z)|^2 dy. \tag{6.3}$$

6.2   The onset of turbulence

Figure 6.2 shows the shape of the condensate during the evolution, from (a) the initial ground state, to (b) the generation of deep density waves in the form of dark solitons, to (c) the turbulent state.

It is natural to ask what nucleation process of vortex lines is in the absence of an external, small-scale stirring potential ('laser spoon') [176, 177]. The process is more clear during the first oscillation of the condensate, before it is masked by large density fluctuations. For a large driving amplitude ($A > 1$), dark solitons (nonlinear waves characterised by a localised dip in the density and a step in the condensate phase) appear at the front of the condensate moving in the $-z$ direction (Fig. 6.2(b)). Solitons have previously been generated in condensates via a variety of techniques
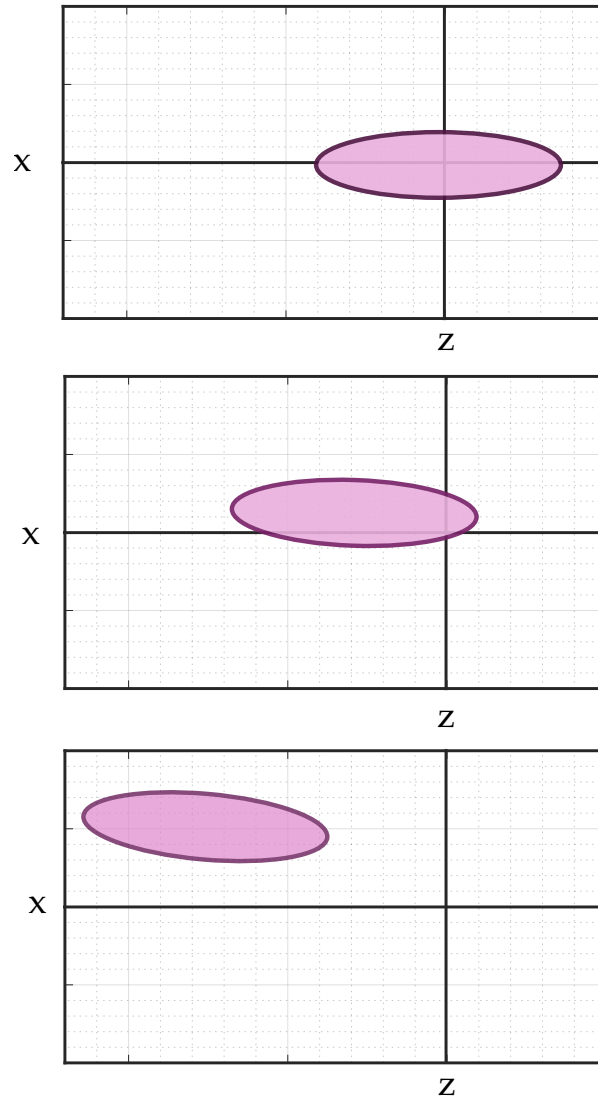
FIGURE 6.1: Three diagrams of a Thomas-Fermi profile in the driving potential (Eq. 6.2) at three times; (top) at $t = 0$, (middle) at $t = \pi/4\Omega$, and (bottom) at $t = \pi/\Omega$ (the drivings maximum) in the (z, x) plane. Note that the effect in the x plane is exaggerated in this diagram for the readers convenience. For $\pi/\Omega < t < 2\pi/\Omega$, the Thomas-Fermi profile returns to the (top) position. As well as a displacement in both the x and z plane, the potential also imparts a slight rotation to the condensate.
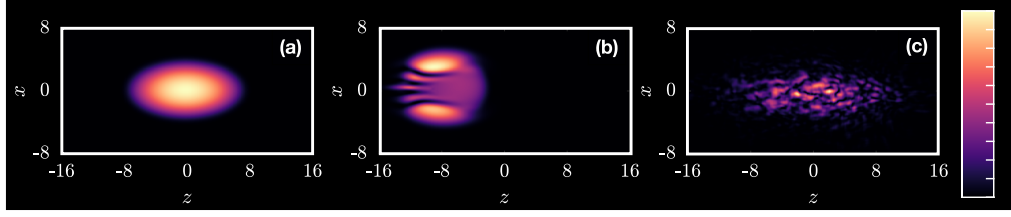
FIGURE 6.2: 2D density slices $n(x, y = 0, z)$ of the simulated condensate at (a) $t = 0.0$ (the ground state), (b) $t = 4.9$ (nucleation of solitons) and (c) $t = 35.2$ (turbulent state with vortices and strong density waves).
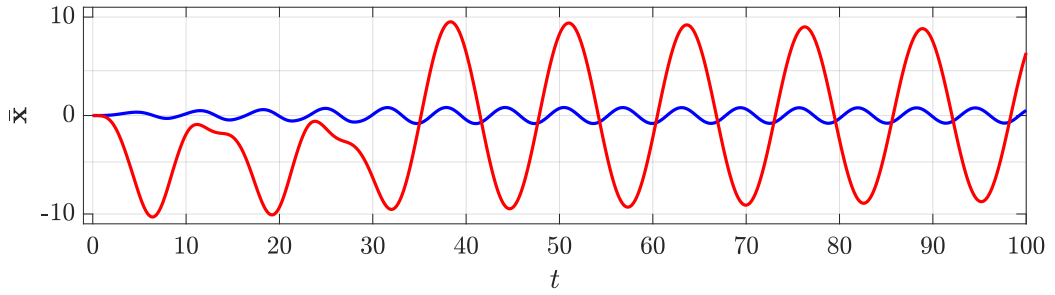
FIGURE 6.3: The centre of mass motion $\bar{x}$ in the x (blue) and z direction (red).

but are stable only in quasi-1D systems, as discussed earlier in the thesis. Indeed, the solitons quickly break down into vortex lines and sound waves [178], which respectively multiply and grow in size as the shaking continues (Fig. 6.2(c)). For $t > T_D$, the condensate moves unforced and undergoes large oscillations about the minimum of the trapping potential, with a detectable breathing mode also present. The change in the centre-of-mass of the condensate is shown in Fig. 6.3; in the beginning there is an observable coupling in the centre-of-mass in both the x and z directions, corresponding to the frequency of the driving, Ω, and the condensate's dipole frequency. Once driving have stopped at $t = 32.4$, the condensate moves in each direction at the condensate's dipole frequency (the dipole frequency in each direction is equal to the trapping frequency in that direction). As well as the dipole mode, the monopole mode is also triggered. During the oscillation, the condensate retains a shape similar to the initial cigar-shaped profile only when the centre of mass is near the the potential minimum at $z = 0$; it is most distorted when far from this minimum, near the points where the centre of mass reverses its direction. The most notable features of the obtained turbulent state at $t > T_D$ are the observed large density oscillations shown in Fig. 6.4, where experimental absorption images, necessarily 2D (Fig. 6.4(a)), are compared (Fig. 6.4(c)) to computed 2D column integrated density fields $n(x, z)$, defined in Eq. (6.3). To better appreciate the non-homogeneous density characterising the turbulent state, in Fig. 6.4(b), (d) we also report the corresponding 1D density profiles.
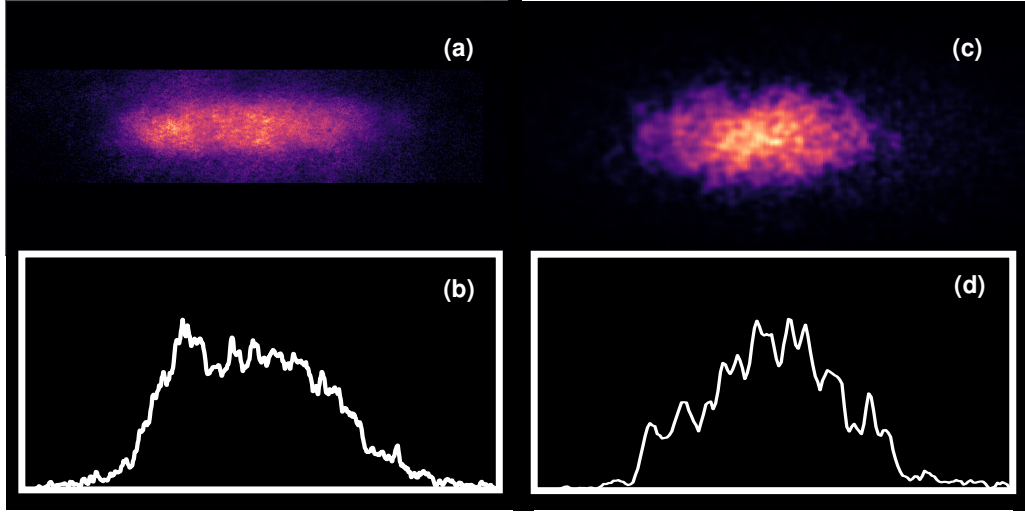
FIGURE 6.4: Panel (a) shows an absorption image of a turbulent condensate, at t=75 which has to be compared to panel (c) with the computed 2D column integrated density $n(x, z)$ at t=66.8 (as explained in Methods, the computed condensate is less elongated in the longitudinal direction). Panels (b) and (d) correspond to 1D slices of the density at $x = 0$, showing large fluctuations on top of a background density.

6.3   Momentum distribution of an expanding condensate

To quantify and characterise the observed density oscillations in their results, experimentalists typically measure the momentum distribution obtained from their 2D absorption images, denoted as $n(k)$, where k is the magnitude of the wavenumber. Due to the inability to measure complicated vortex structure and energies in a turbulent BEC, the momentum distribution remains the main way of evaluating any cascade [8, 179]. To replicate this computationally, we employ the same technique by measuring the column integrated density of the expanding turbulent condensate,

$$n_{CI}(x, z) = \int |\psi(x, y, z)|^2 dy, \tag{6.4}$$

and expand the condensate from $t = 66$ ($t_E = 0$). Due to the sinusoidal movement of the driven condensate (shown in Fig. 6.3), we model the expansion of the condensate in the moving frame,

$$i\frac{\partial \psi(\mathbf{x}, t)}{\partial t} = -\left[\frac{1}{2}\nabla^2 + \mathcal{C}|\psi(\mathbf{x}, t)|^2 + iv_{\mathbf{x}, t}\frac{\partial \psi(\mathbf{x}, t)}{\partial \mathbf{x}}\right]\psi(\mathbf{x}, t), \tag{6.5}$$

where the speed $v_{\mathbf{x}, t}$ is calculated from the centre-of-mass of the condensate at time t (see Fig. 6.3).

We compute the column integrated 2D density at different times t_E after the beginning of the expansion of the turbulent BEC at $t = 66$, and, assuming ballistic expansion, and relate the position $\mathbf{x}$ on the enlarged condensate [8] to the wavenumber $\mathbf{k}$ of the atoms before the expansion. Following the experimental procedure, we assume isotropy such that $\mathbf{k}^2 = k_x^2 + k_z^2$; by angle averaging over this 2D space,
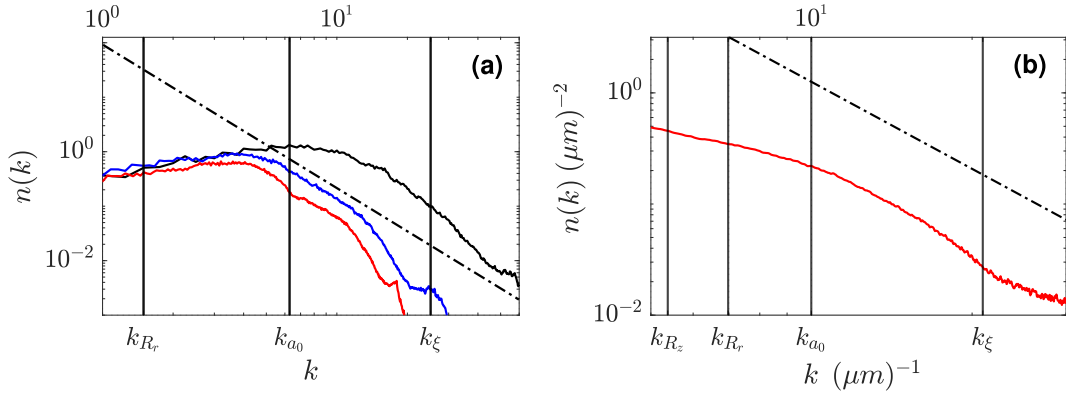
FIGURE 6.5: The momentum distributions obtained from (a) an expanding numerical condensate released at $t = 66$ and (b) an average of 10 experimental images of the expanding turbulent state at an expansion time of 30ms. The different distributions shown in (a) correspond to the expanding condensate at expansion times $t_{exp} = 0.5$ ($t = 66.5$) (black), $t_{exp} = 1.5$ ($t = 67.5$) (blue) and $t_{exp} = 2.5$ ($t = 68.5$) (red). The early time expansion of $t_{exp} = 0.5$ is given to highlight the convergence in the later time results. The power law fits, superimposed to each graph for reference, are $k^{-2.6}$ for both (a) and (b). Figure (b) is presented in SI units.

one then gains a 1D momentum distribution. Doing this for both the column integrated density from Eq. (6.4) and the result from an average of 10 experimental runs, we compare the momentum distributions obtained from the experimental and computational methods. Although the experimental assumption of a point-like density at $t = 0$ is not true for our computational results, we can immediately see the agreement of the distributions in Figs. 6.5(a) and (b). As stated earlier the distribution is reliant on the expanded image being much larger than the initially trapped condensate - we therefore check for convergence in the distributions given by the condensate at different times of expansion, $t_E = 2.0$ to 2.8. Although the width of the cascade is smaller in the computational result compared to that of the experiment, the fitted exponents $n(k) \sim k^{-\alpha}$, agree at $\alpha = 2.6$. It can thus be concluded that our computational modelling is indeed reproducing the experimental results.

As discussed earlier in this thesis, the maximum value we can expand our condensate to is smaller than that of experimentalists. We therefore check the convergence of the value of the fitted exponent. Figure 6.6 shows that the power law behaviour in the momentum distribution at different times does indeed show a rapid convergence - the distribution in the region between the healing length and the core radius averages shows . When the fitting for the exponent between $k_{2\xi}$ and $k = 2\pi/4\xi$, the average power law is shown to be $\alpha = 2.6$ (the inset to Fig. 6.6 shows the individual α value at each time).

To ensure that the results of the momentum spectra are due to the nature of the turbulence and not just the edge of the condensate's shape, we also present the results for a model condensate. We characterise the topology and length of the vortices within the driven turbulent condensate (this characterisation of the vortices is explained in the next section and shown in Fig. 6.8), and expand a cigar condensate
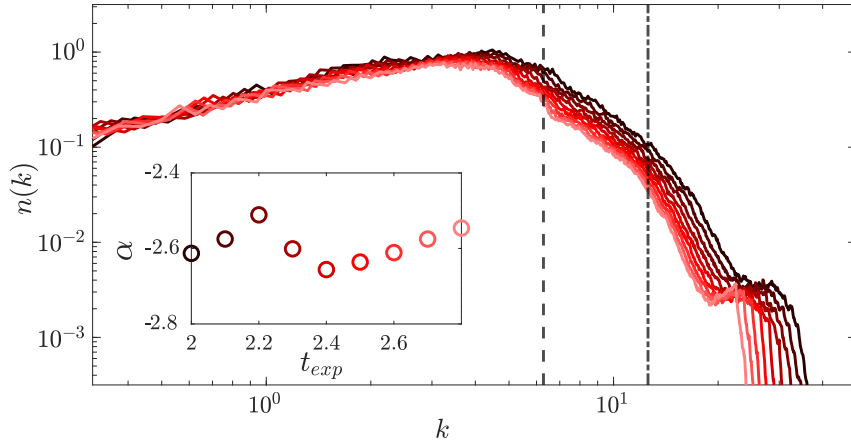
FIGURE 6.6: The momentum distributions from $t_{exp} = 2.0$ to 2.8 ($t = 68.0$ to 68.8) (going from dark to light) with the boundaries of fitting marked by $k = 2\pi/4\xi$ (vertical dashed line) and $k = 2\pi/2\xi$ (vertical dot-dashed line) and (inset) the power exponents for each of the momentum spectra in the corresponding colour.

with vortices added in of the same nature as detected in our turbulent condensate; we reproduce here both the locations and the radii and general shape of all the detected vortices in the turbulent state. We see in Fig. 6.7, that an expanding condensate with the same size and vortex structure does not reproduce the scaling law that has been presented in both the experimental imaging and the computational modelling of the experiment; where both former results gave an exponent of $\alpha = 2.6$, the simplified model shows a lack of any clear scaling law. This disagreement in results shows that the momentum distribution is not simply a measure of the shape of the condensate or the vortices within, but has captured the complicated dynamics of the driving.

6.4 Characterisation of vortices

Besides large density fluctuations and fragmentation, the turbulent condensate contains vortex lines, clearly visible in the numerical simulations. Surprisingly, the vortex configuration is very different from turbulence in superfluid helium. We identify the vortex lines in the simulation using a vortex tracking algorithm established elsewhere for homogeneous or smoothly-varying condensates [101, 105, 180]. In our highly-fragmented system, it is numerically challenging to identify vortices when the condensate is off-centre in the trap (*i.e.* when the condensate is most fragmented and loses a discernible shape). We hence focus on vortex reconstruction when the condensate lies at the centre of the trap. The turbulent condensate and vortex lines therein at $t = 35.2$ is shown in Fig. 6.8. It is apparent that there are two kinds of vortex lines: small vortex rings (shown as blue lines in the figure) and short open vortex lines which terminate at the condensate's boundary (shown as red lines). These open vortex lines are shorter versions of the *U-shaped vortices* discussed in the literature of non-turbulent condensates [164, 181–183]. Both vortex rings and U-vortices are small, of the order of the vortex core size a_0. The lack
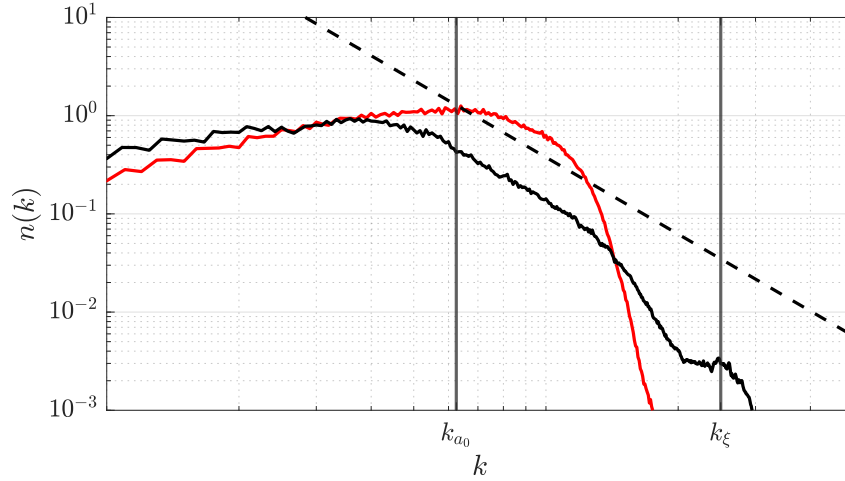
FIGURE 6.7: The momentum distributions of the expanding turbulent condensate at $t_E = 1.5$ (black, reproduced from Fig. 6.5(a)) and a condensate with artificially inserted ring vortices expanded at $t_E = 1.5$ (red). The scaling law $\sim k^{-2.6}$ (black dashed) is plotted for reference. Marked are the locations of the k values corresponding to the healing length of the system k_ξ and the size of the vortex core k_{a_0}.
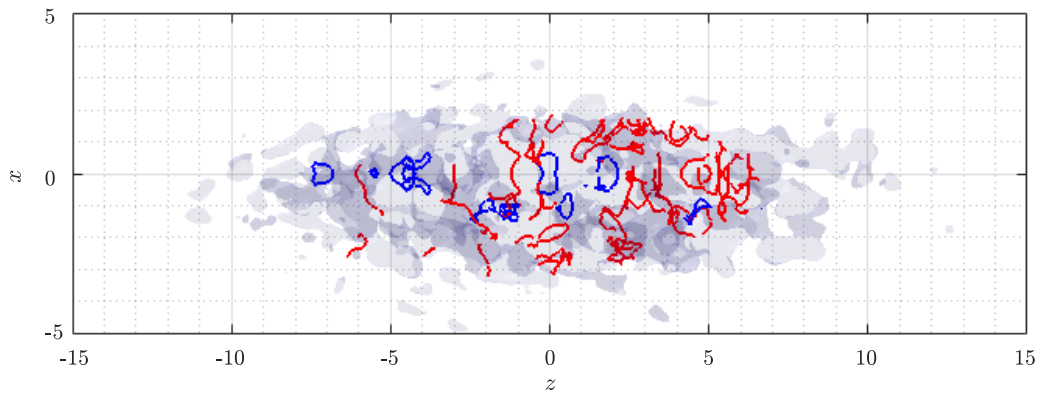
FIGURE 6.8: The isosurface of the condensate at $t = 35.2$ with vortices marked. Line vortices that terminate at the condensate boundary are denoted in red whereas ring vortices in blue. Note that darker patches do not denote larger density, but reveal the fragmented nature of the condensate, as they result from the line of sight crossing the semi-transparent density isosurfaces multiple times.
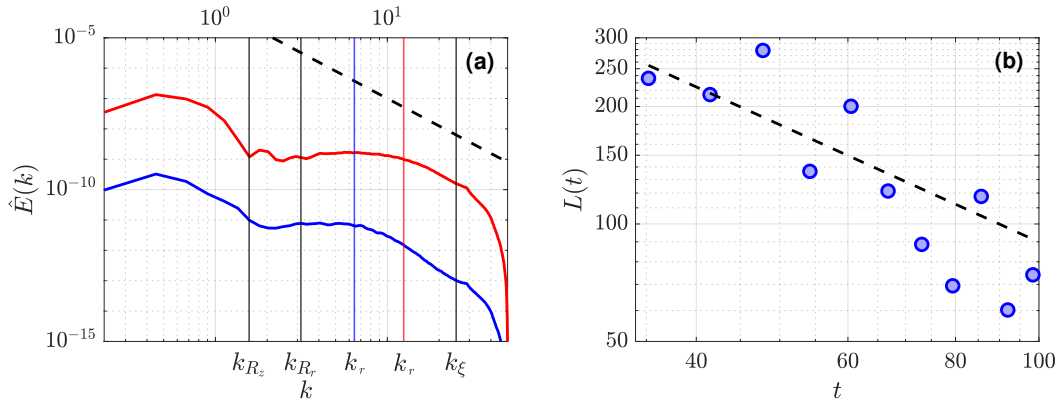
FIGURE 6.9: (a): The numerical incompressible energy spectra $\hat{E}(k)$ of the condensate at times $t = 35.2$ (blue) and $t = 92.0$ (red). The dashed line, $\propto k^{-3}$, is drawn for reference. The spectra are shifted vertically for clarity. The vertical lines indicate the wavenumbers k_{R_z}, k_{R_r}, and k_ξ corresponding in physical space to the longitudinal and radial Thomas-Fermi radii R_z and R_r, and to the healing length ξ, respectively. The wavenumbers k_r (marked in blue and red at the respective times) correspond to the average vortex radius size at the given times. (b): total vortex line length $L(t)$ vs time t; the dashed line $\propto t^{-1}$ is given for reference.

of homogeneity of the vortex configuration is immediately visible in the figure. Although just after T_D vortices are distributed more-or-less uniformly throughout the system, at later times most vortices reside at the back of the moving condensate. When $\bar{z} = 0$, as shown in Fig. 6.8, the vortex rings tend to be located along the central z-axis of the condensate, while U-vortices tend to be more clustered towards the rear of the moving condensate which in Fig. 6.8 is moving towards left. The orientation of the vortices, however, is fairly uniform. The vortex length in each projected Cartesian direction falls between 30 and 40% of the total length at each time analysed. It is therefore fair to conclude that in a turbulent condensate the vortex tangle is isotropic but not homogeneous. It is interesting to remark that, according to numerical simulations, small vortices have also been observed along the edges of a condensate excited by oscillating a boxtrap potential [11].

6.5 Energies

We are able to computationally analyse the individual energies within the condensate. The condensates potential energy varies largely over the time; this makes sense considering the strong dipole motion of the condensate (see Fig. 6.3). When the condensate is in the centre of the harmonic trapping, the incompressible energy is largest. As we know, the incompressible energy of the system corresponds to the phase defects (e.g. vortices).
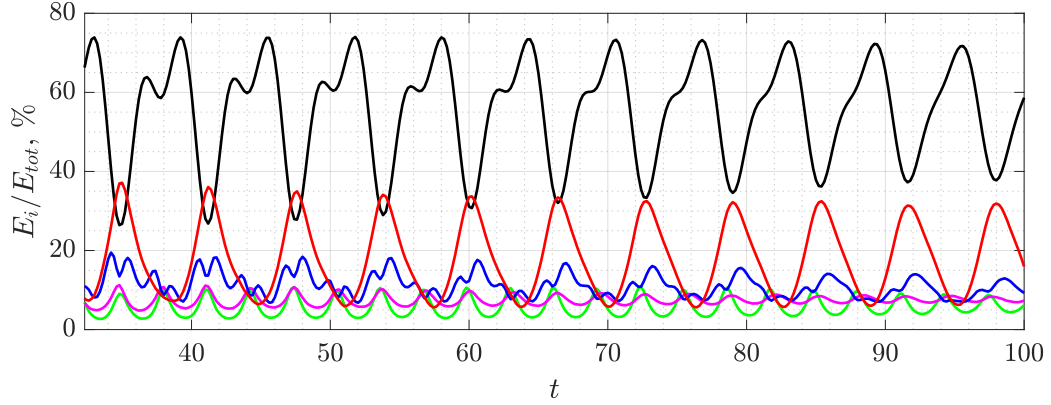
FIGURE 6.10: The percentage of each energy component of the calculated total energy of the system at $t > T_D$: potential (*black*), interaction (*green*), quantum (*magenta*), compressible (*blue*) and incompressible energy (*red*).

6.5.1   Energy spectra

The current understanding of 3D quantum turbulence in superfluid helium arises from combined experimental, numerical and theoretical investigations [184] of the energy spectrum, $\hat{E}(k)$, defined by $E_i = \int_0^\infty \hat{E}(k)dk$ where k is the wavenumber and E_i is the total, incompressible, turbulent kinetic energy. The importance of $\hat{E}(k)$ is that it describes the energy distribution over the length scales, thus revealing inter-scale energy transfers. The key property of classical turbulence (described by the incompressible Navier-Stokes equation) is the celebrated Kolmogorov scaling $\hat{E}(k) \sim k^{-5/3}$. In superfluid helium there appear to be two limiting regimes of quantum turbulence [185]: a *Kolmogorov regime* characterized by the same $\hat{E}(k) \sim k^{-5/3}$ observed in classical turbulence, indicating the existence of an energy cascade; and a *Vinen regime*, which is akin to a random flow, in which the energy spectrum peaks at the mesoscales Δ and decays as k^{-1} at lengthscales smaller than Δ and larger than the vortex core a_0. Unfortunately, the energy spectrum of turbulent 3D condensates is experimentally unavailable due to the lack of local velocity probes. There are also two significant differences with respect to liquid helium. Firstly, condensates are very compressible and become easily fragmented (whereas the Kolmogorov scaling assumes constant density). Secondly, condensates are relatively small, so the spectrum extends only over a limited range of length scales, hindering any scaling law. In this respect, the comparison with liquid helium is staggering: the spatial extension of an atomic condensate is typically of the order of 10^2 times the size of a vortex core, whereas in helium experiments [186] the size of the system can be as high as 10^{10} vortex cores. To make progress, in our numerical part of the study, we obtain the energy spectrum $\hat{E}(k)$ of the turbulent condensate by extracting the incompressible kinetic energy contribution, E_i, from the total kinetic energy via a standard Helmholtz decomposition [187]. The spectrum computed at two different times $t > T_D$ when $\bar{z} = 0$, is reported in Fig. 6.9(a), showing no significant temporal dependence. The figure also shows the wavenumber corresponding to the

average radius of the vortices at each time, defined as $L/2\pi$ for vortex rings and L/π for U-shaped vortices. In the range $1.5k_{a_0} \approx 10 < k < k_\xi \approx 25$ the energy spectrum scales approximately as k^{-3}, while no other scaling is observed at larger scales. At later times ($t = 92$) the average radius decreases with the range of the k^{-3} scaling decreasing accordingly. The k^{-3} scaling, in contrast to both Kolmogorov's and Vinen's spectra, directly stems from the small size of the vortices observed in our turbulent condensate. In fact, the k^{-3} spectrum reported between k_{a_0} and k_ξ coincides, as expected, with the incompressible kinetic energy spectrum inside the core of a quantum vortex [187]. On the other hand, at smaller k, we lack the k^{-1} spectrum (which one would assume given the random orientation of the vortices [83]) precisely because the radii of the vortex rings are of the order of vortex core: there is no separation of scales between the radii of the vortex rings and their core, essential in order to observe the k^{-1} scaling. Indeed, if we compute the spectrum of a homogeneous gas of small vortex rings, we recover the same k^{-3} scaling for $k_{a_0} \lesssim k \lesssim k_\xi$, without further scalings at large scales..

6.6 Vortex rings in homogeneous systems

It is known that the energy spectrum of a single straight vortex line of infinitesimal thickness in a fluid of constant density decays as k^{-1}. If the vortex line is in the shape of a ring of radius R, the energy spectrum [188] rises as k^2 for small k, peaks at $kR \approx 1$, and decays as k^{-1} at larger k with characteristic small amplitude oscillations. A gas of random vortex rings [189] has a similar spectrum, the precise crossover between the k^2 and k^{-1} behaviours depending on the distribution of values of R. It is also known that in a homogeneous condensate, the kinetic energy spectrum at very large wavenumbers in the region $k \leq k_\xi$ scales as k^{-3} due to the presence of the singularity at the core [187]. Consider a gas of random vortex rings
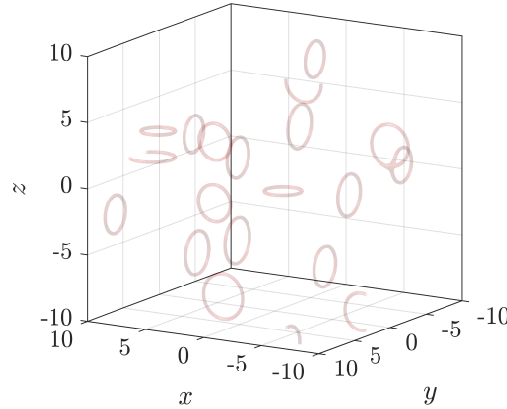
FIGURE 6.11: An example isosurface for a gas of vortex rings in a homogeneous background. The rings are placed randomly throughout the computational box with random orientation and direction of circulation (-1 or 1) with a radius randomly set between 4 and 6 healing lengths.

in a condensate. If the radii are small (of the order of the vortex core size) the region where the spectrum scales as k^{-1} disappears, and we are left with a k^{-3} spectrum at large k. We have verified this result by computing such spectrum in a homogeneous condensate (see Fig. 6.11). In this calculation, the rings are randomly placed within a homogeneous background, with a radius randomly, but uniformly, chosen between 4ξ and 8ξ. This range of radii is chosen to follow the radii of the vortex rings detected in our turbulent cigar condensate. The spectra of said homogeneous condensate is presented in Fig. 6.12, where the spectra for systems of $N = 1, 20$ and 40 rings is shown. Figure 6.12 (a) shows that the incompressible energy spectra of the turbulent condensate have the same k^{-3} scaling of the homogeneous condensate in the large-k regime for $k > k_{a_0}$. Figure 6.12 (b) highlights the differences in the spectra in the condensate with smaller and larger rings.
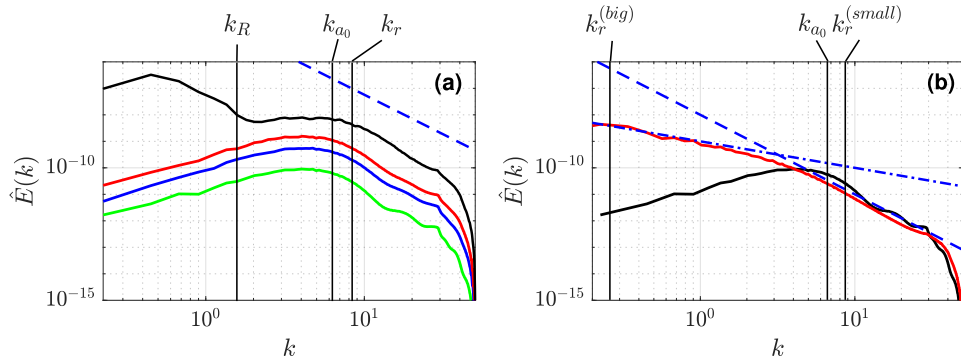
FIGURE 6.12: The incompressible energy spectrum (a) of gas of small vortex rings; $N = 1$ (green), $N = 20$ (blue) and $N = 40$ (red) with the result of our turbulent spectra at $t = 35.2$ (black) with the wavenumbers corresponding to the the Thomas-Fermi radius in r, k_R, the average width of the vortex core k_{a_0}, and the radius of the average ring size, k_r. The (b) $N = 1$ result is repeated (black) accompanied by the spectra of a single large ring of radii 25 (red) with the matching k numbers of the respective radii of the big ring case, $k_r^{(big)}$, the width of the vortex core k_{a_0}, and the radii of the small ring $k_r^{(small)}$. The scalings $\propto k^{-3}$ (dashed), and $\propto k^{-1}$ (dot-dashed) are marked for reference in blue.

6.7   Vortex decay

The random character of the vortex tangle is confirmed by the computed temporal decay of the total vortex length, which is itself a characteristic feature of the turbulent state. Indeed, by measuring the temporal behaviour of the vortex length at all times when $\bar{z} = 0$, we find $L(t) \sim t^{-1\pm0.2}$ (Fig. 6.9(b)) matching the length temporal decay in the Vinen (random flow) regime, observed both in helium [76] and numerically in atomic condensates when the turbulence is created by the instability of antiparallel multicharged vortices [83]. This temporal decay behaviour is clearly distinct from the $L(t) \sim t^{-3/2}$ decay observed in Kolmogorov superfluid helium turbulence [58, 59, 190]. We note that we monitor the total vortex line length and not the incompressible energy due to the large fragmentations which have a
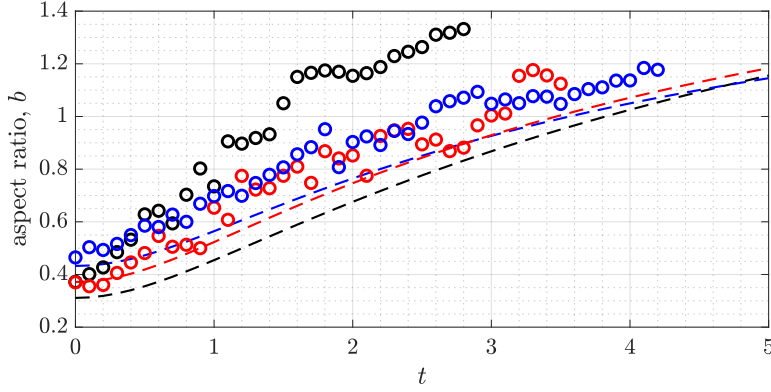
FIGURE 6.13: The measured (circles) values aspect ratio $b = R_x/R_z$ of the expanding condensate at time t, released at $t_E = 35.2$ (black), $t_E = 41.5$ (red) and $t_E = 66.8$ (blue), plotted with the analytical predictions of the

vorticity, which means the incompressible energy is not from vortices alone in this condensate.

6.8 Expansion of the turbulent state

In Section 6.3, we showed how modelling the expansion of the driven condensate in the moving frame (Eq. 6.5) can be used to produce a momentum distribution which matches the experimental data. As reported in experimental papers, a turbulent condensate have a self-similar expansion.

We measure our aspect ratio in the same way as presented in Section 5.2, to find that the expansions from later times (and therefore with less vortices) provide a change in aspect ratio that inverts less compared to the earlier release time of $t_E = 35.2$. We find that there is no conclusive results for the lack of aspect ratio inversion (see Fig. 6.13) we therefore investigate this later.

6.9 Conclusion

In conclusion, we can see that we have been able to accurately model the Sao Paulo experiment. We find that large scale driving of condensates creates large scale modes, a lot of sound waves and small scale vortices within the condensate. The nature of the vortices mean that the usual incompressible energy scaling often associated with Vinen turbulence is altered; the small rings mean that only the k^{-3} scaling is detectable. Although different topologically to the usual vortex turbulence in quantum fluids, they decay in the same way, with the well documented $L(t) = t^{-1}$ scaling observed. We modelled the only experimentally viable measurement - the density spectrum, and concluded that it matches the experiment well. There were difficulties in taking the Time-of-flight measurement of the condensate - the large dipole mode means a difficulty in modelling the expansion. We use the

GPE in the moving frame to counter-act this, however the range of expansion is still small. One should state that even in this small time of expansion, the result of $\alpha = -2.6$ is a converged value.

7 Proposal for the generation of turbulence

So far in this thesis, we have developed an understanding to the expansion of condensates with uncomplicated layouts of vortices and sound waves. This includes the artificial addition of vortices and density fluctuations. We have also provided an explanation and understanding to the results of Vanderlei Bagnato's experimental group with a brief look into the expansion there. We highlighted the issues in the analytical and numerical study. In Chapter 6, the system had both a harmonic potential V_{harm} and oscillating driving V_{osc} (Eq. (6.2)). This oscillatory driving provides a large-scale push in the $-z$ direction and causes ring solitons. We also know that it gives a very large dipole mode which causes difficulties in the computational simulation. This strong, undamped, dipole motion also means that one cannot expand for a time on the scale of an experiment. The size of this dipole mode also means that we have to keep the condensate smaller than, for example, the condensates in Chapter 5 so that we can run the system for a workable computational domain. One thing not yet discussed in that the Sao Paulo and Cambridge [11] have the same driving with a difference from the background potential. A dipole mode is not seen in the Cambridge case and reminds one of the work discussed in our early chapter in 1D condensates - changing the trapping frequency of a harmonically trapped condensate gives a monopole mode - a perpetual expansion and retraction of the condensate's width. If however one alters the width of a trapping potential in a 1D box potential, one creates a train of solitons and sound waves. This difference in dynamics is likely the reason why such different results are reported by the groups. We are therefore inspired to use this curious result to propose the creation of turbulence which is independant on the shape of the condensate. Ideally, we wish to create as many vortices as possible with as little ignition of any modes, displacement of the condensate bulk or the production of noise. As shown in the last chapter, the vortices created had very small individual length and such the type of turbulence created was distinct from that previously derived analytically and modelled computationally. We therefore wish to be able to drive to a state of vortices with large length in order to observe the traditional types of vortex turbulence (be that Kolmogorov or Vinen) in an experimentally achievable way.

7.1 Form of potential

In Section 2.8 we outlined the use of a DMD, a proven way to create arbitrary potentials on a condensate. With such a device, one is able to project a two-dimensional image onto a condensate. If, for example, a bar of high potential is projected onto a condensate, it will create a well of low density throughout the condensate. If this

bar is removed, the two edges will collide and a train of solitons will be formed, just as it was in the 1D system in Chapter 4. It must therefore be that if one imprints many bars onto a condensate in a striped manner and then subsequently releases them, many solitons will be formed without imparting any net momentum or movement that will cause numerical complications. We trialled a few different ideas before settling on a relatively simple scheme. We therefore take inspiration from Chapters 4 and 6 so propose a driving of the form.

$$V_{osc}(z',t) = A \sin(\Omega_t t) \sin(\Omega_x z').$$ (7.1)

Here, one therefore applies sinusoidal bands of potential whose amplitude changes over time, at a given direction $z' = z\cos(\theta) - x\sin(\theta)$. We assume that the potential has no dependence in the y (imaging) direction. The amplitude, A, of the driving needs to be sufficiently large so that the condensate's density needs to fall to 0. An example sketch is given in Fig. 7.1. Trying other patterns such as a grid or checkered shape (inspired by liquid helium grid experiments) also created vortices, however they resulted in small vortex rings akin to the Sao Paulo experiment.

There are four parameters in this proposal; the amplitude of driving A, the width of the potentials bar defined as $2\pi/\Omega_x$, the time-length of the driving $2N\pi/\Omega_t$ with N drives and the direction of driving given by the angle of driving $z' = z\cos(\theta) - x\sin(\theta)$. Due to the number of parameters, we simply cannot achieve
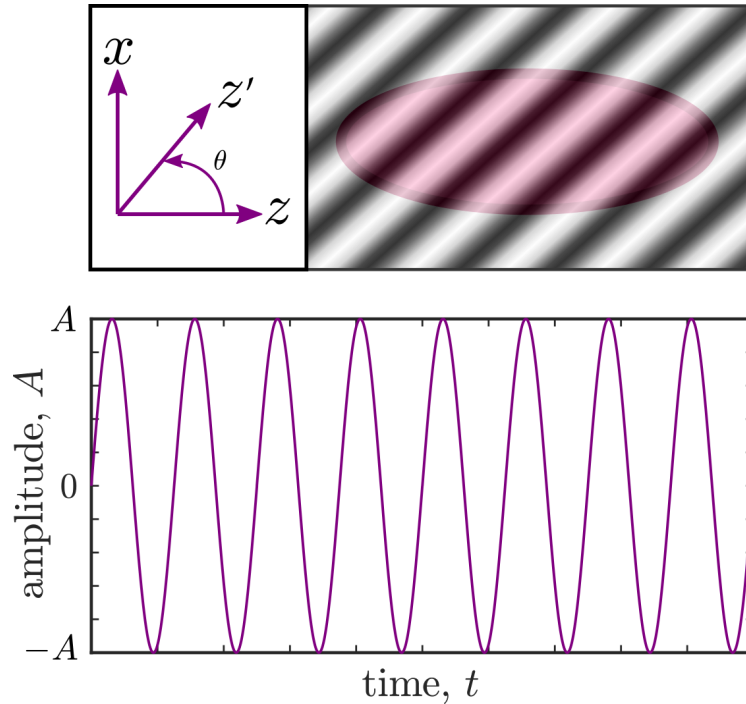
FIGURE 7.1: A simple sketch of the applied potential on a Thomas-Fermi profile.

a full study on every possible combination of parameters. We therefore set the time frequency of driving Ω_t, the width Ω_x, and the angle of driving, θ, and the number of cycles in the driving N_{cycle}. Although not presented here, we studied how the width of the driving affects the type of vortices formed. We found that a width too

small resulted in a lack of soliton (and thus vortex) creation and a width too large results in the warping of the condensate, as well as the appearance of oscillatory modes. There is a "goldilocks" zone of driving width of which one can get the largest number of solitons from avoiding as much as possible the subsequent concomitant of condensate warping. By trial and error, one finds this to be $\Omega_{z'} = 0.5$.

7.1.1 Frequency of driving

The time frequency of the driving must be in such a way that it is (obviously!) neither to quick or too slow. As such, we look at three different frequencies see see how it changes the driving. Figure 7.2 shows 2D density slices with $(1a, 1b, 1c, 1d)$ giving the results for $\Omega_t = 1$, $(2a, 2b, 2c, 2d)$ for $\Omega_t = 0.5$ and $(3a, 3b, 3c, 3d)$ showing $\Omega_t = 0.25$. Four different times are shown (the explanation is given in the figure caption) from the time $t = T_\Omega = 2\pi/\Omega$ until long after driving. For this test, we
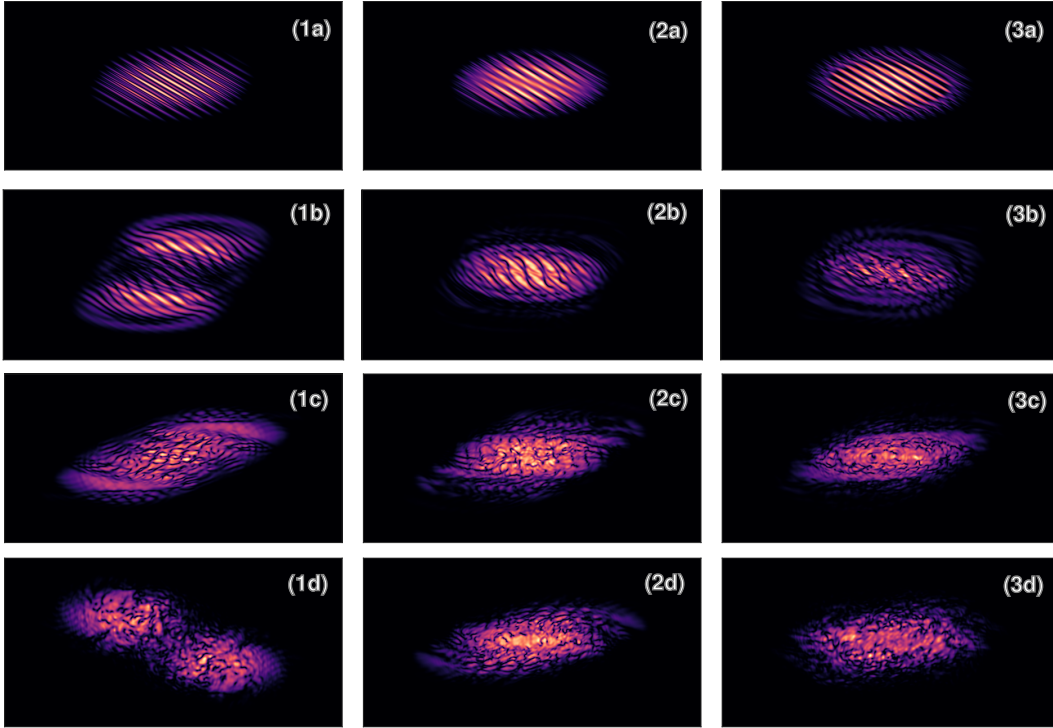
FIGURE 7.2: The 2D density slices, $n(x, y = 0, z)$ with $(1a, 1b, 1c, 1d)$ giving the results for $\Omega_t = 1$, $(2a, 2b, 2c, 2d)$ for $\Omega_t = 0.5$ and $(3a, 3b, 3c, 3d)$ showing $\Omega_t = 0.25$. For each simulation, $N_{cycle} = 1$. The different rows show the results at different time, $(1a, 2a, 3a)$ at $t = T_\Omega$, $(1b, 2b, 3b)$ at $t = T_\Omega + 20$, $(1c, 2c, 3c)$ at $t = T_\Omega + 50$ and $(1d, 2d, 3d, 4d)$ at $t = T_\Omega + 80$.

keep $A = 2$ and the condensate is driven at an angle of $\theta = 60°$. Immediately apparent is that the condensates shape is strongly affected when $\Omega_t = 1$. Although it (by sight alone) gives long vortices in the centre of the condensate (see Fig. 7.2(1c)), the warping of the overall condensate shape means any analytics will be difficult. The results for both $\Omega_t = 0.25$ and $\Omega_t = 0.5$ affect the condensate less but vortices are easily visible throughout the cloud. By monitoring the average location of the

vortices, the $\Omega_t = 0.5$ simulation gives a system with more vortices throughout the condensate bulk whereas the $\Omega_t = 0.25$ case (see Fig. 7.2 (3d)) has vortices around the edges, rather like the large scale driving in Chapter 6.

7.1.2 Angle of driving

We see in Fig. 7.3 that larger driving angles provide more overall vortex length. The t^{-1} decay is observable for all simulations, however lasts much longer for $\theta = 60$ and $80°$. We saw in Chapter 6 that the vortices formed in the large-scale driving are very small and consist mostly of loops. Analysis of the average vortex length
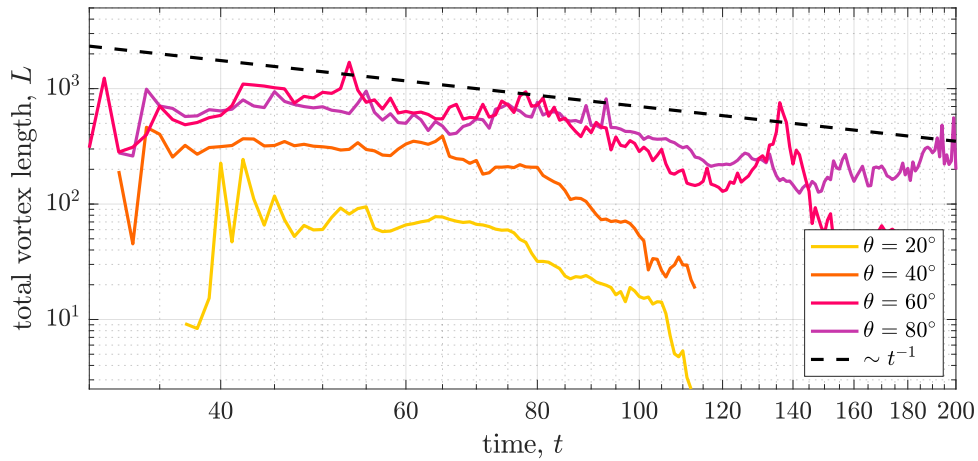
FIGURE 7.3: The total vortex length of the decay of the turbulence created in our tests cases; presented are different driving angles.

formed in the condensate reveals that the length of vortices in the larger θ cases create not just more overall vortex length, but that the length of the individual vortices increase at the driving angle increases; the average vortex length in the $\theta = 60°$ case is double that of $\theta = 20°$. It can be assumed that this is due to the initial bands across the condensate being longer for larger values of θ.

7.2 Expansion dynamics

We now investigate whether there is anything to be discerned from the expansion of our turbulent condensate. As said numerous times throughout this thesis, the expansion of a condensate, and measures done from the resulting images, remain a ubiquitous technique in experimental condensates. In Chapter 5, we never did see true self-similar expansion of condensates but saw a dramatic suppression of the aspect ratio while the cigar condensate expands. We also did not see the self-similar expansion in Chapter 6. We therefore give one last attempt at seeing if one observes self-similar expansion. We also look at measuring the momentum distribution of our turbulent condensates to see if one can gain a meaning from the power law of the momentum distribution of the expanding condensate. As a first test, we expand our test simulation. We release the driven condensate at $t_0 = 44$. Akin to the previous Chapters, we use our remeshing code to expand for a comparatively long

time. Presented in Fig. 7.4, we plot the aspect ratio, R_r/R_z, of a ground state condensate with the same harmonic trapping as the driven case ($\omega_{r,z} = \times[0.05, 0.02]$) (black line) for reference and plot the aspect ratio of the expanding turbulent state (red circles). We see here that the condensate does not invert for the time-span simulated. it does, however, not stay at exactly the same aspect ratio for the whole time; the ratio changes from 0.4 to 0.7. As in Section 6.3, we model the momentum distribution of the expanding condensate for this example case. We show the resultant 1D momentum distributions in Fig. 7.5 for different times of expansion, from $t = 40$ to $t = 140$. We can study how the exponent of the power law changes as we
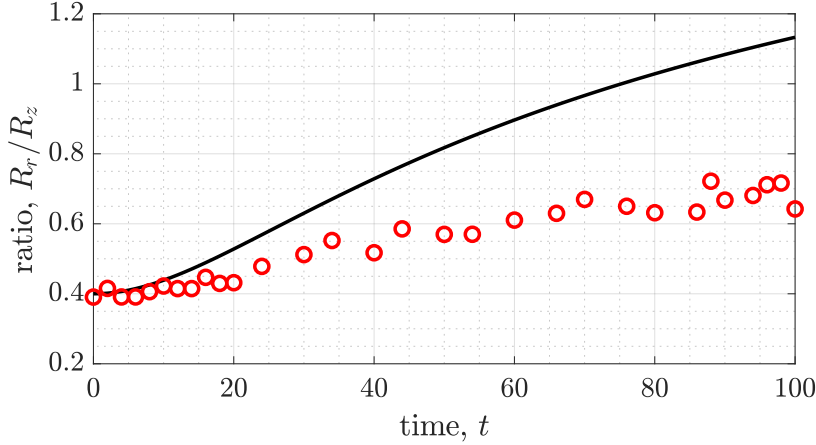
FIGURE 7.4: The change in aspect ratio R_r/R_z for an example ground state (black line) and our turbulent state (red circles) of the expanding condensate.

measure the spectra over different times, as shown in Fig. 7.6. When the expansion is small, the absolute value of the exponent of the momentum distribution is large but quickly diverges. From $t = 100$, the exponent of the momentum distribution, $n(k) \sim k^{-\alpha}$, settles with $\alpha = -2.88 \pm 0.05$. This shows that the given a large enough expansion, the momentum distribution can be obtained computationally with the Gross-Pitaevskii equation, as long as the time of expansion is sufficient. The scaling of $\alpha = -2.88$ is sufficiently close to that reported for wave turbulence. The 0.12 difference could occur due to a variety of reasons which need to be investigated - the presence of large-scale vortices, the inhomogenous nature of a harmonic condensate or the granulation of the driven condensate around the edges. One natural question is whether the scaling law we obtain is actually due to the presence of wave turbulence or whether it is a artefact of any condensate simply expanding, and whether the $\alpha = -2.88$ constant remains at any point of turbulent decay.

One quantification of the nature of vortex turbulence is the decay of the total vortex length - for our case here the total vortex length decays as t^{-1}.

The incompressible energy spectra also decays as the vortices begin to reconnect and lose length. We drive our condensate and let the simulation run long enough for the vortices to completely decay. At different times of the decay, we release the condensate and see how the scaling of the momentum distribution changes as a function of the time of release, t_0. In Fig. 7.7, we once again plot the $t_0 = 44$ line
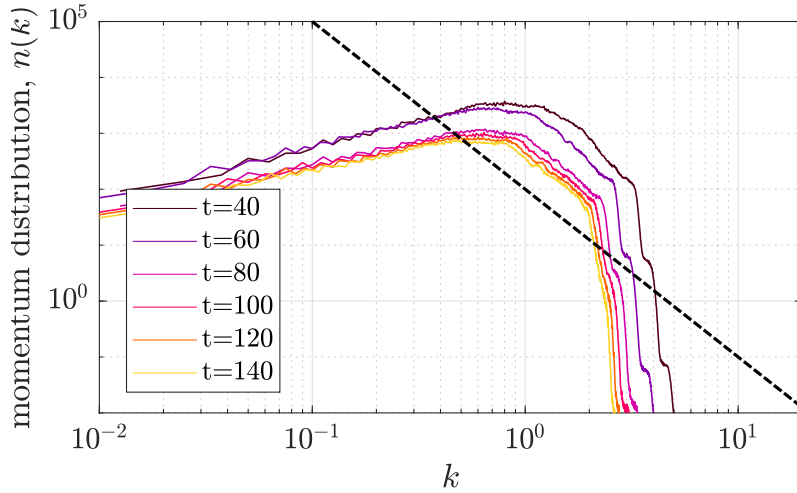
FIGURE 7.5: The momentum distribution of our example turbulent condensate, released at time t_0, with the distributions gained at times $t_0 + 40$ to $t_0 = 140$. Marked (black) is k^{-3} for reference.

from Fig. 7.5 alongside with the corresponding $t_0 + 80$ results for different t_0 values. Between $t_0 = 44$ and $t_0 = 60$, there is a noticeable shortening of the k^{-3} scale. It has almost disappeared by $t_0 = 80$ and is no longer distinguishable from $t_0 = 100$. It is worth pointing out here that depending on the drive given, the condensate can expand up to 15 times the original size of the condensate.

7.3 Generalisation of system

In the previous section, we focused on one specific parameter set for the driving; we briefly touched on the angle of driving but this was simply to see how the topology of the vortices changes as a function of angle before sticking to $\theta = 60°$. We see how there there is a noticeable t^{-1} scaling in the decay of the total vortex length. As the condensate expands further and further, the exponent tails towards a value (for our selected parameter, $\alpha = -2.88$). We also showed that for when we hold onto the condensate for longer and longer before expanding, the range of which the exponent is visible gets smaller and smaller until it is no longer visible. This is for a specific example and we therefore must look at a range of parameters to see how much of a range of disorder we can obtain using this proposed system. As stated many times in this thesis, we have access to the whole system whereas experimentalists have a very limited view on their condensates. One debate is that of what the exact mechanism which dictates the exponent formed in the momentum distribution. Another possible idea is to measure the correlation length from the time-of-flight image.

7.3.1 Dynamics of vortices

Earlier in this thesis, we discussed the idea of granulation and quantified it with a correlation length of the density; combining an averaged density around a point

Name	Maximum amplitude, A	Number of cycles, N
(1a)	0.25	1
(1b)	0.25	5
(1c)	0.25	10
(2a)	0.50	1
(2b)	0.50	5
(2c)	0.50	10
(3a)	1.00	1
(3b)	1.00	5
(3c)	1.00	10
(4a)	2.00	1
(4b)	2.00	5
(4c)	2.00	10
(5a)	5.00	1
(5b)	5.00	5
(5c)	5.00	10

TABLE 7.1: A list of simulations ran and the parameters used. For all simulations, $\theta = 60°$, $\Omega_x = 0.5$ and $\Omega_t = 0.5$.
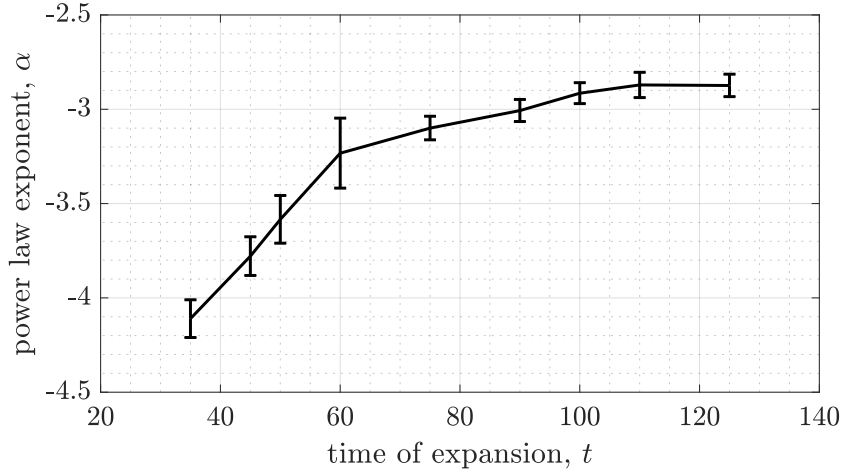
FIGURE 7.6: The exponent of the power law obtained from the expanding momentum distribution for the condensate released at $t_0 = 44$.

and the correlation helped distinguish between whether a phase defect in a system is an actual vortex or a subsequent of granulation of the condensate. In this new case, the granulation of the condensate is only on the outer extremities of the condensate so a much simpler method of vortex detection can be used for a wide array of parameter sets. We decide to study the location of vortices at locations within 70% of the calculated Thomas-Fermi profile of the system. Although there can indeed be vortices along the edges of the condensate, we decide to leave these out due to their co-existence with the granulation of the condensate bulk. We also reiterate that any vortices at the edge boundary of the condensate are arbitrary and contribute negligible energy compared to the ones in the condensate bulk. Akin to our previous work we aim to first see how the total vortex line length falls after the condensates have been driven. We see in Fig. 7.8 how the majority of simulations have a noticeable decay that one can quantify. When the driving amplitude and number of drives is low, the number of vortices formed are negligible and thus we denote these with "no vortices". This work is easier viewed in Table 7.2 where results are color-coded in order to see the clear domains. The term α simply denotes here the cases where a decay is indiscernible due to the lack of vortex line length created. The yellow section denotes areas of decay where $L \sim t^{-1.5}$, green where $L \sim t^{-1}$. Finally, the blue areas denoted by β, where the granulation of the condensate bulk makes any quantification of the decay constant unconvincing. We know from Chapter 2 that these two decay constants, $\alpha = -1.5$ and $\alpha = -1.0$ denote Kolmogorov and Vinen turbulence respectively.

As well as the decay laws, we also note the span of total vortex length detected for each parameter in Fig. 7.8. the total range of vortex lengths detected go from 1×10^2 to 5×10^4; this can be compared of a total maximum vortex length (in ξ) of roughly $L = 1 \times 10^3$ in the recreation of the Sao Paulo experiment in Chapter 6,
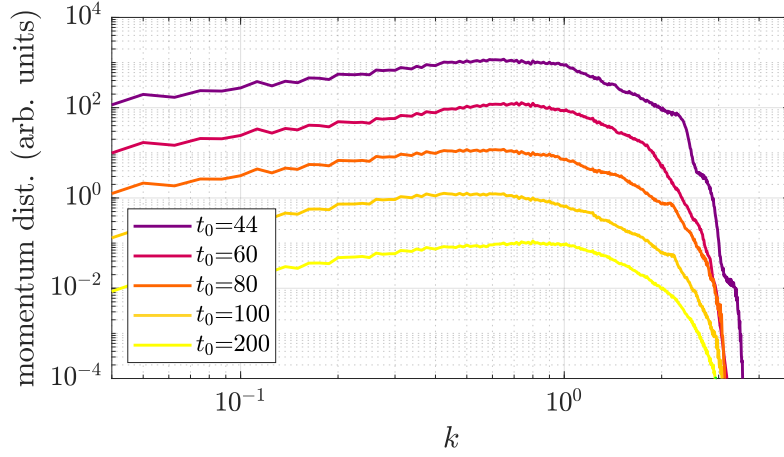
FIGURE 7.7: The momentum distribution of the expanding turbulent condensate, taken at a time $t = t_0 + 80$, where t_0 is the time of release from the harmonic potential. The distributions have been artificially shifted to make the results readable.
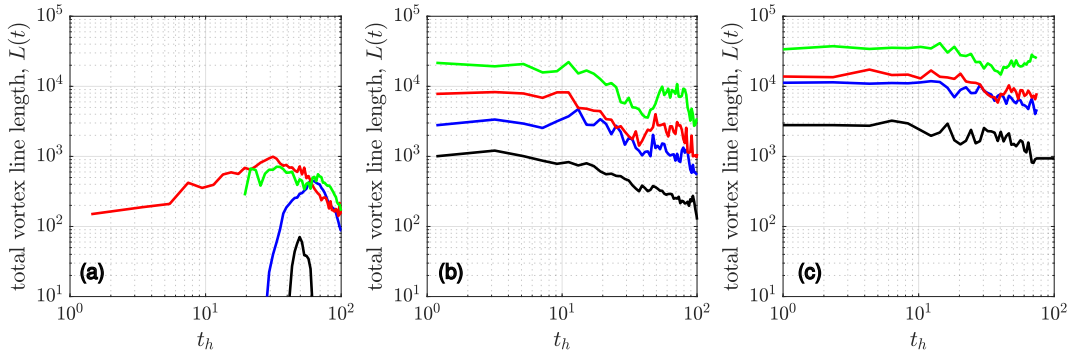
FIGURE 7.8: The decay of the total line length, L as the function of the hold time after driving $t_h = t - 2N\pi/\omega_t$ for (a) $N = 1$, (b) $N = 5$ and $N = 10$ for a system driven at $A = 0.25$ (black), $A = 0.50$ (blue), $A = 1.00$ (red) and $A = 2.00$ (green).

resulting in an improvement of up to roughly 50 times greater vortex length. Also quantifiable is the average vortex length of the system. While doing this, we negate all the vortices detected that have a length smaller than 5ξ. Unlike the detection of the exponent of the decay, the average length of the vortices detected is directly related to the amplitude and length of driving - the longer and harder the drive, the larger the average vortex length (see Fig. 7.9).

7.3.2 Momentum distribution

We end this thesis by seeing if one is able to quantify the nature of the turbulence by the exponent, $n(k) \sim k^{-\alpha}$, taken from the momentum distribution; we know how to quantify the disturbance within the condensate and thus wish to match these quantifications with the exponents measured to see if there is a trend. We do this by simply repeating what has been done earlier in the thesis - by allowing each simulation

	$A = 0.25$	$A = 0.50$	$A = 1.00$	$A = 2.00$	$A = 5.00$
$N = 1$	no vortices	no vortices	-1.18	-0.922	granulation
$N = 5$	-1.60	-1.10	-1.23	-1.142	granulation
$N = 10$	-1.66	-1.68	-1.56	granulation	granulation

TABLE 7.2: The term "no vortices" denotes a simulation of which no, or negligible vortices, are formed. The term "granulation" denotes a simulation where large granulation of the condensate resulted in difficulty obtaining an acceptable measurement of the decay of the total vortex line length.
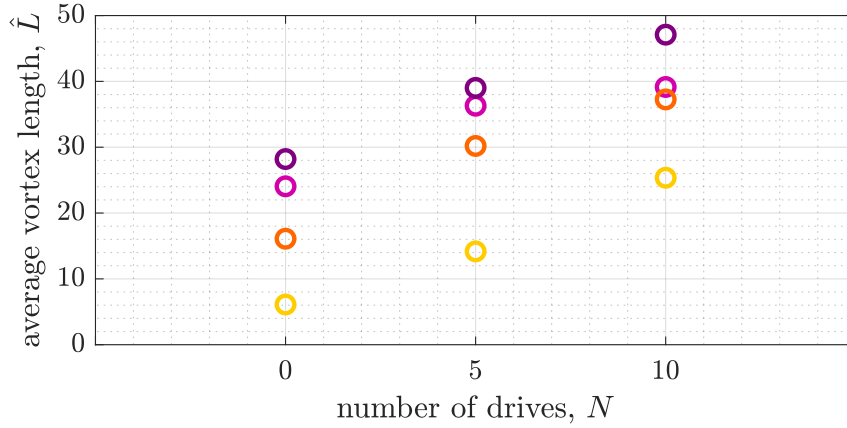
FIGURE 7.9: The average vortex length at a time corresponding to the peak total vortex length for simulations 1a, 1b and 1c (yellow), 2a, 2b, 2c (orange), 3a, 3b, 3c (pink) and 4a, 4b, 4c (purple).

to expand and measuring the exponent from the time-of-flight integrated image we receive; each simulation ran is listed in Tab. 7.1. The results are presented in Fig. 7.10 where the colour of the marker corresponds to the colour scheme denoted in Table 7.2. We note that three of the simulations failed; two of these corresponded to simulations (5b) and (5c): the simulations expanded at such a rate that the simulation collided with the edges of the computational domain before the simulation reached its end. The last missing simulation is (1a), this simulation simply did not give a detectable power law (due to a lack of turbulence). The results obtained tell something interesting: the result giving the steepest law was simulation (5a), where A=5.00. This lead to a wildly fragmented state. In the integrated plane, it can be assumed that this gives the closest result to a weak wave turbulent state. Also noticeable is that the simulations corresponding to a Kolmogorov vortex decay has a much smaller scaling law compared to those simulations corresponding to a Vinen turbulent state.

7.4 Conclusion

In this Chapter we presented an experimentally viable method to create turbulence within a condensate. Using a DMD, one would be able to drive a condensate to turbulence and image the result. Here, we showed that non-negligible vortices are created and that we can discern that most simulations we ran end in a turbulent
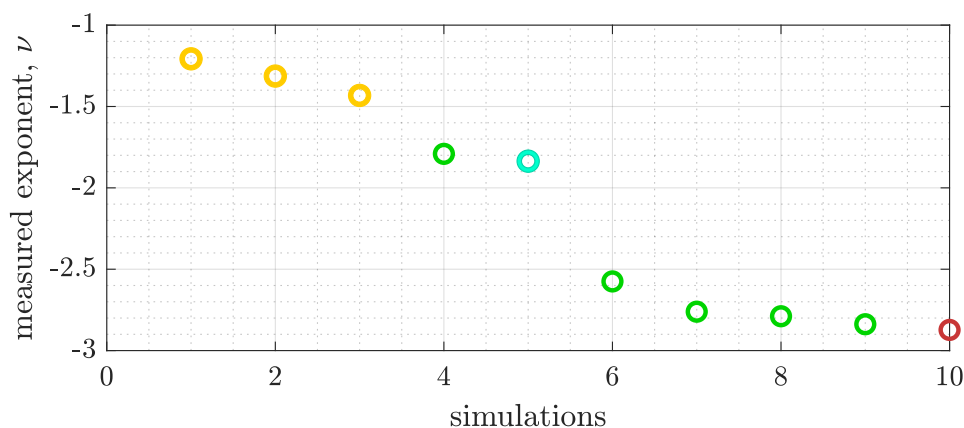
FIGURE 7.10: The measured exponents for the different simulations,
with colours referencing the colour scheme in Table 7.2

state. By choosing the parameters of the driving, it is believed that one can, to some extent, alter and manufacture the type of turbulence in their experimental setup.

One must strongly warn the reader that the work presented in the expansion work is not claimed to be a universal law. The condensates this work was based off is a harmonically trapped condensate in a cigar shape. To run these 12 simulations was extremely computationally intensive, both in CPU hours and in storage. It was therefore not feasible at the time of writing to also be able to explore different condensate shapes or even investigate how the exponent of the momentum distribution changes when one changes other parameters kept the same in this chapter (i.e., the angle and frequency of driving). We also did not take into affect the quantification of the density fluctuations (i.e., the density correlation), and it is certainly possible that these have a big role to play in the measured correlation. Ideally, extra work must be done to explore the parameter regime - the goal is to achieve a condensate with the largest number of, and longest vortices. Here, one must optimise the parameters to obtain the largest ratio of the incompressible to compressible energy in the condensate.

Nevertheless, even with such caveats, we have shown that it may indeed be possible to categorise the disorder in a given experimental image alone, or at least give a strong indication to such a reading.

8 Conclusions and Further Work

In this thesis we have carried out a computational study of turbulence within a Bose-Einstein condensate. This work can be seen as twofold; the modelling of time-of-flight experiments and the creation of turbulence within a condensate. We combine these two works to then study experimentally viable measurements. We have developed a workable solution to model the expansion of condensates; this ensured that one can model the expansion of condensates to the scale of experiments. Here, we have computationally verified analytical solutions regarding how vortex tangles affect the expansion of condensates and discussed the different ways one can produce analytical predictions. Interesting in itself, it has also meant that we can make useful measurements for our later work and can model how experimentalists take the exponent for the experimental momentum distribution. We found good agreement between the estimates given by an expanding condensate and the analyical predictions on how vortices effect the expansion of a condensate.

In Chapter 6 we provided the first full computational modelling of the driving of condensates to turbulence using experimentally viable means. Here, we concluded that the turbulence created is not what was expected - as in, that is was not Kolmogorov turbulence. Although clearly turbulent in nature, the topology of the vortices created give rise to a new turbulent range not previously predicted in literature. We showed that various measurements are similar to that of stereotypical Vinen turbulence in quantum fluids. There are, however, differences, which are due to the typical shape of the vortices.

In our final chapter we proposed a method to create turbulence in an experimentally achievable manner. Here, we were able to show that one can indeed drive a condensate to turbulence without bringing about the large dipole mode brought on by the large scale driving in Chapter 6. Here, we showed evidence to say that we can create larger scale vortices than in the large-scale diving case and that some simulations showed evidence of a Kolmogorov vortex decay whereas some showed evidence of a Vinen type of decay. We finally showed that a wide range of momentum distribution can be measured from such an experiment.

There is a vast array of further work that can be investigated from the work concluded in this thesis:

The method of a remeshable computational grid was a success for our harmonically trapped condensates. Although not reported in the main thesis, trying to model the expansion of a homogeneous, box-trapped condensate failed. Unlike in the harmonically trapped cases, there is no analytical prediction to the change of the shape of the condensate during expansion. In tests, the expanding ground state can have such sharp fluctuations that remeshing onto a less line grid can cause errors and artificial noise which will break the simulation. If one wishes to model the expansion of a hard-wall condensate, one will have to develop a new system. It is worth pointing out that no analytical study on the expansion of box-trapped

condensate exists at the time of writing.

The biggest problem we encountered in the modelling of the Sao Paulo experiment was the large dipole mode. Upon testing different methods of damping, it was found that the behaviour of the condensate changed completely changed depending on how one implemented the damping. If, for example, one used a spatially independant low damping everywhere in the system, the dipole mode would indeed die out but the dark soliton formation that seeds the vortex creation did not occur. If one attempted to mimic a thermal cloud (which will sit around the edges of the condensate) using a spatially dependant damping, then the result was completely dependant on how it defines such a damping (and thus shouldnt be used). If one therefore wishes to model a spatially driven condensate and neglect the dipole mode, it was concluded that one must use a coupled system where one simulates both the condensate and the thermal cloud. Here, Zaremba, Nikuni, and Griffin (ZNG) formalism can be employed [191], where a GPE equation is coupled with the semiclassical Boltzmann equation which models the corresponding thermal cloud of the system. Oscillatory modes are often used experimentally to detect the temperature of the system, as they are widely affected by the temperature of the system and the thermal cloud. The ZNG approach to modelling condensates has been successfully used to model this oscillations so seem to be the best method to describe any extra physics provided by the interaction of a condensate and thermal cloud. It also would mean the decay of the dipole mode, which would provide a larger timescale in which one could study the system.

This work on the driven system and the code developed is also in use by a Masters student in the study of how condensates can be used as a Ramsey Interferometer.

The majority of open questions are without a doubt come from the work in Chapter 7. Of paramount importance is the verification of momentum distribution obtained through experimental means. There have been claims of shifting of scaling when one goes from a measurement from a 3D to a 2D system. In our cases, we measured a change of 0.2 in the scaling exponent. Bold claims have been made in the determination of the type of turbulence from the experimental image, and detected scaling exponent, but conclusive evidence has yet to be provided to link an exponent and the nature of the disorder inside the condensate. We have presented the start of a work that can investigate such a link. Using our tuneable method, one can look at a range of level of disorder from small density fluctuations, our strong turbulence of small vortex rings and large density fluctuations, to vortex turbulence, to fragmentation. Modelling the expansion one could then see how the exponent gained from TOF images changes accordingly. Ideally, one would be able to obtain a Kolmogorov system with a large number of very long vortices from the same driving technique; for all the turbulent states created, the total vortex length was relatively small. It must be stated that this isn't inherently due to the technique but the shape of the condensate; the Thomas-Fermi radius in the radial direction was 28, or roughly on the order of the average vortex length shown in Fig. 7.9. We had to chose a condensate of a smaller size so that the simulation of the expansion was also workable. Although not included in this thesis, we did investigate the use of passing grids through a condensate; this work gave a very similar to that of Helium system. As discussed in our Background chapter, grids are the archetypal method of inducing Kolmogorov turbulence into both classical fluids and liquid Helium.

Indeed - some classical fluids texts use the terms "grid" and "Kolmogorov" interchangeably when discussing turbulence. We note that it might simply be that it is not achievable to make large scale Kolmogorov turbulence experimentally in a condensate. The healing length in Helium is decades smaller than the width of the grid, both of which are decades and decades smaller than the total size of the experimental container. At the time of writing this thesis, the width of trapped condensates are typically only a decade larger than the healing length of the condensate. It may be that one has to wait until very large condensates can be created in a laboratory to finally observe Kolmogorov turbulence in an experimental condensate.

Branching out to further questions, it is also imperative to understand the combination and interplay between wave turbulence and vortices. In this thesis we focused more on the effect of vortices and how the turbulence changes depending on their topological nature, and were not able to fully delve into wave turbulence. There are questions that remain unanswered;

- A typical wave-turbulence is studied in a homogeneous system with small perturbations. These systems are solvable analytically. What, therefore, is the effect of a varying background density?

- In what limit can we study wave-turbulence with the GPE? Are we able to resolve the range from the small density fluctuations to the beginnings of fragmentation in the density?

- Kelvin waves on a quantised vortex [91] are predicted to be fundamental in the final stages of decay of vortex turbulence [192]. How is this regime affected by the topology of the vortex?; if the vortices one creates in strong turbulence are typically much smaller than that of typical Vinen turbulence, what does this mean for this "Kelvin wave" regime?

- Related to this, how does the short length of the vortex rings affect the final stage? If there is a limit on the wavelength of the allowed Kelvin waves, how does this change the final stage mechanism?

It must be stated that the author has most likely missed many other interesting questions; any list would, without a doubt, be incomplete.

Bibliography

[1] Plutarch. *Lives. Volume V / Plutarch.* eng. 1917.

[2] A. Colagrossi et al. "Da Vinci's observation of turbulence: A French-Italian study aiming at numerically reproducing the physics behind one of his drawings, 500 years later". In: *Phys. Fluids* 33.11 (2021).

[3] P. A. Davidson. *Turbulence: an introduction for scientists and engineers.* Oxford university press, 2015.

[4] R. P. Feynman. *The Feynman lectures on physics.* eng. 1963.

[5] Stringari. S. Pitaevskiĭ L. P. *Bose-Einstein condensation and superfluidity.* International Series of Monographs on Physics. 2016. ISBN: 0-19-181872-0.

[6] C. J. Pethick and H. Smith. *Bose–Einstein condensation in dilute gases.* Cambridge university press, 2008.

[7] E. A. L. Henn et al. "Emergence of Turbulence in an Oscillating Bose-Einstein Condensate". In: *Phys. Rev. Lett.* 103 (4 2009), p. 045301.

[8] K. J. Thompson et al. "Evidence of power law behavior in the momentum distribution of a turbulent trapped Bose–Einstein condensate". In: *Laser Phys. Lett.* 11.1 (2013), p. 015501.

[9] A. D. García-Orozco et al. "Universal dynamics of a turbulent superfluid Bose gas". In: *Phys. Rev. A* 106.2 (2022), p. 023314.

[10] A. L. Gaunt et al. "Bose-Einstein Condensation of Atoms in a Uniform Potential". In: *Phys. Rev. Lett.* 110 (20 2013), p. 200406.

[11] N. Navon et al. "Emergence of a turbulent cascade in a quantum gas". In: *Nature* 539.7627 (2016), pp. 72–75.

[12] Lena H Dogra et al. "Universal equation of state for wave turbulence in a quantum gas". In: *Nature* 620.7974 (2023), pp. 521–524.

[13] H. A. J. Middleton-Spencer et al. "Characterising arbitrary dark solitons in trapped one-dimensional Bose-Einstein condensates (a)". In: *EPL* 133.1 (2021), p. 16001.

[14] C. F. Barenghi et al. "Types of quantum turbulence". In: *AVS Quantum Science* 5.2 (2023).

[15] H. A. J. Middleton-Spencer et al. "Evidence of Strong Quantum Turbulence in Bose Einstein Condensates". In: *arXiv preprint arXiv:2204.08544* (2022).

[16] L. D. Landau and E. M. Lifshitz. *Statistical Physics: Volume 5.* Vol. 5. Elsevier, 2013.

[17] V. S. Bagnato, D. E. Pritchard, and D. Kleppner. "Bose-Einstein condensation in an external potential". In: *Phys. Rev. A* 35 (10 1987), pp. 4354–4358.

[18] E. P. Gross. "Structure of a quantized vortex in boson systems". In: *Il Nuovo Cimento (1955-1965)* 20.3 (1961), pp. 454–477.

[19] L. P. Pitaevskii. "Vortex lines in an imperfect Bose gas". In: *Sov. Phys. JETP* 13.2 (1961), pp. 451–454.

[20] M. C Tsatsos et al. "Quantum turbulence in trapped atomic Bose–Einstein condensates". In: *Phys. Rep.* 622 (2016), pp. 1–52.

[21] D. J. Frantzeskakis. "Dark solitons in atomic Bose–Einstein condensates: from theory to experiments". In: *J. Phys. A* 43.21 (2010), p. 213001.

[22] V. E. Zakharov and A. B Shabat. "Interaction between solitons in a stable medium". In: *Sov. Phys. JETP* 37.5 (1973), pp. 823–828.

[23] Th. Busch and J. R. Anglin. "Motion of Dark Solitons in Trapped Bose-Einstein Condensates". In: *Phys. Rev. Lett.* 84 (11 2000), pp. 2298–2301.

[24] M. Sciacca, C. F. Barenghi, and N. G. Parker. "Matter-wave dark solitons in boxlike traps". In: *Phys. Rev. A* 95 (1 2017), p. 013628.

[25] N. G. Parker et al. "Soliton-sound interactions in quasi-one-dimensional Bose-Einstein condensates". In: *Phys. Rev. Lett.* 90.22 (2003), p. 220401.

[26] N. G. Parker, N. P. Proukakis, and C. S. Adams. "Dark soliton decay due to trap anharmonicity in atomic Bose-Einstein condensates". In: *Phys. Rev. A* 81 (3 2010), p. 033606.

[27] B. Jackson, N. P. Proukakis, and C. F. Barenghi. "Dark-soliton dynamics in Bose-Einstein condensates at finite temperature". In: *Phys. Rev. A* 75 (5 2007), p. 051601.

[28] L. D. Carr et al. "Dark-soliton creation in Bose-Einstein condensates". In: *Phys. Rev. A* 63.5 (2001), p. 051601.

[29] A. R. Fritsch et al. "Creating solitons with controllable and near-zero velocity in Bose-Einstein condensates". In: *Phys. Rev. A* 101.5 (2020), p. 053629.

[30] S. Burger et al. "Dark Solitons in Bose-Einstein Condensates". In: *Phys. Rev. Lett.* 83 (25 1999), pp. 5198–5201.

[31] J Denschlag et al. "Generating solitons by phase engineering of a Bose-Einstein condensate". In: *Science* 287.5450 (2000), pp. 97–101.

[32] B. P. Anderson et al. "Watching Dark Solitons Decay into Vortex Rings in a Bose-Einstein Condensate". In: *Phys. Rev. Lett.* 86 (14 2001), pp. 2926–2929.

[33] Y. Kawaguchi and T. Ohmi. "Splitting instability of a multiply charged vortex in a Bose-Einstein condensate". In: *Phys. Rev. A* 70 (4 Oct. 2004), p. 043610.

[34] P. G. Kevrekidis, D. J. Frantzeskakis, and R. Carretero-González. *Emergent nonlinear phenomena in Bose-Einstein condensates: theory and experiment*. Vol. 45. Springer, 2008.

[35] K.-P. Marzlin, W. Zhang, and E. M. Wright. "Vortex Coupler for Atomic Bose-Einstein Condensates". In: *Phys. Rev. Lett.* 79 (24 1997), pp. 4728–4731.

[36] E. L. Bolda and D. F. Walls. "Creation of vortices in a Bose-Einstein condensate by a Raman technique". In: *Phys. Lett. A.* 246.1-2 (1998), pp. 32–36.

[37]   R. Dum et al. "Creation of Dark Solitons and Vortices in Bose-Einstein Condensates". In: *Phys. Rev. Lett.* 80 (14 1998), pp. 2972–2975.

[38]   J. E. Williams and M. J. Holland. "Preparing topological states of a Bose–Einstein condensate". In: *Nature* 401.6753 (1999), pp. 568–572.

[39]   M. R. Matthews et al. "Vortices in a Bose-Einstein condensate". In: *Phys. Rev. Lett.* 83.13 (1999), p. 2498.

[40]   A. E. Leanhardt et al. "Imprinting Vortices in a Bose-Einstein Condensate using Topological Phases". In: *Phys. Rev. Lett.* 89 (19 2002), p. 190403.

[41]   E. A. L. Henn et al. "Observation of vortex formation in an oscillating trapped Bose–Einstein condensate". In: *Phys. Rev. A* 79 (4 2009), p. 043618.

[42]   D. R. Scherer et al. "Vortex Formation by Merging of Multiple Trapped Bose-Einstein Condensates". In: *Phys. Rev. Lett.* 98 (11 2007), p. 110402.

[43]   M. W. Zwierlein et al. "Vortices and superfluidity in a strongly interacting Fermi gas". In: *Nature* 435.7045 (2005), pp. 1047–1051.

[44]   S. Nazarenko and R. West. "Analytical solution for nonlinear Schrödinger vortex reconnection". In: *J. Low Temp. Phys.* 132.1 (2003), pp. 1–10.

[45]   A. T. A. M. De Waele and R. G. K. M. Aarts. "Route to vortex reconnection". In: *Phys. Rev. Lett.* 72.4 (1994), p. 482.

[46]   M. S. Paoletti, M. E. Fisher, and D. P. Lathrop. "Reconnection dynamics for quantized vortices". In: *Physica D: Nonlinear Phenomena* 239.14 (2010), pp. 1367–1377.

[47]   R. Tebbs, A. J. Youd, and C. F. Barenghi. "The approach to vortex reconnection". In: *J. Low Temp. Phys.* 162.3 (2011), pp. 314–321.

[48]   A. Villois, D. Proment, and G. Krstulovic. "Universal and nonuniversal aspects of vortex reconnections in superfluids". In: *Phys. Rev. Fluids* 2.4 (2017), p. 044701.

[49]   S. Zuccher et al. "Quantum vortex reconnections". In: *Phys. Fluids* 24.12 (2012), p. 125108.

[50]   A. J. Allen et al. "Vortex reconnections in atomic condensates at finite temperature". In: *Phys. Rev. A* 90.1 (2014), p. 013601.

[51]   C. Rorai et al. "Approach and separation of quantised vortices with balanced cores". In: *J. Fluid Mech.* 808 (2016), pp. 641–667.

[52]   E. Fonda, K. R. Sreenivasan, and D. P. Lathrop. "Reconnection scaling in quantum fluids". In: *Proc. Natl. Acad. Sci. U.S.A.* 116.6 (2019), pp. 1924–1928.

[53]   T. Lipniacki. "Evolution of quantum vortices following reconnection". In: *European Journal of Mechanics-B/Fluids* 19.3 (2000), pp. 361–378.

[54]   L. Galantucci et al. "Crossover from interaction to driven regimes in quantum vortex reconnections". In: *Proc. Natl. Acad. Sci. U.S.A.* 116.25 (2019), pp. 12204–12211.

[55]   A. Villois, D. Proment, and G. Krstulovic. "Irreversible dynamics of vortex reconnections in quantum fluids". In: *Phys. Rev. Lett.* 125.16 (2020), p. 164501.

[56]   L. D. Landau and E. M. Lifshitz. *Fluid Mechanics: Landau and Lifshitz: Course of Theoretical Physics, Volume 6*. Vol. 6. Elsevier, 2013.

[57]   K. R. Sreenivasan. "On the universality of the Kolmogorov constant". In: *Physics of Fluids* 7.11 (1995), pp. 2778–2784.

[58]   S. R. Stalp, L. Skrbek, and R. J. Donnelly. "Decay of Grid Turbulence in a Finite Channel". In: *Phys. Rev. Lett.* 82 (24 1999), pp. 4831–4834.

[59]   W. F. Vinen and J. J. Niemela. "Quantum turbulence". In: *J. Low Temp. Phys* 128 (2002), pp. 167–231.

[60]   R. Hänninen and A. W. Baggaley. "Vortex filament method as a tool for computational visualization of quantum turbulence". In: *Proc. Natl. Acad. Sci. U.S.A.* 111.supplement_1 (2014), pp. 4667–4674.

[61]   J. Maurer and P. Tabeling. "Local investigation of superfluid turbulence". In: *EPL* 43.1 (1998), p. 29.

[62]   J. Salort et al. "Experimental signature of quantum turbulence in velocity spectra?" In: *New J. Phys.* 23.6 (2021), p. 063005.

[63]   M. R. Smith et al. "Decay of vorticity in homogeneous turbulence". In: *Phys. Rev. Lett.* 71.16 (1993), p. 2583.

[64]   D. E. Zmeev et al. "Dissipation of Quasiclassical Turbulence in Superfluid ^{4}He". In: *Phys. Rev. Lett.* 115 (15 2015), p. 155303.

[65]   J. Salort et al. "Turbulent velocity spectra in superfluid flows". In: *Phys. Fluids* 22.12 (2010), p. 125102.

[66]   B. Rousset et al. "Superfluid high REynolds von Kármán experiment". In: *Rev. Sci. Instrum.* 85.10 (2014), p. 103908.

[67]   M. S. Paoletti et al. "Velocity statistics distinguish quantum turbulence from classical turbulence". In: *Phys. Rev. Lett.* 101.15 (2008), p. 154501.

[68]   M. Farge, G. Pellegrino, and K. Schneider. "Coherent vortex extraction in 3D turbulent flows using orthogonal wavelets". In: *Phys. Rev. Lett.* 87.5 (2001), p. 054501.

[69]   A. W. Baggaley, J. Laurie, and C. F. Barenghi. "Vortex-density fluctuations, energy spectra, and vortical regions in superfluid turbulence". In: *Physical Rev. Lett.* 109.20 (2012), p. 205304.

[70]   A. W. Baggaley. "The importance of vortex bundles in quantum turbulence at absolute zero". In: *Phys. Fluids* 24.5 (2012), p. 055109.

[71]   J. I. Polanco, N. P. Müller, and G. Krstulovic. "Vortex clustering, polarisation and circulation intermittency in classical and quantum turbulence". In: *Nat. Commun.* 12.1 (2021), pp. 1–11.

[72]   P.-E Roche and C. F Barenghi. "Vortex spectrum in superfluid turbulence: Interpretation of a recent experiment". In: *EPL* 81.3 (2008), p. 36002.

[73]   P. M. Walmsley et al. "Dissipation of quantum turbulence in the zero temperature limit". In: *Phys. Rev. Lett.* 99.26 (2007), p. 265302.

[74]   D. I. Bradley et al. "Decay of Pure Quantum Turbulence in Superfluid He 3-B". In: *Phys. Rev. Lett.* 96.3 (2006), p. 035301.

[75] A. W. Baggaley et al. "Visualizing Pure Quantum Turbulence in Superfluid He 3: Andreev Reflection and its Spectral Properties". In: *Phys. Rev. Lett.* 115.1 (2015), p. 015302.

[76] P. M. Walmsley and A. I. Golov. "Quantum and quasiclassical types of superfluid turbulence". In: *Phys. Rev. Lett.* 100.24 (2008), p. 245301.

[77] W. F. Vinen. "Mutual friction in a heat current in liquid helium II. II. Experiments on transient effects". In: *Proc. R. Soc. A* 240.1220 (1957), pp. 128–143.

[78] W. F. Vinen. "Mutual friction in a heat current in liquid helium II III. Theory of the mutual friction". In: *Proc. R. Soc. A* 242.1231 (1957), pp. 493–515.

[79] W. F. Vinen. "Mutual friction in a heat current in liquid helium II I. Experiments on steady heat currents". In: *Proc. R. Soc. A* 240.1220 (1957), pp. 114–127.

[80] G. E. Volovik. "Classical and quantum regimes of superfluid turbulence". In: *J. Exp. Theor. Phys. Lett.* 78.9 (2003), pp. 533–537.

[81] G. E. Volovik. "On developed superfluid turbulence". In: *J. Low Temp. Phys.* 136.5 (2004), pp. 309–327.

[82] V. S. L'vov, V. Nazarenko, and G. E Volovik. "Energy spectra of developed superfluid turbulence". In: *J. Exp. Theor. Phys. Lett.* 80.7 (2004), pp. 479–483.

[83] A. Cidrim et al. "Vinen turbulence via the decay of multicharged vortices in trapped atomic Bose–Einstein condensates". In: *Phys. Rev. A* 96 (2 2017), p. 023617.

[84] G. W. Stagg, N. G. Parker, and C. F. Barenghi. "Ultraquantum turbulence in a quenched homogeneous Bose gas". In: *Phys. Rev. A* 94 (5 2016), p. 053632.

[85] P. M. Walmsley and A. I. Golov. "Coexistence of quantum and classical flows in quantum turbulence in the t= 0 limit". In: *Phys. Rev. Lett.* 118.13 (2017), p. 134501.

[86] P. M. Walmsley and A. I. Golov. "Quantum and Quasiclassical Types of Superfluid Turbulence". In: *Phys. Rev. Lett.* 100 (24 2008), p. 245301.

[87] A. W. Baggaley, C. F. Barenghi, and Y. A. Sergeev. "Quasiclassical and ultraquantum decay of superfluid turbulence". In: *Phys. Rev. B* 85.6 (2012).

[88] P. Caillol and V. Zeitlin. "Kinetic equations and stationary energy spectra of weakly nonlinear internal gravity waves". In: *Dynamics of atmospheres and oceans* 32.2 (2000), pp. 81–112.

[89] T. W. B. Kibble. "Topology of cosmic domains and strings". In: *J. Phys. A* 9.8 (1976), p. 1387.

[90] Evgeny Kozik and Boris Svistunov. "Kelvin-wave cascade and decay of superfluid turbulence". In: *Physical review letters* 92.3 (2004), p. 035301.

[91] German V Kolmakov, Peter Vaughan Elsmere McClintock, and Sergey V Nazarenko. "Wave turbulence in quantum fluids". In: *Proceedings of the National Academy of Sciences* 111.supplement_1 (2014), pp. 4727–4734.

[92] T. W. Hänsch and A. L. Schawlow. "Cooling of gases by laser radiation". In: *Opt. Commun.* 13.1 (1975), pp. 68–69.

[93] S. Chu et al. "Experimental Observation of Optically Trapped Atoms". In: *Phys. Rev. Lett.* 57 (3 1986), pp. 314–317.

[94] C. J. Foot. *Atomic physics*. Vol. 7. OUP Oxford, 2004.

[95] G. Gauthier et al. "Direct imaging of a digital-micromirror device for configurable microscopic optical potentials". In: *Optica* 3.10 (2016), pp. 1136–1143.

[96] M. Kobayashi and M. Tsubota. "Quantum turbulence in a trapped Bose-Einstein condensate". In: *Phys. Rev. A* 76.4 (2007), p. 045603.

[97] J. A. S. Harutinian. "Study of excitations in a Bose-Einstein condensate". PhD thesis. Universidade de São Paulo, 2011.

[98] V. I. Yukalov, E. P. Yukalova, and V. S. Bagnato. "Bose systems in spatially random or time-varying potentials". In: *Laser Phys.* 19.4 (2009), pp. 686–699.

[99] K. E. Wilson et al. "In situ imaging of vortices in Bose-Einstein condensates". In: *Phys. Rev. A* 91 (2 2015), p. 023621.

[100] S. W. Seo et al. "Observation of vortex-antivortex pairing in decaying 2D turbulence of a superfluid gas". In: *Sci. Rep.* 7.1 (2017), pp. 1–8.

[101] S. Serafini et al. "Vortex Reconnections and Rebounds in Trapped Atomic Bose-Einstein Condensates". In: *Phys. Rev. X* 7 (2 2017), p. 021031.

[102] *Github Repository*. https://github.com/georgestagg/3D-GP-MPIOMP. Accessed: 2022-02-28.

[103] C. R. Taylor. *Finite Difference Coefficients Calculator*. https://web.media.mit.edu/~crtaylor/calculator.html. 2016.

[104] N. G. Berloff. "Padé approximations of solitary wave solutions of the Gross–Pitaevskii equation". In: *J. Phys. A* 37.5 (2004), p. 1617.

[105] A. Villois et al. "A vortex filament tracking method for the gross–pitaevskii model of a superfluid". In: *J. Phys. A* 49.41 (2016), p. 415502.

[106] P. Alliez et al. "Recent advances in remeshing of surfaces". In: *Shape analysis and structuring* (2008), pp. 53–82.

[107] A. Magni and G.-H. Cottet. "Accurate, non-oscillatory, remeshing schemes for particle methods". In: *J. of Comput. Phys.* 231.1 (2012), pp. 152–172.

[108] T. Plewa and E. Mueller. "AMRA: An Adaptive Mesh Refinement hydrodynamic code for astrophysics". In: *Comput. Phys. Commun* 138.2 (2001), pp. 101–127.

[109] Laurent Debreu, Christophe Vouland, and Eric Blayo. "AGRIF: Adaptive grid refinement in Fortran". In: *Comput. Geosci* 34.1 (2008), pp. 8–13.

[110] Yu. S. Kivshar and B. Luther-Davies. "Dark optical solitons: physics and applications". In: *Phys. Rep.* 298.2-3 (1998), pp. 81–197.

[111] Yu. S. Kivshar. "On the soliton generation in optical fibres". In: *J. Phys. A:* 22.3 (1989), p. 337.

[112] B. Kibler et al. "The Peregrine soliton in nonlinear fibre optics". In: *Nat. Phys.* 6.10 (2010), pp. 790–795.

[113] M. Chen et al. "Microwave magnetic-envelope dark solitons in yttrium iron garnet thin films". In: *Phys. Rev. Lett.* 70.11 (1993), p. 1707.

[114] A. V. Drozdovskii et al. "Formation of envelope solitons of spin-wave packets propagating in thin-film magnon crystals". In: *JETP Lett.* 91.1 (2010), pp. 16–20.

[115] R. Camassa and D. D. Holm. "An integrable shallow water equation with peaked solitons". In: *Phys. Rev. Lett.* 71.11 (1993), p. 1661.

[116] Y. Kodama. "KP solitons in shallow water". In: *J. Phys. A* 43.43 (2010), p. 434004.

[117] A. Chabchoub et al. "Experimental Observation of Dark Solitons on the Surface of Water". In: *Phys. Rev. Lett.* 110 (12 2013), p. 124101.

[118] Z. Dutton et al. "Observation of quantum shock waves created with ultra-compressed slow light pulses in a Bose-Einstein condensate". In: *Science* 293.5530 (2001), pp. 663–668.

[119] G.-B. Jo et al. "Phase-Sensitive Recombination of Two Bose-Einstein Condensates on an Atom Chip". In: *Phys. Rev. Lett.* 98 (18 2007), p. 180401.

[120] P. Engels and C. Atherton. "Stationary and Nonstationary Fluid Flow of a Bose-Einstein Condensate Through a Penetrable Barrier". In: *Phys. Rev. Lett.* 99 (16 2007), p. 160405.

[121] C. Becker et al. "Oscillations and interactions of dark and dark–bright solitons in Bose–Einstein condensates". In: *Nat. Phys.* 4.6 (2008), pp. 496–501.

[122] J. J. Chang, P. Engels, and M. A. Hoefer. "Formation of Dispersive Shock Waves by Merging and Splitting Bose-Einstein Condensates". In: *Phys. Rev. Lett.* 101 (17 2008), p. 170404.

[123] S. Stellmer et al. "Collisions of Dark Solitons in Elongated Bose-Einstein Condensates". In: *Phys. Rev. Lett.* 101 (12 2008), p. 120406.

[124] A. Weller et al. "Experimental Observation of Oscillating and Interacting Matter Wave Dark Solitons". In: *Phys. Rev. Lett.* 101 (13 2008), p. 130401.

[125] X. Chai et al. "Magnetic Solitons in a Spin-1 Bose-Einstein Condensate". In: *Phys. Rev. Lett.* 125 (3 2020), p. 030402.

[126] A. Farolfi et al. "Observation of Magnetic Solitons in Two-Component Bose-Einstein Condensates". In: *Phys. Rev. Lett.* 125 (3 2020), p. 030401.

[127] L. M. Aycock et al. "Brownian motion of solitons in a Bose–Einstein condensate". In: *Proc. Natl. Acad. Sci. U.S.A.* 114.10 (2017), pp. 2503–2508.

[128] N. Meyer et al. "Observation of Two-Dimensional Localized Jones-Roberts Solitons in Bose-Einstein Condensates". In: *Phys. Rev. Lett.* 119 (15 2017), p. 150403.

[129] A. R. Fritsch et al. "Creating solitons with controllable and near-zero velocity in Bose-Einstein condensates". In: *Phys. Rev. A* 101 (5 2020), p. 053629.

[130] L. D. Carr et al. "Dark-soliton creation in Bose-Einstein condensates". In: *Phys. Rev. A* 63 (5 2001), p. 051601.

[131] TF Scott, RJ Ballagh, and K Burnett. "Formation of fundamental structures in Bose-Einstein condensates". In: *J. Phys. B* 31.8 (1998), p. L329.

[132] M. H. Anderson et al. "Observation of Bose-Einstein condensation in a dilute atomic vapor". In: *Science* 269.5221 (1995), pp. 198–201.

[133] K. B. Davis et al. "Bose-Einstein Condensation in a Gas of Sodium Atoms". In: *Phys. Rev. Lett.* 75 (22 1995), pp. 3969–3973.

[134] C. C. Bradley et al. "Evidence of Bose-Einstein Condensation in an Atomic Gas with Attractive Interactions". In: *Phys. Rev. Lett.* 75 (9 1995), pp. 1687–1690.

[135] C. C. Bradley et al. "Evidence of Bose-Einstein Condensation in an Atomic Gas with Attractive Interactions [Phys. Rev. Lett. 75, 1687 (1995)]". In: *Phys. Rev. Lett.* 79 (6 1997), pp. 1170–1170.

[136] A. Görlitz et al. "Realization of Bose-Einstein Condensates in Lower Dimensions". In: *Phys. Rev. Lett.* 87 (13 2001), p. 130402.

[137] G. Andrelczyk et al. "Optical generation of vortices in trapped Bose-Einstein condensates". In: *Phys. Rev. A* 64 (4 2001), p. 043601.

[138] A. Romero-Ros et al. "On-demand generation of dark soliton trains in Bose-Einstein condensates". In: *Phys. Rev. A* 103 (2 2021), p. 023329.

[139] E. J. Halperin and J. L. Bohn. "Quench-produced solitons in a box-trapped Bose-Einstein condensate". In: *Phys. Rev. Research* 2 (4 2020), p. 043256.

[140] H. Kiehn et al. "Spontaneous generation of dark-bright and dark-antidark solitons upon quenching a particle-imbalanced bosonic mixture". In: *Phys. Rev. A* 100 (2 2019), p. 023613.

[141] N. G. Parker et al. "Soliton-Sound Interactions in Quasi-One-Dimensional Bose-Einstein Condensates". In: *Phys. Rev. Lett.* 90 (22 2003), p. 220401.

[142] G. Theocharis et al. "Dark matter-wave solitons in the dimensionality crossover". In: *Phys. Rev. A* 76 (4 2007), p. 045601.

[143] A. E. Muryshev, H. B. van Linden van den Heuvell, and G. V. Shlyapnikov. "Stability of standing matter waves in a trap". In: *Phys. Rev. A* 60 (4 1999), R2665–R2668.

[144] L. D. Carr, M. A. Leung, and W. P. Reinhardt. "Dynamics of the Bose-Einstein condensate: quasi-one-dimension and beyond". In: *J. Phys. B* 33.19 (2000), p. 3983.

[145] D. L. Feder et al. "Dark-soliton states of Bose-Einstein condensates in anisotropic traps". In: *Phys. Rev. A* 62 (5 2000), p. 053606.

[146] M. A. Hoefer and B. Ilan. "Onset of transverse instabilities of confined dark solitons". In: *Phys. Rev. A* 94 (1 2016), p. 013609.

[147] P. O. Fedichev, A. E. Muryshev, and G. V. Shlyapnikov. "Dissipative dynamics of a kink state in a Bose-condensed gas". In: *Phys. Rev. A* 60 (4 1999), pp. 3220–3224.

[148] A. Muryshev et al. "Dynamics of Dark Solitons in Elongated Bose-Einstein Condensates". In: *Phys. Rev. Lett.* 89 (11 2002), p. 110401.

[149] I. Shomroni et al. "Evidence for an oscillating soliton/vortex ring by density engineering of a Bose–Einstein condensate". In: *Nat. Phys.* 5.3 (2009), pp. 193–197.

[150] P. G. Kevrekidis et al. "Dynamics of interacting dark soliton stripes". In: *Phys. Rev. A* 100 (3 2019), p. 033607.

[151] G. Theocharis et al. "Multiple atomic dark solitons in cigar-shaped Bose-Einstein condensates". In: *Phys. Rev. A* 81 (6 2010), p. 063604.

[152] D. Yan et al. "Multiple dark-bright solitons in atomic Bose-Einstein condensates". In: *Phys. Rev. A* 84 (5 2011), p. 053630.

[153] S. Middelkamp et al. "Dynamics of dark–bright solitons in cigar-shaped Bose–Einstein condensates". In: *Phys. Lett. A* 375.3 (2011), pp. 642–646.

[154] A. Romero-Ros et al. "Controlled generation of dark-bright soliton complexes in two-component and spinor Bose-Einstein condensates". In: *Phys. Rev. A* 100 (1 2019), p. 013626.

[155] C. F. Barenghi, L. Skrbek, and Sreenivasan. K. R. "Introduction to quantum turbulence". In: *Proc. Nat. Acad. Sci. (USA)* 111 (2014), (suppl. 1) 4647.

[156] M. R. Andrews et al. "Direct, nondestructive observation of a Bose condensate". In: *Science* 273.5271 (1996), pp. 84–87.

[157] A. Ramanathan et al. "Partial-transfer absorption imaging: A versatile technique for optimal imaging of ultracold gases". In: *Rev. Sci. Instrum.* 83.8 (2012), p. 083119.

[158] E. W. Streed et al. "Absorption imaging of a single atom". In: *Nature communications* 3.1 (2012), pp. 1–5.

[159] C. C. Bradley, C. A. Sackett, and R. G. Hulet. "Bose-Einstein Condensation of Lithium: Observation of Limited Condensate Number". In: *Phys. Rev. Lett.* 78 (6 1997), pp. 985–989.

[160] R. Meppelink et al. "Thermodynamics of Bose-Einstein-condensed clouds using phase-contrast imaging". In: *Phys. Rev. A* 81 (5 2010), p. 053632.

[161] J. J. Hope and J. D. Close. "Limit to Minimally Destructive Optical Detection of Atoms". In: *Phys. Rev. Lett.* 93 (18 2004), p. 180402.

[162] D. V. Freilich et al. "Real-time dynamics of single vortex lines and vortex dipoles in a Bose-Einstein condensate". In: *Science* 329.5996 (2010), pp. 1182–1185.

[163] S. Donadello et al. "Observation of solitonic vortices in Bose-Einstein condensates". In: *Physical review letters* 113.6 (2014), p. 065302.

[164] S. Serafini et al. "Dynamics and Interaction of Vortex Lines in an Elongated Bose-Einstein Condensate". In: *Phys. Rev. Lett.* 115 (17 2015), p. 170402.

[165] K. Hueck et al. "Calibrating high intensity absorption imaging of ultracold atoms". In: *Opt. express* 25.8 (2017), pp. 8670–8679.

[166] A. Putra et al. "Optimally focused cold atom systems obtained using density-density correlations". In: *Rev. Sci. Instrum.* 85.1 (2014), p. 013110.

[167] C. F Barenghi and N. G. Parker. *A primer on quantum fluids*. Springer, 2016.

[168] C. Menotti and S. Stringari. "Collective oscillations of a one-dimensional trapped Bose-Einstein gas". In: *Phys. Rev. A* 66 (4 2002), p. 043610.

[169] G. Baym and C. J. Pethick. "Ground-State Properties of Magnetically Trapped Bose-Condensed Rubidium Gas". In: *Phys. Rev. Lett.* 76 (1 1996), pp. 6–9.

[170]   E. A. L. Henn et al. "Bose-Einstein condensation in 87Rb: characterization of the Brazilian experiment". In: *Brazilian J. Phys.* 38.2 (2008), pp. 279–286.

[171]   M. Caracanhas et al. "Self-similar expansion of a turbulent Bose-Einstein condensate: A generalized hydrodynamic model". In: *J. Low Temp. Phys* 170 (2013), pp. 133–142.

[172]   P. H. Roberts and R. J. Donnelly. "Dynamics of vortex rings". In: *Phys. Lett. A.* 31.3 (1970), pp. 137–138.

[173]   C. F. Barenghi and R. J. Donnelly. "Vortex rings in classical and quantum systems". In: *Fluid Dyn. Res.* 41.5 (2009), p. 051401.

[174]   J. A. Seman et al. "Route to turbulence in a trapped Bose-Einstein condensate". In: *Laser Phys. Lett.* 8 (2011), pp. 691–696.

[175]   R. F. Shiozaki et al. "Transition to quantum turbulence in finite-size superfluids". In: *Laser Phys. Lett.* 8.5 (2011), pp. 393–397.

[176]   R. Desbuquois et al. "Superfluid behaviour of a two-dimensional Bose gas". In: *Nat. Phys.* 8 (2012), p. 645.

[177]   W. J. Kwon et al. "Sound emission and annihilations in a programmable quantum vortex collider". In: *Nature* 600.7887 (2021), pp. 64–69.

[178]   M. E. Mossman et al. "Dissipative shock waves generated by a quantum-mechanical piston". In: *Nat. Comm.* 9 (2018), p. 4665.

[179]   A Bahrami et al. "Investigation of the momentum distribution of an excited BEC by free expansion: Coupling with collective modes". In: *J. Low Temp. Phys.* 180.1 (2015), pp. 126–132.

[180]   C. Rorai et al. "Approach and separation of quantised vortices with balanced cores". In: *J. Fluid Mech.* 808 (2016), pp. 641–667.

[181]   P. Rosenbusch, V. Bretin, and J. Dalibard. "Dynamics of a Single Vortex Line in a Bose-Einstein Condensate". In: *Phys. Rev. Lett.* 89 (20 2002), p. 200403.

[182]   M. Modugno, L. Pricoupenko, and Y. Castin. "Bose-Einstein condensates with a bent vortex in rotating traps". In: *Eur. Phys. J. D* 22.2 (2003), pp. 235–257.

[183]   S. Komineas, N. R. Cooper, and N. Papanicolaou. "Single vortex states in a confined Bose-Einstein condensate". In: *Phys. Rev. A* 72 (5 2005), p. 053624.

[184]   C. F. Barenghi, V. L'vov, and P.-E. Roche. "Experimental, numerical and analytical velocity spectra in turbulent quantum fluid". In: *Proc. Nat. Acad. Sci. USA* 111 (suppl. 1) (2014), pp. 4683–4690.

[185]   C. F. Barenghi, Y. A. Sergeev, and A. W. Baggaley. "Regimes of turbulence without an energy cascade". In: *Sci. Reports* 6 (2016), p. 35701.

[186]   B. Rousset et al. "Superfluid high Reynolds von Karman experiment". In: *Rev. Sci. Instruments* 85 (2014), p. 103908.

[187]   C. Nore, M. Abid, and M. E. Brachet. "Decaying Kolmogorov turbulence in a model of superflow". In: *Phys. Fluids* 9.9 (1997), pp. 2644–2669.

[188]   A. Leonard. "Computing three-dimensional incompressible flows with vortex elements". In: *Annu. Rev. Fluid Mech.* 17.1 (1985), pp. 523–559.

[189] O. Yurkina and S. K. Nemirovskii. "On the energy spectrum of the 3D velocity field, generated by an ensemble of vortex loops". In: *J. Low Temp. Phys.* 47.8 (2021), pp. 652–655.

[190] M. R. Smith et al. "Decay of vorticity in homogeneous turbulence". In: *Phys. Rev. Lett.* 71 (16 1993), pp. 2583–2586.

[191] A. Griffin, T. Nikuni, and E. Zaremba. *Bose-condensed gases at finite temperatures*. Cambridge University Press, 2009.

[192] C. F. Barenghi, V. S. L'vov, and P.-E. Roche. "Experimental, numerical, and analytical velocity spectra in turbulent quantum fluid". In: *Proc. Natl. Acad. Sci. U.S.A.* 111.supplement_1 (2014), pp. 4683–4690.